

# DISSERTATION

submitted to the

Combined Faculty of Natural Sciences and Mathematics  
of Heidelberg University, Germany

for the degree of

Doctor of Natural Sciences

Put forward by

GRIGORII V. SMIRNOV-PINCHUKOV

born in: MOSCOW, RUSSIA

Oral examination: January 12<sup>th</sup>, 2023



# **Formylium as a tracer of circumstellar disks physics**

Referees: Prof. Dr. Dr. h.c. Thomas K. Henning  
Prof. Dr. Cornelis Dullemond

## Abstract

There are many different tracers of circumstellar disk physics, most notably, micrometer to millimeter-sized dust, and one of the most abundant molecules, CO. Formylium ( $\text{HCO}^+$ ) is another commonly observed species. Its chemistry is more complex than CO chemistry, and more interpretation steps are necessary to build the bridge between the disk structure and observed emission. Its isotopologs  $\text{DCO}^+$  and  $\text{H}^{13}\text{CO}^+$  complement the picture and allow a more precise understanding of the disk structure. In this thesis, I present my results achieved by combining and developing physical modeling, chemical kinetics, and radiative transfer methods to understand circumstellar disks' physical properties through formylium isotopologs observations. I explain the observed  $\text{DCO}^+$  increase in the protoplanetary disk gap and use it as proof of the reduced amount of gas in the gaps. I show that  $\text{HCO}^+$  should be the brightest molecule after CO isotopologs in the gas-rich debris disks, and its brightness would reveal the elemental composition, but a next-generation observatory is needed to detect it. Then I present an application of the machine learning approach to predict the modeled disk chemistry instantaneously based on the pre-computed disk models' data set, allowing the replacement of computationally expensive thermo-chemical models in the fitting pipelines. Finally, I demonstrate the data which will be analyzed using this approach.

## Zusammenfassung

Es gibt viele verschiedene Indikatoren für die Physik zirkumstellarer Scheiben, vor allem Mikrometer- bis Millimetergroßen Staub und eines der häufigsten Moleküle, CO. Formylium ( $\text{HCO}^+$ ) ist eine weitere häufig beobachtete Spezies. Seine Chemie ist komplexer als die von CO, und es sind mehr Interpretationsschritte erforderlich, um die Brücke zwischen der Scheibenstruktur und der beobachteten Emission zu schlagen. Seine Isotopologe  $\text{DCO}^+$  und  $\text{H}^{13}\text{CO}^+$  ergänzen das Bild und ermöglichen ein genaueres Verständnis der Scheibenstruktur. In dieser Arbeit stelle ich meine Ergebnisse vor, die ich durch die Kombination und Weiterentwicklung von physikalischer Modellierung, chemischer Kinetik und Strahlungstransfermethoden erzielt habe, um die physikalischen Eigenschaften zirkumstellarer Scheiben anhand der Beobachtungen von Formylium-Isotopologen zu verstehen. Ich erkläre den beobachteten  $\text{DCO}^+$ -Anstieg in der protoplanetaren Scheibenlücke und verwende ihn als Beweis für die geringere Gasmenge in den Lücken. Ich zeige, dass  $\text{HCO}^+$  nach den CO-Isotopologen das hellste Molekül in den gasreichen Trümmerscheiben sein sollte, und seine Helligkeit würde die elementare Zusammensetzung verraten, aber es wird ein Observatorium der nächsten Generation benötigt, um es zu entdecken. Dann stelle ich eine Anwendung des Ansatzes des maschinellen Lernens zur sofortigen Vorhersage der modellierten Scheibenchemie auf der Grundlage des vorberechneten Datensatzes der Scheibenmodelle vor, wodurch die rechenintensiven thermo-chemischen Modelle in den Anpassungspipelines ersetzt werden können. Schließlich demonstriere ich die Daten, die mit diesem Ansatz analysiert werden.

---

# Contents

<b>Abstract</b>	<b>2</b>
<b>1 Introduction</b>	<b>5</b>
1.1 Circumstellar disks	7
1.2 Physics of protoplanetary disks	14
1.3 Astrochemistry of circumstellar disks	16
1.4 Radiative transfer and line emission	20
<b>2 HCO<sup>+</sup> isotopologs and gas depletion</b>	<b>23</b>
2.1 Introduction	25
2.2 Methods and models	27
2.2.1 Thermo-chemical modeling	27
2.2.2 ANDES post-processing	28
2.2.3 Chemical model	31
2.2.4 Line radiative transfer	32
2.3 Results	37
2.3.1 Reference model (R)	38
2.3.2 Gas-poor model (A)	39
2.3.3 Gas-rich, dust-poor model (B)	39
2.4 Discussion	40
2.4.1 Model uncertainties and future development	40
2.4.2 Comparison with previous studies	40
2.5 Conclusions	44
<b>3 Molecules in CO-rich debris disks</b>	<b>45</b>
3.1 Introduction	47
3.2 Targets and selected molecules	50
3.3 Observations and data reduction	53
3.4 Results and analysis	57
3.5 Discussion	60
3.5.1 Photodissociation of molecules	60
3.5.2 Chemical and line flux modelling	64
3.5.3 Effect of hydrogen depletion on disk scale height	67
3.6 Conclusions	70
3.7 App. A: Results of the continuum observations	72
<b>4 ML-accelerated chemistry</b>	<b>75</b>
4.1 Introduction	77
4.2 Thermo-chemical protoplanetary disk model grid	79
4.3 KNN estimator training	81
4.4 Results and discussion	83
4.5 Conclusions	84

4.6	App. B: Additional figures . . . . .	85
<b>5</b>	<b>PRODIGE sample</b>	<b>91</b>
5.1	Ionization of protoplanetary disks and formylium isotopologs . . . . .	92
5.2	Observations . . . . .	93
5.3	Protoplanetary disk model . . . . .	97
5.4	Bayesian fitting . . . . .	99
<b>6</b>	<b>Summary</b>	<b>105</b>
	<b>Authored publications</b>	<b>107</b>
	<b>Bibliography</b>	<b>108</b>
	<b>Acknowledgements</b>	<b>115</b>
	<b>Declaration of Originality</b>	<b>117</b>

# **Chapter 1**

## **Introduction**

## Thesis outline

In Section 1.1, I briefly summarize the history and current view of the planet formation process with an overview of observational methods to characterize the disks. In Section 1.2, I describe various approaches to disk physics modeling, focusing on the method most commonly used together with astrochemistry. An overview of the circumstellar disk chemistry and possible reaction types follows in Section 1.3. The introduction is summarized with Section 1.4 describing the physics of emission line formation.

The Chapters 2-5 of the thesis are a compilation of the most important pieces of research I performed in the last years. Chapter 2 describes the thermo-chemical modeling of protoplanetary disks in relation to the most common substructure, a gap. Chapter 3 describes and discusses the non-detection of most of the molecular species in a later stage of a circumstellar disk, a CO-rich debris disk. Chapter 4 proposes a novel method to accelerate protoplanetary disk chemistry modeling drastically. It is followed by Chapter 5 showing yet unpublished disk chemistry retrieval method.

The outcome of the thesis is summarized in Chapter 6, with a complete bibliography list, acknowledgments, and the declaration of originality.

*The PDF version of this thesis contains active links to figures, tables, text sections, and bibliography items.*

---

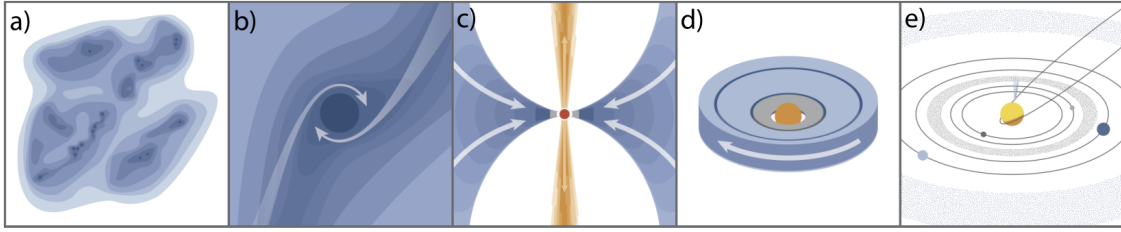


Figure 1.1: A sketch of different stages of low-mass star and planet formation, adopted from Öberg & Bergin (2021), credit: K. Peek. *a*: Dense cores form in a molecular cloud. *b*: The dense core collapses due to self-gravity. *c*: The center of the core becomes hot and dense, starting the nuclear fusion reactions with a low barrier. Accretion continues, but the accreting material flattens to a disk, and some are ejected via the jet. *d*: A protostar is surrounded by a semi-stable rotating protoplanetary disk, a birthplace for planets, for 2-5 million years. *e*: As most of the gas leaves the system either via evaporation or accretion, the leftover dust, pebbles, and planetesimals support the planet growth and migration for another 100 million years.

## 1.1 Circumstellar disks

Circumstellar disks are one of the most thrilling objects observed by astronomers in the last decade. Indeed, these are the cradle for planets, and the Earth was once a cloud of pebbles in the disk around the young Sun. Being drastically complex in their physical and chemical structure, circumstellar disks attract hundreds of researchers to plan and execute observations and to develop and run models. The exact path of planet formation is debated, but with recent observations, it is starting to become more and more clear. Modern observatories provide an unprecedented view of the young planetary systems, and they cover wavelengths from millimeter radio to X-ray. Thermal continuum emission of millimeter-to-micrometer-sized dust; line emission from dozens of molecules, atoms, and ions; scattered light of the host star; and the stellar radiation itself are different and independent channels to study the circumstellar disks. Being able to combine these data together is crucial. In this thesis, I am touching on a minor piece of this picture: application of the computational chemistry methods to the data coming from the world's best observatories, focusing specifically on formylum ( $\text{HCO}^+$ ) isotopologs.

Being a relatively short period in the evolution of a low-to-middle mass star ( $\lesssim 3M_{\odot}$ ), the first ten million years shape the planetary system for billions of years. A new population of stars forms in a giant molecular cloud, with each star forming from its own clump. The excess envelope gas is mainly blown away by the energy produced by the nuclear reactions in the stellar cores. Due to viscosity and the initial angular momentum, the leftover gas tends to form a disk-like structure around the central star. The outer disk is efficiently shielded by the dense inner disk, preventing quick dissipation. Before the star injects enough energy into the disk, the solid carbon, silicate, ice, and metal particles stick together and form larger and larger dust particles, pebbles, planetesimals, and, eventually, planets.

The stars hosting planet-forming disks were first identified by a broad infrared to sub-mm continuum emission excess from the disk in their spectral energy distribution (SED),  $\nu S_{\nu}(\nu)$ . The first statistical infrared observations were made by the Infrared Astronomical Satellite (IRAS) (Strom et al. 1989, see Fig. 1.2 left). The sub-millimeter observations followed the infrared observations, and mm-sized hot dust was first detected (Weintraub et al. 1989). The Hubble Space Telescope soon confirmed the disk-like shape (O'Dell & Wen 1994, Fig. 1.2 right).

The later advancements in the development of the infrared space observatories (Infrared Space Observatory (ISO), Spitzer Space Telescope, and Herschel Space Observatory), millimeter single-dish telescopes (Institut de Radioastronomie Millimetrique 30-meter telescope, Robert C. Byrd Green Bank Telescope), millimeter interferometers (Submillimeter Array (SMA), Plateau de Bure Interferometer and its upgrade Northern Extended Millimeter Array (NOEMA, Fig. 1.3), and, recently, The Atacama Large Millimeter/submillimeter Array (ALMA)), and sensitive X-ray telescopes (Chandra X-ray Observatory, X-ray Multi-Mirror Mission (XMM-Newton), Neil Gehrels Swift Observatory) have provided a multi-wavelength view on the disk physics.

The traditional classification of the protostars is based on SED shape (for an overview of disk-related terms, see Evans et al. 2009). Class 0 protostars require the heat source to appear in the center of the dense core, which corresponds to a late stage of  $b$  in Fig. 1.1. Observationally they are found by sub-millimeter (0.35 mm) luminosity being at least 0.5% of the bolometric luminosity, and the bolometric temperature not exceeding 70 K, typically 15 – 30 K. As the evolution of the system progresses to the stage Class I, or  $c$  in Fig. 1.1, the central heat source becomes hotter. However, the envelope still dominates the total emission in the far infrared (FIR). This stage is characterized by the spectral index  $\alpha$ , the slope of the SED between NIR and MIR (2 and 20  $\mu\text{m}$ ), as  $\alpha \gtrsim 0.3$ . The dissipation of the envelope leaves the star surrounded only by a protoplanetary disk with primordial chemical composition, a Class II object, shown as stage  $d$  in Fig. 1.1. At this stage, the disk contributes significantly to the far infrared excess with  $-1.6 < \alpha < 0.3$ , and this is the most important period for the planet formation and molecular enrichment of the disk material, forming planets up to Jupyter scale and complex organic molecules. After a few million years, most of the gas leaves the system either via accretion onto the host star or via winds, and dust grows into centimeter pebbles, rocks, and planetesimals, which collide and shatter again. The trapped molecular ice from the grain surfaces partially returns back to the disk as secondary, hydrogen-poor gas. Only a leftover debris disk, which is the last stage of planet formation, or Class III, is left. Finally, the dust does not contribute to the SED much, corresponding to  $\alpha < -1.6$ . The debris disk may stay in a system for billions of years: once it loses most of the viscous gas, nothing leads to a significant angular momentum transfer. Kuiper asteroid belt between Mars and Jupiter, Oort cloud in the outer Solar system, and the 10-micron scale dust in the inner Solar system scattering the solar light into zodiacal light are manifestations of the gas-poor debris disks orbiting Sun.

Over time, the development and deployment of new observatories led to increased detailization in our understanding of the disk variety, physics, and evolution. The golden age of the circumstellar disks has begun in the last decade, with the results from ALMA. Several large programs on ALMA and NOEMA were dedicated primarily to revealing structure, physics, and chemistry in protoplanetary disks. The results of two projects were recently published. ALMA large program Disk Substructures at High Angular Resolution Project (DSHARP), providing spatially resolved observations of dust, has shaped our understanding of protoplanetary disk dust substructures (Andrews et al. 2018, Fig. 1.4). The Molecules with ALMA at Planet-forming Scales large program has studied five protoplanetary disks to provide a large number of molecular probes at high angular resolutions (Öberg et al. 2021, Fig. 1.5). More large programs are coming from ALMA and NOEMA. A short comparison of all the disk-related large programs is given in Table 1.1. This thesis presents the novel approach for quick disk modeling for the model retrieval in Chapter 4, which will be used in the NOEMA large program PROtoplanetary DIskS: Global Evolution (PRODIGE, PI: Thomas Henning).

Observations of the disks continue in other parts of the electromagnetic spectrum. A very bright X-ray flare was detected during a predicted accretion event on a circumbinary

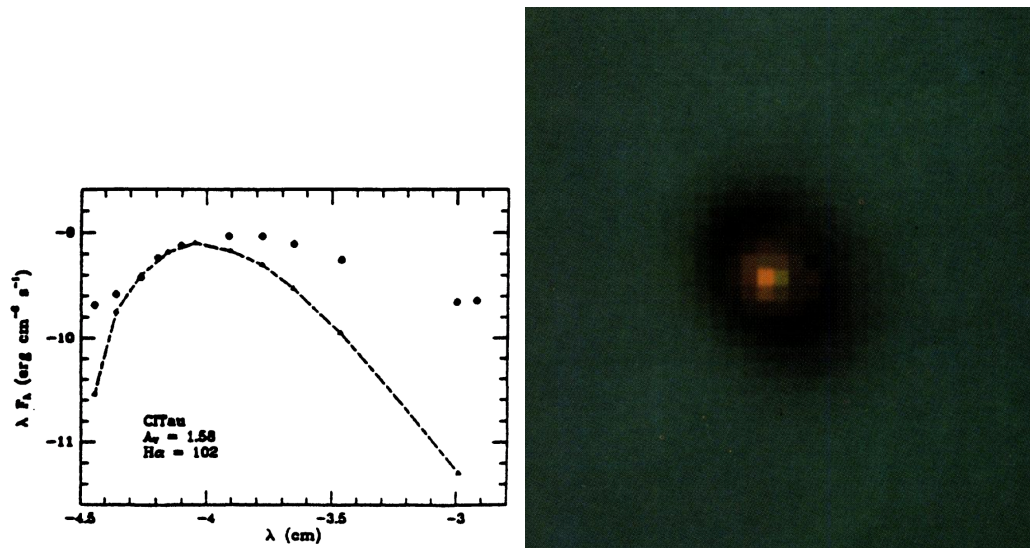


Figure 1.2: *Left*: First optical-to-infrared SED of CI Tau seen by IRAS space observatory with infrared (thermal emission of the colder dust) and blue (hot dust in the accretion region) excess compared to the stellar black-body (Strom et al. 1989). *Right*: First HST image of a protoplanetary disk shading the background Orion nebula (O'Dell & Wen 1994).



Figure 1.3: A concept art of the 12-antennae NOEMA expansion to the Plateau de Bure Interferometer observatory, downloaded from <https://www.iram-institute.org/>.

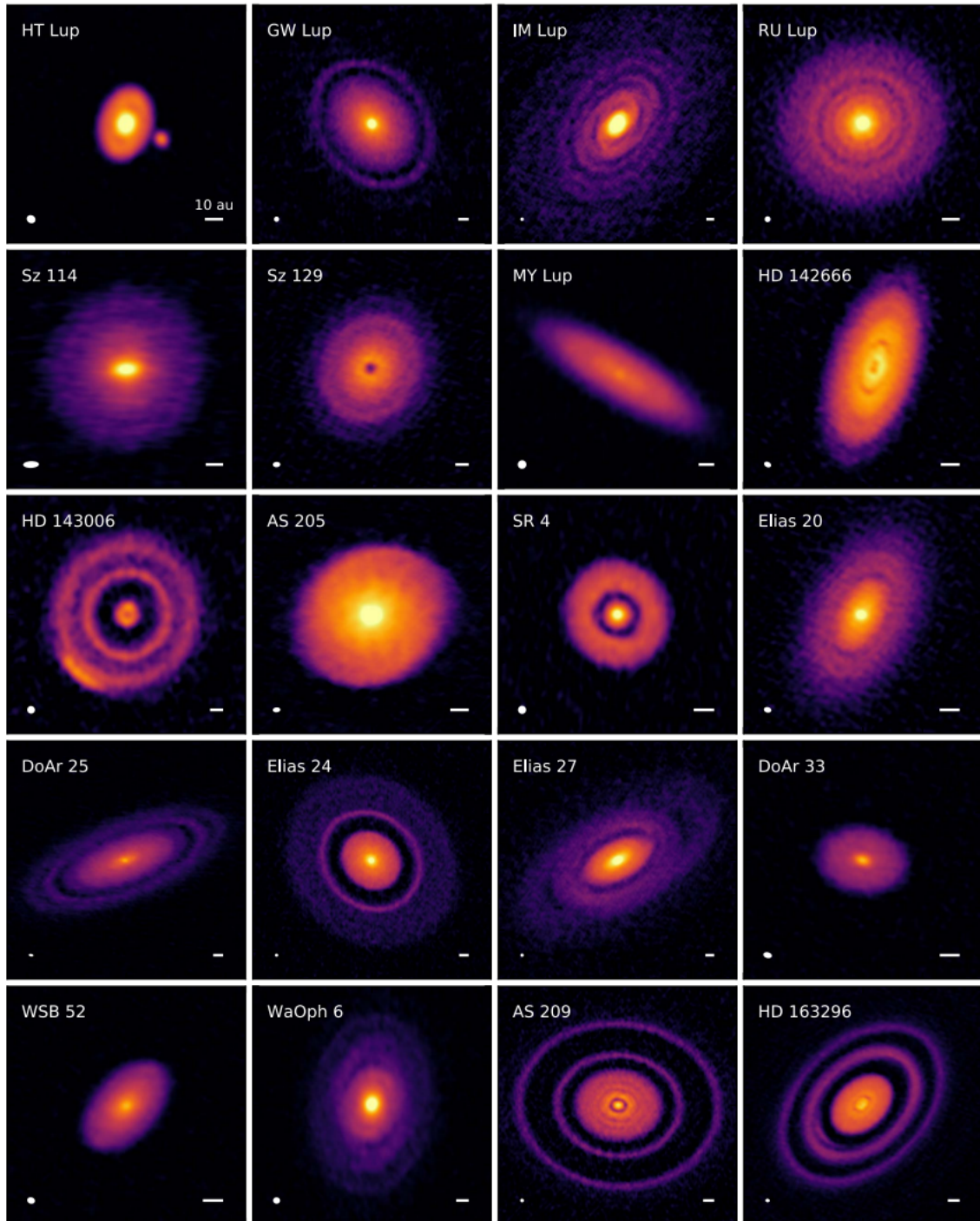


Figure 1.4: 240 GHz continuum maps from ALMA large program DSHARP (Andrews et al. 2018). The program has revealed a diversity of small-scale dust substructures in protoplanetary disks: rings and gaps (i.e., GW Lup, RU Lup, Elias 24, AS 209), spirals (i.e., Elias 27, the central region of IM Lup), banana-shaped asymmetries (i.e., HD 143006, HD 163296). HD 163296 maps in 20 molecular transitions are shown in Fig. 1.5.

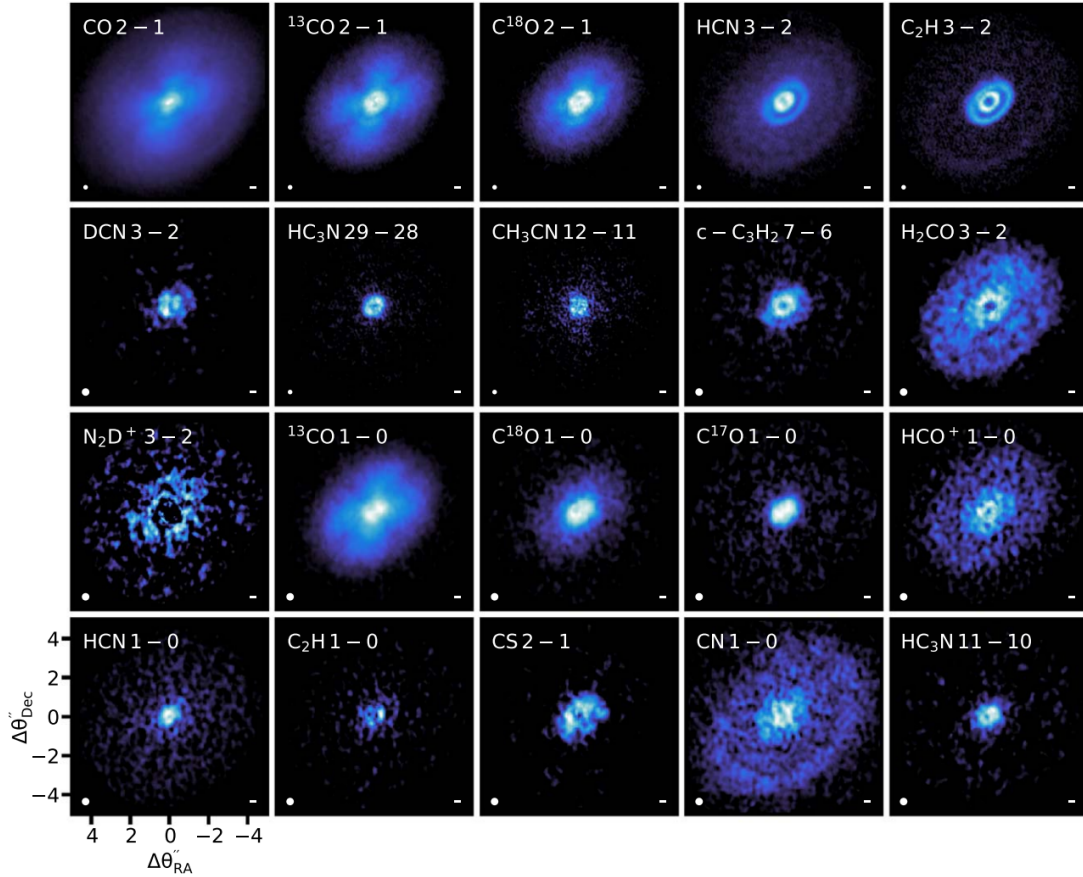


Figure 1.5: Protoplanetary disk HD 163296 in 20 molecular transitions seen by ALMA large program MAPS (Öberg et al. 2021). A bar in the lower right of each panel corresponds to 20 au. The inner disk part is visible in mm-sized dust continuum emission (Fig 1.4, lower right), and the gaseous disk is significantly larger. Various transitions of multiple molecules highlight disk regions with specific physical conditions.

Program name	PI	Project ID	Sources	Lines (sensitivity)	Resolution	Publication (notable)
Disk Substructures at High Angular Resolution Project (DSHARP)	Sean Andrews	ALMA 2016.1.00484.L	20 massive disks IM Lup, AS 209, HD 163296, etc.	CO (2 – 5 K), 1.3 mm contin- uum (0.1 – 0.7 K)	5 au	Andrews et al. (2018) (substructures in dust)
The Molecules with ALMA at Planet-forming Scales (MAPS)	Karin Öberg	ALMA 2018.1.01055.L	IM Lup, GM Aur, AS 209, HD 163296, MWC 480	4 setups at 3 mm (1 K) and 1.3 mm (0.3 K)	10 au	Öberg et al. (2021) (substructures in gas, many molecules)
PROtoplanetary Global Evolution (PRODIGE)	Thomas Henning	NOEMA L19ME	CI, CY, DG, DL, DM, DN, IQ Tau, UZ Tau E	4 broad setups at 1.1 – 1.4 mm (0.1 K)	150 au	in prep. (high sensitivity, more molecules)
The ALMA survey of Gas Evolution in PROtoplanetary disks (AGE-PRO)	Ke Zhang	ALMA 2021.1.00128.L	30 disks	CO isotopologs, N <sub>2</sub> H <sup>+</sup> , 1.1 and 1.4 mm	15 au	in prep. (mass and size estimations)
exoALMA	Richard Teague	ALMA 2021.1.01123.L	15 disks	CO, <sup>13</sup> CO and CS at 1.3 mm	15 au	in prep. (planets detection by kinematics)
The ALMA survey to Resolve exoKuiper belt Substructures (ARKS)	Sebastian Marino	ALMA 2022.1.00338.L	18 exoKuiper belts	Not announced	N/A	no data taken (exoplanets in Class III)
The ALMA Disk-Exoplanet C/Onnection	Ilse Cleeves	ALMA 2022.1.00875.L	80 disks	C <sub>2</sub> H, N <sub>2</sub> H <sup>+</sup> , CO	N/A	no data taken (elemental composition)

Table 1.1: Overview of large circumstellar disk observation programs. ALMA large programs are listed at <https://almascience.eso.org/alma-data/lp>.

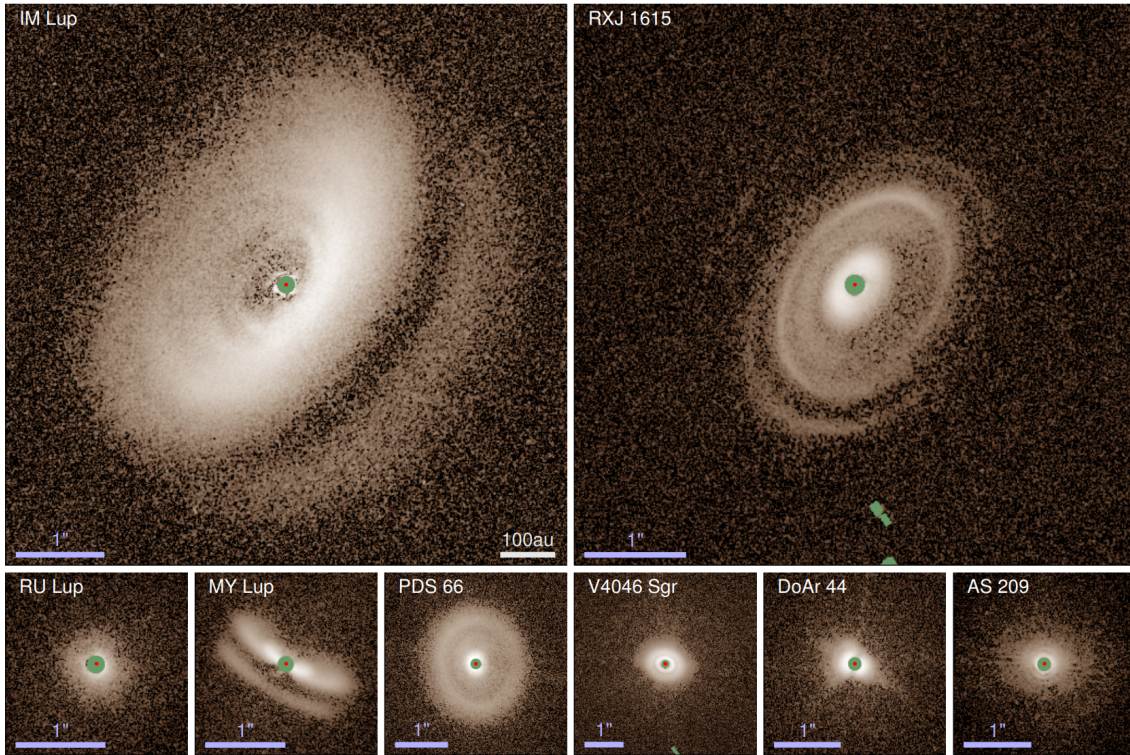


Figure 1.6: Near-infrared H-band images of the circumstellar disks around T Tauri stars obtained with SPHERE/IRDIS, adopted from Avenhaus et al. (2018). All disks are shown at the same physical scale.

disk DQ Tau using the Neil Gehrels Swift Observatory within a program of coordinated observations using the IRAM 30-m millimeter telescope, ALMA, Swift, the Fiber-fed Extended Range Optical Spectrograph (FEROS) on the 2.2-m telescope at the La Silla observatory, and support from small optical telescopes (PIs: van Terwisga, Smirnov-Pinchukov, preliminary X-ray analysis published as Getman et al. 2022). The scattered light observations using Spectro-Polarimetric High-contrast Exoplanet REsearch (SPHERE) instrument reveal the non-uniform structure of the small dust in the disk atmospheres (Fig. 1.6, Avenhaus et al. 2018). Comparisons between the ALMA and SPHERE observations of the disk substructures provide more information on the connection between different layers of the disk by studies of different dust populations (Brown-Sevilla et al. 2021). The James Webb Space Telescope (JWST), which became operational in 2022 will provide infrared spectra to characterize ice mantle properties and the hot gas in the inner disk.

The observations themselves do not provide us with the physical parameters of the circumstellar disks. The interpretation of the observations relies on a combination of models used to reproduce the data. Circumstellar disk chemistry is complex, and the structures seen in the molecular emission do not directly link with the physics, especially if the sensitivity and or resolution are not high enough to locate and trace individual features. The models of gas and dust distribution in the disk linked with chemical and radiative transfer models build the bridge between the physical parameters of the disk, such as total disk mass, and the observations. In the next sections of this introduction, I will focus on the basic concepts of these models.

## 1.2 Physics of protoplanetary disks

Physical modeling of the Class II protoplanetary disks is a challenge, involving a vast number of various physical effects and requiring an interdisciplinary approach. Protoplanetary disks are among the most complex objects astrophysicists attempt to model. Indeed, they appear as a rotating turbulent cloud of partially and not-uniformly ionized gas mixture, irradiated by UV, X-rays, and cosmic rays, mixed with solids from nanometer (PAHs and nanodiamonds) to tens of thousands kilometers (planets) scale. On top of all that, the gas reacts chemically, changing the local molar weight and adiabatic index as molecules are dissociated in the upper layers and obtaining new heating and cooling mechanisms via the new combination of possible energy transitions. All this complexity cannot simply be put in a single model. Hydrodynamical simulations operate only on a handful of equations but require a fine spatial and temporal grid. On the other limit, chemical networks operate tens of thousands of equations but at significantly longer timescales. A direct combination would lead to a practically unsolvable combination of a large number of equations on a fine grid.

The standard solution is to focus only on a subset of the physical effects. Hydrodynamical models can point at instabilities leading to disk substructures such as gaps or spirals. The inclusion of ionization and, thus, magnetohydrodynamics does one more step toward explaining the mechanisms of the angular momentum transfer. Growth and migration of solids models are used to explain the distribution of mm-sized dust seen by ALMA and the formation of planets. High-energy radiation causing photodissociation and ionization is paramount for chemical modeling.

The typical chemical modeling of a protoplanetary disk starts with a “physical” model – a model of the mass distribution and temperature of the gas and the dust in the disk. The interstellar medium dust to gas mass ratio is about 0.01, as the most abundant elements, hydrogen and helium, do not form solids. The accreting gas defines the structure of the whole disk. Observations are consistent with the power-law radial density profile with additional exponential tapering at hundreds of astronomical units (au, roughly the radius of the Earth orbit). The vertical disk structure is usually assumed to be hydrostatic, which leads to a gaussian vertical density distribution if the disk is isothermic, and a more “puffed” structure if the disk is hotter in the atmosphere.

As small micron-sized dust dominates both infrared opacity and surface area for chemical reactions and is also well-mixed with the gas, simple chemical models focus on it. The dust is heated by the central star’s radiation, which is re-emitted at longer wavelengths and scattered inside the disk. The disk surface is directly heated by the star and is thus relatively warm,  $\lesssim 100$  K at 100 au, with temperature scaling as  $\sim R^{-0.5}$ , where  $R$  is the distance to the star. The disk midplane is significantly colder, with temperatures below 20 K at 100 au. The small dust and gas temperatures are consistent in most of the disk ( $z/r \lesssim 0.4$ ) due to thermal conductivity between the dust surface area and the gas. The gas viscosity also heats the inner disk, but this effect is minor for the astrochemically-relevant radial distances of tens au. Some additional heating of the midplane is provided by hard X-ray and cosmic ray ionizing radiation penetrating the disk and absorbed by the dust and gas. Many significant cooling and heating processes happen in the disk atmosphere, where gas and dust temperature are decoupled. The gas temperature in the disk atmosphere is very high ( $\gtrsim 1000$  K). Gas is photodissociated and ionized, and thus heated, by the ultraviolet and soft X-ray radiation and is cooled only via line emission, primarily those of atomic ions  $C^+$  and  $O^+$  (Röllig et al. 2007).

The temperature distribution for the disk model can thus be calculated with various levels of proximity. As the general behavior of radial and vertical temperature profiles is

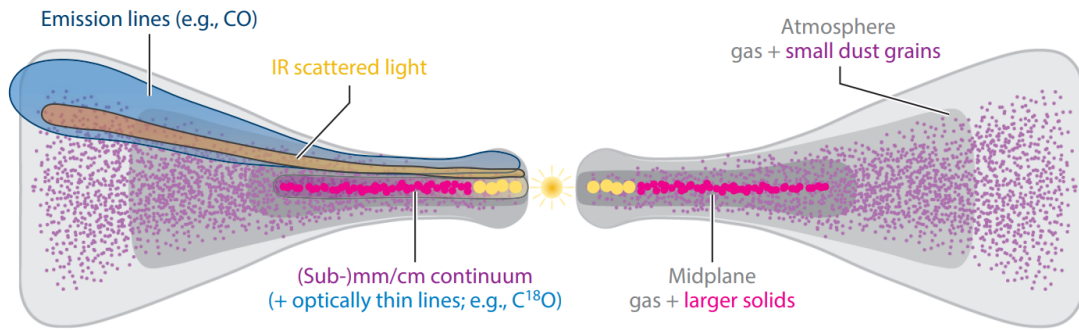


Figure 1.7: Protoplanetary Class II disk structure in a cross-section, adopted from Andrews (2020).

well studied, it can be just a parametrization based on the assumed disk density structure; for example, a standard approximation is given by Williams & Best (2014). Next, the dust radiative transfer model can be utilized to calculate the dust temperature distribution consistent with the central star emission and the dust density distribution. The inclusion of more heating and cooling processes is possible but computationally very expensive and requires iterative calculations of dust thermal structure, gas chemistry, and thermal balance to achieve convergence. Chapter 2 of this thesis demonstrates an application of such a thermo-chemical model for a protoplanetary disk with substructures.

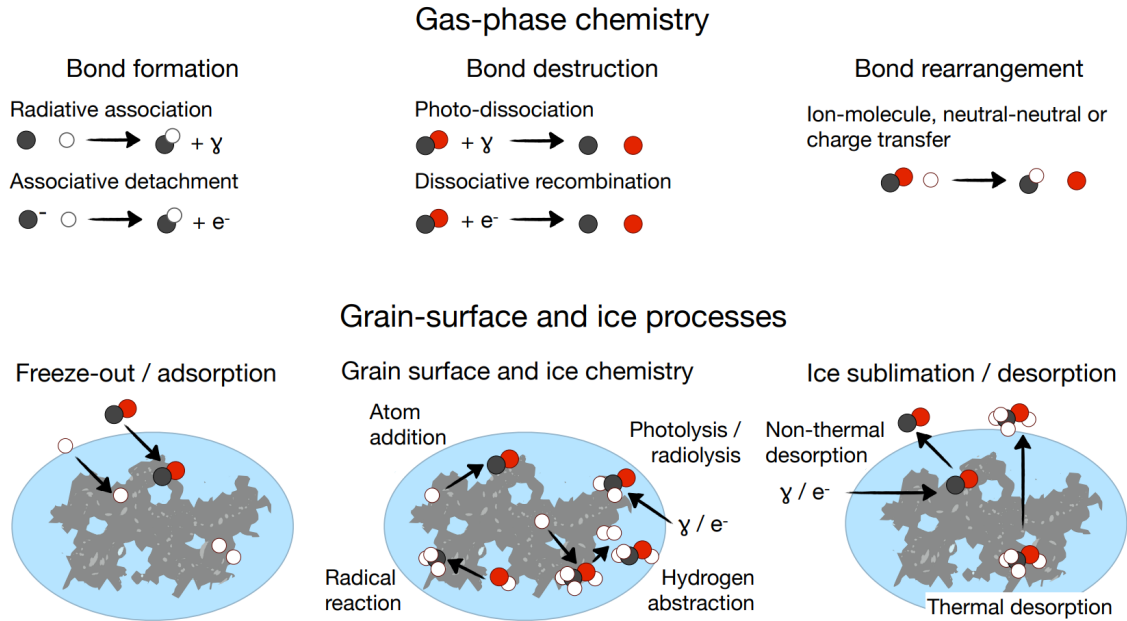


Figure 1.8: Common chemical reaction paths in protoplanetary disks, adopted from Öberg & Bergin (2021).

### 1.3 Astrochemistry of circumstellar disks

To compare a physical model and emission line data of the circumstellar disk, a crucial model step is required: to estimate the abundance of the emitting molecule and, thus, its density distribution across the disk. A detailed review on astrochemistry was published recently by Öberg & Bergin (2021). The chemistry of circumstellar disks dramatically differs from the chemistry easily observed on Earth. A high collision rate typical for “normal” chemistry in the dense medium provides a lot of possible formation paths to ensure that unstable molecules, such as radicals, quickly react to form a relatively limited set of stable molecules. In relatively short timescales, the gas mixture achieves chemical balance with minimal potential energy. The Earth atmosphere has  $2.7 \times 10^{19}$  particles per cubic centimeter at the ground level, which is enough to boost collision time scale to  $\tau_{\text{coll}} \sim 10^{-9}$  s. At this collision frequency, once two atoms collide and form a molecule ( $A + B \rightarrow AB$ ), a third particle has a chance to fly by and take away some of excess energy within the dissociation time scale of  $\tau_{\text{diss}} \sim 10^{-13}$  s (effectively,  $A + B + C \rightarrow ABC^* \rightarrow AB + C$ ).

As in particle physics, two-to-one merging (bond formation) reactions are forbidden in chemistry due to the impossibility of energy and momentum conservation without excess energy dissipation. The collision frequency is much lower for the low density and temperature of the circumstellar disk gas than in the Earth’s atmosphere (Herbst & Klemperer 1973). The only way to emit the excess energy would be in a form of photon (radiative association  $A + B \rightarrow AB + \gamma$  reaction), but the time scale of the relevant vibrational transition of the excited molecule of  $\tau_{\text{rad}} \sim 10^{-3}$  s is 10 orders of magnitude longer than  $\tau_{\text{diss}}$ , effectively forbidding such reactions. This difference is lower for some reactions if the resulting molecule is more stable in the excited state or can emit a photon faster. However, these reactions are not dominant in the molecule formation process.

Another particle that an excited molecule can emit is an electron. This is only possible for negatively-charged molecular ions (anions) as the ionization energy for neutral molecules is typically high, thus requiring one of reacting atoms to be an anion

already. This molecule formation path seems inefficient as positively charged ions (cations) are much more abundant and recombine quickly with anions, in addition to unstable anions being quickly destroyed by photoreactions (Millar et al. 2007).

Molecules in the interstellar medium and circumstellar disks, primarily hydrogen ( $\text{H}_2$ ), form on the surfaces of the dust grains (e.g. Garrod & Herbst 2006). Being macroscopic particles, the dust grains can internally dissipate the excess energy after a collision. Light hydrogen atoms efficiently tunnel between the potential energy minima and react with each other and other atoms, forming larger molecules and radicals. The dust grains serve as a “third body” of this reaction, and the resulting molecule can stay on a surface or desorb (evaporate) from the grain into the gas phase. The molecules trapped on the grain surface form an ice layer, which sublimates into the gas phase due to external radiation and internal heat of the grain.

Once molecules are returned to the gas phase, more types of reactions become available. More species can form in the gas phase in atom exchange ( $AB + C \rightarrow A + BC$ ), which is especially efficient for ions as they electrostatically attract other, even neutral, particles. More complex molecules form via neutral-neutral and ion-neutral bond rearrangement reactions ( $AB + CD \rightarrow ABC + D$ ).

The molecules are also destroyed, and their dissociation rate depends on local ionization and hard radiation from UV, X-Ray, and secondary photons from cosmic rays interacting with other particles. Reactions of dissociative recombination of a cation, such as  $\text{HCO}^+$ , with an electron typically have a large cross-section due to electrostatic attraction. High-energy photons react with molecules, too, with cross-sections depending on the photon wavelength. Higher-energy X-ray radiation has enough energy per photon to dissociate a molecule. For some molecules, photodissociation is effective in specific bands (see an extensive study by Heays et al. 2017, and adopted Fig.1.9). For abundant molecules, such as hydrogen and CO, even a small amount of molecules is enough to fully absorb all the incoming UV photons and shield the outer parts of the disk from the UV (so-called self-shielding). Moreover, hydrogen and CO mutually shield each other from radiation as their photodissociative bands partially overlap. Self-shielding is less efficient for other species, as their abundance is much lower. Due to self-shielding, hydrogen and CO remain the last gaseous molecular species to be observed in later stages of protoplanetary disk evolution, the debris disks (see Chapter 3 for more discussion and observational evidence).

These reactions are studied with different methods on different microscopic to macroscopic levels to be utilized in disk chemistry modeling (a recent review Garrod & Widicus Weaver 2013). The gas-phase reactions and photodissociation processes can be modeled using methods of quantum chemistry. To calculate the cross-section of gas-phase reactions, the potential energy between the reactants and the energy of the product is calculated depending on the distance between the molecules as a numerical solution to the corresponding Schrödinger equation, including atom nuclei and electrons. For the reaction to happen, the colliding particles should overcome the energy barrier, either having enough kinetic energy or tunneling through. The complication of this approach comes with the fact that the relative orientation and rotation of the particles also have an effect, providing uncertainty to the derived reaction rates. Photodissociation is modeled similarly, but the distance between products is calculated instead, and energy levels of the molecule are considered as possible intermediate steps, see Fig.1.9. Some of the reaction rates can be directly measured in the laboratory, but only quantum chemistry simulations are available for most of the reactions (Wakelam et al. 2012, 2015). For reactions, where simulations were compared with the laboratory measurements, the reaction rates differ by a factor of 3 (0.5 dex) (Smith 2011).

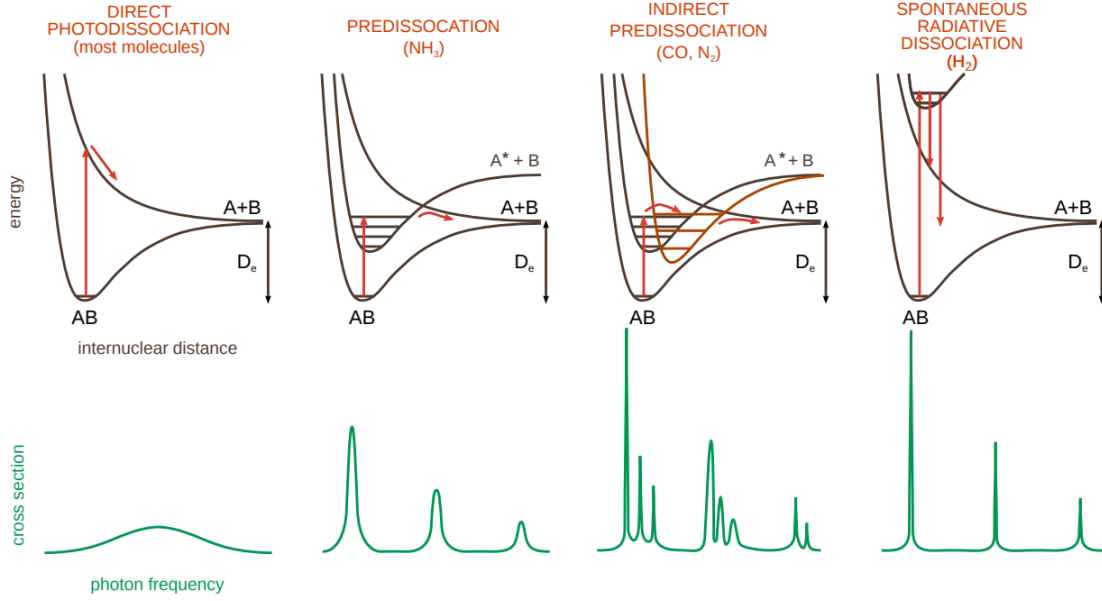


Figure 1.9: Photodissociation cross-section as a function of wavelength for different molecules, adopted from Heays et al. (2017).

The calculated cross-sections are directly utilized in chemical kinetics solvers such as ALCHEMIC (Semenov et al. 2010), NAUTILUS (Ruaud et al. 2016), UCLCHEM (Holdship et al. 2017) and KROME (Grassi et al. 2014), where they are converted into a system of equations in the form of:

$$A + \gamma \rightarrow C + D \iff -\dot{X}_{A,k} = \dot{X}_{C,k} = \dot{X}_{D,k} = X_A \int_0^{\text{inf}} \sigma_{\nu,k} I_\nu d\nu \approx X_A \sigma_k G$$

$$A + B \rightarrow C + D \iff -\dot{X}_{A,k} = -\dot{X}_{B,k} = \dot{X}_{C,k} = \dot{X}_{D,k} = X_A X_B f_k(T_{gas}),$$

In these equations,  $X_i$  is abundance of species  $i$ ,  $\dot{X}_{i,k}$  is time derivative of its abundance from reaction  $k$ . Wavelength-dependent photodissociation cross-section of the species in the reaction  $\sigma_{\nu,k}$  and local radiation intensity  $I_\nu$  are often averaged as a combination of so-called “radiation strength”  $G$  shared between different species and a reaction cross-section for a given reaction  $k$ . For independent radiation bands the reaction can be split in multiple sub-reactions, for example  $\sigma_k G \rightarrow \sigma_{k,NUV} G_{NUV} + \sigma_{k,FUV} G_{FUV} + \sigma_{k,X} G_X$  for near ultraviolet, far ultraviolet, and X-ray respectively.

For the two-reactants reactions,  $f_k(T_{gas})$  is usually a form of modified Arrhenius law:

$$f_k(T_{gas}) = \alpha_k \exp \left[ - \left( \frac{\gamma_k}{T} \right)^{\beta_k} \right],$$

Where  $\alpha_k$  is a function of the reaction cross-section,  $\gamma_k$  is the activation energy in Kelvin, and  $\beta_k \approx 1$  is an empirical factor to compensate for additional factors not accounted in this simple approach. These equations, added together for all reactions  $k$ , create an initial value problem for a linear ordinary differential equations system, which can be solved given the physical conditions.

The inclusion of dust-surface reactions makes this picture more complicated. The typical shape and surface composition are not well known for the dust in the circumstellar disk environment. The rates for the reactions on the dust surface cannot be derived as simply as the gas phase reactions. In addition to the reaction barriers calculated from the

quantum chemistry, the collision rate should be somehow estimated. Molecular dynamics simulations trace trajectories of a number of molecules and their reactions with each other, and parametrization of these simulations provides macroscopic reaction rates, which can be adopted by chemical kinetics code. The shape of the grains is debated, they are modeled either as spheres with layers of different ices on top, or expect more fractal porous shapes with all the different surfaces exposed for the chemistry (e.g. Garrod 2013). Regardless, only the surface layers of the dust grain are available for molecule formation, and there is a saturation limit at which higher on-grain abundance does not increase the number of reactions.

Chemical kinetics codes with large chemical networks (hundreds of species, thousands of reactions) are slow. Even the most optimized models with many simplifications take at least  $\sim 1$  second per physical bin to calculate chemistry from atomic or simple molecular composition for  $\sim 1$  Myr timescale. With disk models having thousands of separate bins, each model takes a while. In Chapter 4, I propose one more step in the chemistry simulation generalization. The physical conditions in the protoplanetary (Class II) disks are correlated. For example, cold and dense regions always refer to the disk mid-plane, where UV and even X-ray radiation cannot penetrate. Looking at the simulations provided by a disk thermo-chemical model ANDES (Akimkin et al. 2013; Molyarova et al. 2017, 2018) I have found out that one can reproduce ANDES-like chemistry for other disk models, training a machine learning estimator on these data. This approach, for the first time, allows Bayesian fitting of emission line observations with disk models, allowing to directly retrieve the physical parameters such as disk mass or ionization rate of the star, of course, within the accuracy of the model.

## 1.4 Radiative transfer and line emission

The electromagnetic radiation emitted by a medium along the ray obeys the following equation:

$$\frac{dI_\nu(x)}{dx} = j_\nu(x) - \alpha_\nu(x)I_\nu(x),$$

Where  $I_\nu$  is intensity,  $j_\nu$  is emissivity (amount of radiation emitted per path), and  $\alpha_\nu$  is extinction (fraction of radiation absorbed per path), and all depend on the coordinate along the path  $x$ . The equation simplifies if divided by  $\alpha_\nu(x)$ :

$$\frac{dI_\nu(x)}{\alpha_\nu(x)dx} = \frac{j_\nu(x)}{\alpha_\nu(x)} - I_\nu(x) \iff \frac{dI_\nu(x)}{d\tau} = S_\nu(x) - I_\nu(x),$$

Where  $\tau = \int \alpha_\nu(x)dx$  is optical depth, and  $S_\nu$  is a source function, comprising the radiative properties of the medium. As the ray passes through the medium, the intensity exponentially tends from the initial value  $I_{\nu,0}$  to  $S_\nu$ :

$$I_\nu(\tau) = I_{\nu,0}e^{-\tau} + S_\nu(1 - e^{-\tau}) \approx I_{\nu,0}e^{-\tau} + S_\nu\tau + O(\tau^2)$$

Assuming  $\tau \ll 1$ , the optically-thin limit, and no background radiation  $I_{\nu,0} = 0$ , intensity is proportional to the optical depth:  $I_\nu(\tau) \approx S_\nu\tau$ . On the optically-thick limit  $\tau \gg 1$ , intensity becomes equal to the source function independent on the background radiation  $I_\nu \rightarrow S_\nu$ .

In case of local thermodynamic equilibrium (LTE),  $S_\nu$  is a Planck function  $B_\nu$ :

$$B_\nu(T) = \frac{2h\nu^3/c^2}{\exp(h\nu/k_B T) - 1},$$

Where  $k_B$  is the Boltzmann constant,  $h$  is the Planck constant, and  $c$  is the speed of light. At a low-frequency limit,  $h\nu/k_B T \ll 1$ , the Planck function is approximated to the classical Rayleigh-Jeans law, with emission being proportional to temperature:

$$B_\nu(T) = 2\nu^2 k_B T / c^2 \sim T$$

Radioastronomers commonly use this proportionality to bridge the source properties and the emitted light. The intensity is often converted to “brightness temperature” units, measured in Kelvin. In the optically-thick limit, the brightness temperature of a spatially-resolved source equals its source function, and thus, if LTE is assumed, the source thermodynamic temperature. Within the LTE assumption, if the brightness is measured at 1 K when the cloud temperature is expected to be 20 K, this suggests the optical depth of  $\tau = 0.05$ , giving a proxy for the column density. Suppose LTE is not achieved, for example, in masers. In that case, when the background radiation or other effects set the non-Boltzmann distribution of the energy levels in the medium, the brightness temperature at some frequencies can be many orders of magnitude higher than the actual thermodynamic temperature.

Quantum systems with a small number of energy levels, such as atoms or simple molecules, only have noticeable opacity at a few specific frequencies corresponding to energy transitions. As one of the simplest examples, a hydrogen atom only has the levels at

$$E_n = -\frac{13.6}{n^2} \text{ eV} \approx -\{13.6, 3.4, 1.5, 0.85, 0.54, 0.38, \dots\} \text{ eV}.$$

$k_B T = 1 \text{ eV}$  corresponds to  $T \approx 11600 \text{ K}$ , so temperatures of tens of thousands K are required to have excited hydrogen atoms at energy level  $-3.4 \text{ eV}$ ,  $10.2 \text{ eV}$  above

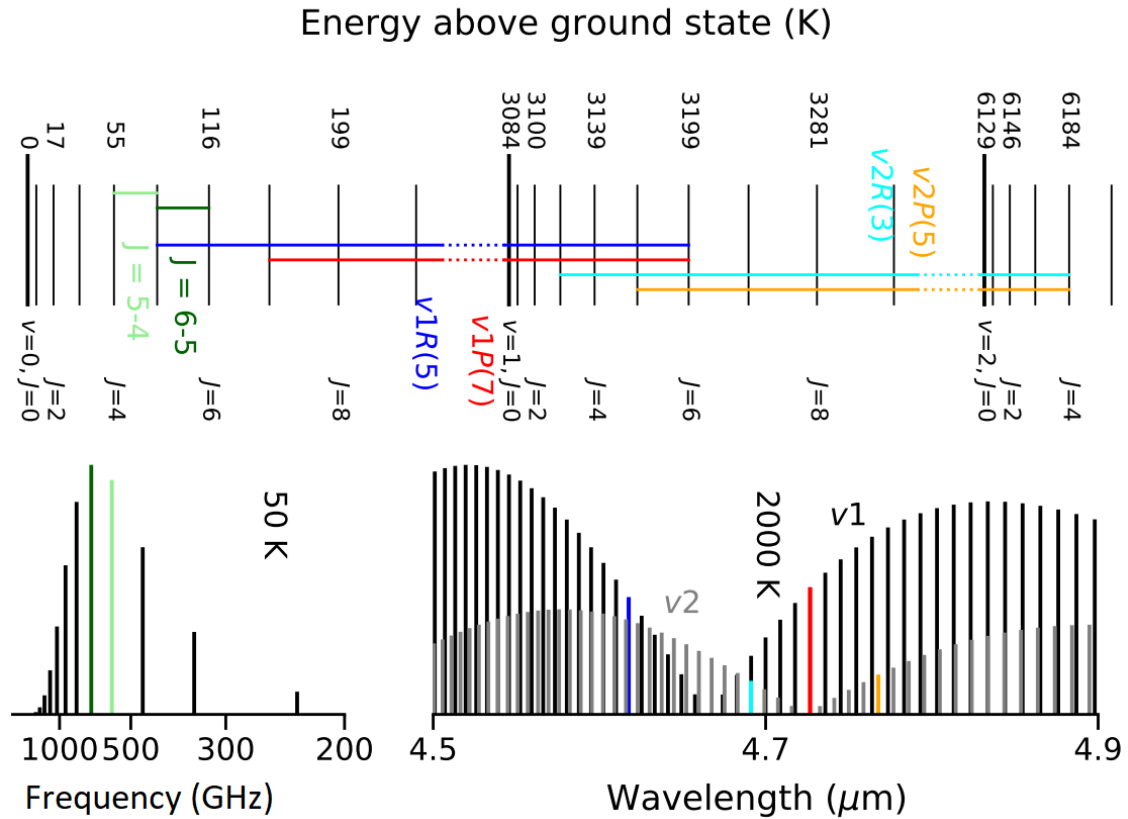


Figure 1.10: Some of CO energy levels and transitions, adopted from Bosman (2018).

the ground state. The transitions between the ground state and other energy levels, all belonging to the ultraviolet range of the electromagnetic spectrum, are called the Lyman series. Hydrogen atoms in the dense interstellar medium can only absorb light at these frequencies, and the ionizing far ultraviolet (FUV) with energies above 13.6 eV. The atomic hydrogen is transparent to all other long-wavelength electromagnetic radiation.

The larger amount of particles in a quantum system leads to increased number of energy levels and possible transitions between them. The most abundant molecule,  $\text{H}_2$ , does not have a dipole moment, and thus its rotational transitions are forbidden. Vibrational transitions of hydrogen have the upper state energy of more than 300 K and thus only happen in the hot gas. The two most common proxies for cold gas observations are HD and CO. There are two observable transitions in HD, at 112 and 56  $\mu\text{m}$ , in the far infrared, which are only observable from space telescopes. These transitions only get excited at temperatures of tens of K, higher than the temperatures of the disk midplanes. In addition, these lines are weak and required many hours to be detected on the Herschel Space Observatory (Trapman et al. 2017; Kama et al. 2020), decommissioned in 2013.

CO is a very convenient molecule for gas observations (Fig. 1.10). Its abundance to hydrogen is of  $X_{\text{CO}} \sim 10^{-4}$ . It is efficiently self-shielded from UV radiation and thus abundant even outside dense cores. CO is a volatile species; it freezes out on dust grains at about 20 K. Moreover, it is chemically active and forms more complex species, for example,  $\text{CO}_2$ , at temperatures below 30 K. Both effects lead to CO removal from the gas phase, thus underestimating the total gas mass if the fixed abundance is assumed.

Being optically thick in the low-level rotational lines CO  $J = 2 - 1$  (230 GHz) or  $J = 6 - 5$  (691 GHz) in the protoplanetary disk, CO is routinely observed by ALMA, NOEMA, and other ground-based mm-range interferometers and single-dish telescopes.

Bulk low-resolution observations of disk populations in star-forming clouds provide a lower limit for the disk gas masses. High-resolution spectrally-resolved CO observations constrain the disk structure and kinematics, indicating the effect of substructures and forming planets (Teague et al. 2021). Less abundant isotopologs  $^{13}\text{CO}$ ,  $\text{C}^{18}\text{O}$ ,  $\text{C}^{17}\text{O}$ , and  $^{13}\text{C}^{18}\text{O}$  allow deeper and deeper probes into the disk midplane (Wilson & Rood 1994, for the elemental ratios), and their combinations provide more accurate determination for the mass of CO. CO is not present in the disk midplane, but as density grows it can be supplemented with less abundant and less volatile CS.

$\text{HCO}^+$  (formylium) follows CO as one of the most abundant observable molecules in the protoplanetary disks.  $\text{HCO}^+$  is a product of highly efficient ion-molecule bond rearrangement, for example, between  $\text{H}_3^+$  and CO.  $\text{HCO}^+$  is a stable molecule sensitive only to harder UV radiation with a photodissociation lifetime in the interstellar radiation field of thousands of years. It is additionally shielded from UV by carbon atoms and hydrogen molecules. Formylium is not only a primary ionized species in the molecular layer but is also an intermediate step to forming organics, such as formaldehyde ( $\text{H}_2\text{CO}$ ). In this thesis, I focus on formylium and its isotopologs for all three chapters. In Chapter 2 I show that  $\text{HCO}^+$  and  $\text{DCO}^+$  together with  $\text{C}^{18}\text{O}$  provide a good tracer of gas depletion in the protoplanetary disk gaps. In Chapter 3, formylium is predicted to be the brightest yet still weak line in the gas-rich debris disk, and its non-detection confirms the assumption that the debris disks do not shield UV radiation. In Chapter 4 I present a way to reproduce the protoplanetary disk chemistry using machine learning quickly, and I demonstrate it on CO,  $\text{HCO}^+$ , and  $\text{DCO}^+$ .

## **Chapter 2**

# **Using HCO<sup>+</sup> isotopologs as tracers of gas depletion in protoplanetary disk gaps**

The widespread rings and gaps seen in the dust continuum in protoplanetary disks are sometimes accompanied by similar substructures seen in molecular line emission. One example is the outer gap at  $\sim 100$  au in AS 209, which shows that the  $\text{H}^{13}\text{CO}^+$  and  $\text{C}^{18}\text{O}$  emission intensities decrease along with the continuum in the gap, while the  $\text{DCO}^+$  emission increases inside the gap. We aim to study the behavior of  $\text{DCO}^+/\text{H}^{13}\text{CO}^+$  and  $\text{DCO}^+/\text{HCO}^+$  ratios in protoplanetary disk gaps assuming the two scenarios: (A) the gas depletion follows the dust depletion and (B) only the dust is depleted.

We first modeled the physical disk structure using the thermo-chemical model ANDES. This 1+1D steady-state disk model calculates the thermal balance of gas and dust and includes the far ultraviolet (FUV), X-rays, cosmic rays, and other ionization sources together with the reduced chemical network for molecular coolants. Afterward, this physical structure was adopted for calculations of molecular abundances with the extended gas-grain chemical network with deuterium fractionation. Ideal synthetic spectra and 0th-moment maps were produced with the Line Modeling Engine (LIME).

We are able to qualitatively reproduce the increase in the  $\text{DCO}^+$  intensity and the decrease in the  $\text{H}^{13}\text{CO}^+$  and  $\text{C}^{18}\text{O}$  intensities inside the disk gap, which is qualitatively similar to what is observed in the outer AS 209 gap. The corresponding disk model (A) assumes that both the gas and dust are depleted in the gap. The model (B) with the gas-rich gap, where only the dust is depleted, produces emission that is too bright in all  $\text{HCO}^+$  isotopologs and  $\text{C}^{18}\text{O}$ .

The  $\text{DCO}^+/\text{H}^{13}\text{CO}^+$  line ratio can be used to probe gas depletion in dust continuum gaps outside of the CO snow line. The  $\text{DCO}^+/\text{C}^{18}\text{O}$  line ratio shows a similar, albeit weaker, effect; however, these species can be observed simultaneously with a single (sub)mm interferometer setup.

*Published as Smirnov-Pinchukov et al. (2020) in A&A by Grigorii V. Smirnov-Pinchukov, Dmitry A. Semenov, Vitaly V. Akimkin, and Thomas Henning. DS and VA were the developers of the earlier versions of the used codes (ALCHEMIC and ANDES). All co-authors have contributed to the discussions of the methods and the results. I have tuned the codes to run them on the high-performance computing clusters, performed the simulation runs, and created the figures.*

*astrochemistry – methods: numerical – protoplanetary disks – stars: pre-main sequence – ISM: molecules – submillimeter: planetary systems*

---

## 2.1 Introduction

Protoplanetary disks are believed to be the birthplaces of planetary systems. While more and more theoretical studies of the planet formation in disks appear in the literature, they need observational constraints regarding physical conditions and chemical composition in various disks and disk locations. Now, in the Atacama Large (sub)Millimeter Array (ALMA), NOthern Extended Millimeter Array (NOEMA), Very Large Telescope / Spectro-Polarimetric High-contrast Exoplanet REsearch (VLT/SPHERE), and Gemini Planet Imager (GPI) era, the spatially resolved observations of dust and gas in protoplanetary disks in nearby star-forming regions have become a routine. High-resolution studies in dust continuum and scattered light with an angular resolution up to  $0.025'' - 0.04''$  reveal complex substructures with multiple gaps, inner holes, rings, and spirals (DSHARP: Andrews et al. 2018; Huang et al. 2018b; Long et al. 2019; Huang et al. 2020; van Boekel et al. 2017). The high-resolution observations in the CO isotopologs and other molecules also show the presence of substructures in the disk gas (see, e.g., Isella et al. 2016; Fedele et al. 2017; Teague et al. 2017; Huang et al. 2018a). Often disk substructures that are detected in the scattered light at near-infrared wavelengths do not coincide with the substructures visible in the submillimeter dust continuum and gas emission lines (Keppler et al. 2019).

One of the peculiar disks showing very wide gaps is AS 209. Huang et al. (2017) have studied continuum and line emission in this disk at the  $\sim 0.4''$  resolution with ALMA. They have found a notable difference between  $\text{H}^{13}\text{CO}^+$  and  $\text{DCO}^+$  emission radial profiles, with the  $\text{DCO}^+$  emission peak extending farther out up to radii of  $\lesssim 80 - 100$  au. The follow-up higher resolution observations have shown that the AS 209 disk has a dust gap at around 55–120 au (Fedele et al. 2018; Favre et al. 2019). At this gap location, the optically thin  $\text{C}^{18}\text{O}$   $J=2-1$  emission decreases slightly in intensity, while optically thick  $^{12}\text{CO}$   $J=2-1$  does not show any intensity decreases, and the  $\text{DCO}^+$   $J=3-2$  line reaches its peak intensity. Inspired by these puzzling observational findings, we decided to study whether a combination of optically thin and thick  $\text{HCO}^+$  isotopologs could be used as a probe for gas depletion in disk gaps that have been detected before in dust continuum or CO isotopologs.

There are several major factors that can cause molecular line emission in disks to show gap-like or ring-like substructures. Firstly, a circular gap or a ring in the line emission could be driven by a local, rather azimuthally symmetric deviation in the physical structure of the disk, either in density or temperature (e.g., due to planet-disk interactions, snowlines, a change in dust properties, etc. Lin & Papaloizou 1993; Guzmán et al. 2018; Huang et al. 2020). In the case of a surface density drop, the total molecular column density could become smaller or higher (e.g., for ions), which would lead to weaker or stronger line emission, as long as the line remains optically thin. Similarly, a local increase or decrease in the gas's kinetic temperature or background radiation affect molecular line excitation and hence emission intensity, assuming that the line is thermalized.

Secondly, molecular emission could show rings or gaps caused primarily by various chemical effects. The most prominent ones are ultraviolet (UV)-driven production or (selective) photodissociation in the disk atmosphere, C/O variations, and the freeze-out of molecules onto the dust grain surfaces in the disk midplane (see, e.g., Dutrey et al. 2017; Teague et al. 2017; Cazzoletti et al. 2018; Miotello et al. 2018, 2019; van Terwisga et al. 2019; Garufi et al. 2020). For example,  $c\text{-C}_3\text{H}_2$ , CCH, CN,  $\text{H}_2\text{CO}$ , and CS emission often shows a ring-like appearance in disks. Whereas for hydrocarbons and CN emission, the C/O variations and high-energy UV or X-ray irradiation are the most important factors;

for CS and  $\text{H}_2\text{CO}$  emission, the surface chemistry processes and freeze-out play the major role (Bergin et al. 2016; Cazzoletti et al. 2018; Miotello et al. 2019; van Terwisga et al. 2019). The ring-like appearance of  $\text{N}_2\text{D}^+$  and  $\text{DCO}^+$  emission in disks is mainly due to low-temperature deuterium fractionation when gaseous CO freezes out in the disk midplane (Qi et al. 2013; Ceccarelli et al. 2014; Huang & Öberg 2015; Salinas et al. 2018; Garufi et al. 2020). In addition, temporal variations in physical conditions can also affect chemical abundances, for example, via X-ray flares or episodic accretion outbursts (e.g., Cleeves et al. 2017; Molyarova et al. 2018; Lee et al. 2019).

Finally, a third relevant effect for molecular line excitation and emission intensity is the departure from local thermal equilibrium (LTE). It depends on the molecular properties and the location of the emitting molecular layer in the disk (Pavlyuchenkov et al. 2007). The most notable examples are the CN radical emitting from upper disk layer, where excitation is dominated by radiative processes, and  $\text{CH}_3\text{OH}$ , which have a complex energy level structure with torsional and coupled energy levels (e.g., Parfenov et al. 2016; Cazzoletti et al. 2018; Teague & Loomis 2020). Another effect that may affect the line excitation in disks locally is the localized deviation in the physical structure of the disk, which does not affect the global structure of the disk otherwise (e.g., local heating in a circumplanetary disk Cleeves et al. 2015a). This shows the complex interplay between the physical structure, chemistry, and excitation conditions in defining the strength of line emission and its spatial distribution in a disk.

The chapter is structured as follows. In the Section 2.2, we present the tools we use and the assumptions we make. In Section 2.3 we present the results for each model (2.3.1-2.3.3). In Section 2.4 we discuss the model uncertainties (2.4.1) and the comparison with previous observational gas gap studies (2.4.2). We provide the final conclusion in Section 2.5.

## 2.2 Methods and models

In this section we list all of the steps involved in our modeling. Firstly, we describe ANDES, the thermo-chemical code we used to simulate 1+1D disk gas and dust thermal structure (Subsection 2.2.1). Secondly, we explain how we combined the simulated vertical columns into three 2D disk models, with one reference model and two models with and without gas depletion in the dust gap. We recalculated the radial ionization and photodissociation self-shielding factors for those 2D physical structures (2.2.2). Thirdly, we briefly overview the chemical model ALCHEMIC with the deuterated network, which we used to calculate the chemical abundances (2.2.3). Finally, we describe how we computed the synthetic molecular line emission maps with LIME (2.2.4).

### 2.2.1 Thermo-chemical modeling

The standard practice of chemical modeling of protoplanetary disks includes some density structure setup, dust radiative transfer simulations for the thermal structure of the dust, gas thermal balance, and chemical kinetics calculations using the resulting structure (Dust And Lines (DALI) (Bruderer et al. 2009, 2014), PRotoplanetary Disk MOdel (ProDiMo) (Woitke et al. 2009), ANDES (Akimkin et al. 2013), also (Gorti & Hollenbach 2004; Cleeves et al. 2013; Du & Bergin 2014; Walsh et al. 2015; Salinas et al. 2018)). The ANDES model allows one to simulate the chemical evolution of a protoplanetary disk with a detailed treatment of gas and dust thermal balance. Its original version (Akimkin et al. 2013) is based on a 1+1D approach, where the vertical disk structure at each radius is simulated independently. In the upper, low-density regions of the protoplanetary disk, the gas temperature is not coupled to the dust temperature. The gas density becomes too low for thermal accommodation with the dust, and the gas usually becomes hotter than the dust as it cools itself rather inefficiently (Röllig et al. 2007). The gas density, temperature, and chemical composition depend on each other, so iterative modeling of the vertical disk structure is performed. After the initial chemical assumptions are made, the thermal balance for this predefined chemical structure is calculated. The chemical kinetics calculations are iterated with thermal balance until convergence in further iterations. In the utilized version of the ANDES code, the dust temperature step is recalculated again for the hydrostatic solution that fits the vertical temperature structure, assuming well-mixed small dust particles and, therefore, a constant dust-to-gas mass ratio.

The recent version of the ANDES<sub>2D</sub> code is based on a fully 2D approach and it simultaneously iterates the vertical disk structure and the chemical evolution, which allows one to accurately simulate some time-dependent effects such as luminosity outbursts in the FU Ori-type systems (Molyarova et al. 2017, 2018). However, this recent version does not feature the detailed gas thermal balance. In this study, we use the original version of ANDES with the reduced chemical network for molecular coolants and modifications to the modeling of the X-ray and cosmic ray ionization rates. The reduced chemical network consists of 63 species and 480 reactions to accurately model the abundances of C, C<sup>+</sup>, H<sub>2</sub>O, CO, CO<sub>2</sub>, OH, H<sub>2</sub>, and other simple species. It has been obtained from the full network (described in Subsection 2.2.3) by using the iterative reaction-based reduction method followed by manual tuning (Wiebe et al. 2003; Semenov et al. 2004).

Using the ANDES model, we first computed a set of disk thermo-chemical models to obtain 1+1D temperature and density structures. We assumed the stellar and disk parameters, as listed in Table 2.1. We selected a T Tauri star with a mass of  $M = 0.5 M_{\odot}$ , and we derived its effective temperature  $T_{\text{eff}} = 3820$  K and radius  $R = 1.47 R_{\odot}$  from

Table 2.1: ANDES input parameters.

Parameter	Value
$M_{\text{star}}$	$0.5 M_{\odot}$
$T_{\text{star}}$	3820 K
$R_{\text{star}}$	$1.47 R_{\odot}$
UV excess	$B_{\nu}(T_{\text{eff}} = 20000 \text{ K})$
Accretion rate	$3.6 \times 10^{-9} M_{\odot} \text{yr}^{-1}$
Dust opacity	Draine & Lee (1984)
Dust grain size	$10^{-5} \text{ cm}$
Dust-to-gas mass ratio	0.01, 0.001
Grazing angle	0.05
Gas column density at 1 au	10, 100 $\text{g cm}^{-2}$
Density power-law slope	-1

the evolutionary track model assuming an age of 2 Myr (Yorke & Bodenheimer 2008, private communication). We did not aim to qualitatively model the K5e-type AS 209 star, rather we modeled a generic T Tauri protoplanetary disk. For the UV excess, we assumed the blackbody emission with  $T_{\text{eff}} = 20000 \text{ K}$ , normalized to the total flux of blackbody radiation with  $T_{\text{eff}} = 4000 \text{ K}$ . We did not take the evolution of the stellar radius and effective temperature into account. For the dust radiative transfer and surface chemistry, we used non-evolving single-size silicate grains with a size of  $10^{-5} \text{ cm}$ . We set the dust-to-gas mass ratio to 0.01 in our reference disk model.

The disk surface density was parameterized using the following power-law distribution, without taking tapering at outer radii into account:

$$\Sigma(r) = \Sigma_{1\text{au}} \left( \frac{r}{1 \text{ au}} \right)^{-1}. \quad (2.1)$$

This approach leads to a denser outer disk and affects the integral disk properties. On the other hand, it does not affect the effect of the local substructure much. We also separately computed radii between 80 and 250 au with a 10 times lower surface density, and with a 10 times lower dust-to-gas ratio for the gap models, which is described in the next section. The summary of the adopted stellar and disk parameters is presented in Table 2.1.

## 2.2.2 ANDES post-processing

### Models with gaps

After that, we combined the vertical structures computed by ANDES for each disk radii into the three protoplanetary disk models (see Table 2.2). The first model, the so-called reference model, hereafter referred to as (R), is the disk model without any dust or gas gaps. For the other two disk models, we used the separately computed vertical structures for the radii between 80 and 250 au, and those from the reference model (R) outside of this gap. For the second model, the so-called gas-poor gap model, hereafter referred to as (A), we lowered gas and dust surface densities by a factor of 10 between 80 and 250 au, such that the dust-to-gas mass ratio remains the same inside the gap as in the reference model (R). For the third model, the so-called gas-rich gap model, hereafter referred to as (B), we only lowered the dust surface density by a factor of 10 between 80 and 250 au, such that

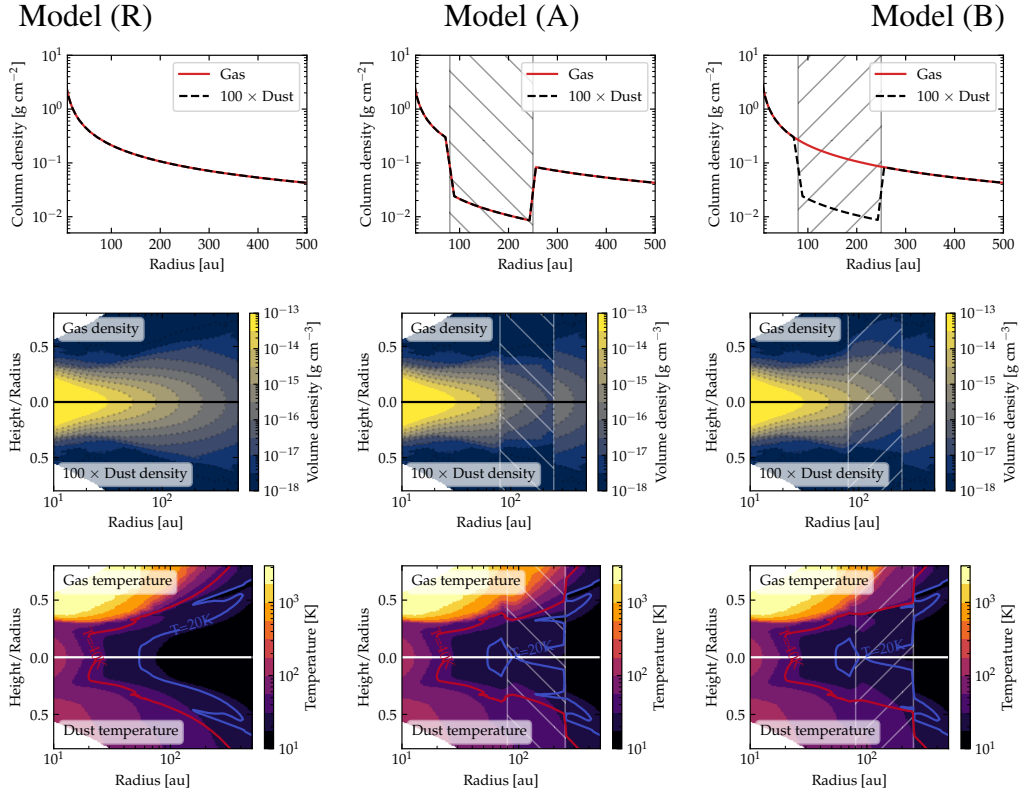


Figure 2.1: Physical structure of the three protoplanetary disk models. The left panels are for the reference model (R), the middle panels are for the gas-poor gap model (A), and the right panels are for the gas-rich gap model (B). In the upper row, the column densities of gas and dust are presented. The dust column density is multiplied by 100 for comparison purposes with the gas and the typical dust-to-gas mass ratio of 0.01. In the second row, the upper half of each panel is the gas density, and the bottom half is the dust density, multiplied by 100 for comparison. In the bottom row, the upper half of each panel is the gas temperature, and the bottom half is the dust temperature. The location of the gap is marked by a hatched rectangle. The 20 and 40 K gas temperature isotherms are shown as blue and red contour lines, respectively.

the gas surface density remains the same inside the gap as in the reference model. This setup leads to a much lower dust-to-gas mass ratio of 0.001 inside the gap in model (B). Our 1+1D approach does not include the interaction between different radii, which are treated independently; furthermore, the physical conditions and abundances at the gap's edges may not be completely feasible. We present the resulting density and thermal disk structures in Fig. 2.1. The width of the gap used in our modeling is larger than a typical gap width of  $\sim 1 - 20$  au observed in the dust continuum, but it is similar to the wide gap found in the AS 209 disk. The effects of narrower gaps of a similar depth located anywhere between 80 and 250 au on the disk physics and chemistry would be similar because of the 1+1D nature of our modeling tools.

### **X-rays, cosmic rays, and stellar wind**

Other than cosmic rays, stellar X-ray radiation is one of the primary ionization mechanisms in protoplanetary disks. X-rays are produced by the accreting gas and its interaction with magnetic fields (see Rab et al. (2018) and references therein). In addition to X-rays, it has recently been recognized that the high-energy stellar energetic particles (SEP) could also play an important role in the disk ionization (Rab et al. 2017). We added the SEP ionization using the active T Tauri model of Rab et al. (2017). While far ultraviolet (FUV) radiation dominates ionization in the disk atmosphere (Röllig et al. 2007), both X-rays and SEP are the primary ionization sources in the intermediate layers of the disk (Semenov et al. 2004). In the midplane, the ionization is dominated by the cosmic rays or the decay of short-lived radionuclides (SLRs).

The X-ray ionization rate at a specific disk location primarily depends on the X-ray flux and the hardness of the X-ray energy spectrum. To compute the X-ray flux at a given point in the disk, one should perform X-ray radiative transfer modeling. The addition of the Compton scattering is necessary for more realistic calculations of the X-ray ionization rates in the disk. However, the Monte-Carlo X-ray radiative transfer is computationally expensive.

Instead, a more conventional approach is the computation of the X-ray ray tracing on simplified 1D or 2D geometries and the further usage of parametrization to approximate the disk structure. In recent versions of the ProDiMo code, the X-ray radiative transfer was performed for every disk structure (Rab et al. 2018). In the DALI code, the Compton scattering is neglected, and the one-dimension ray tracing from a point-like stellar source is assumed (Bruderer et al. 2009).

The parametrization of the disk's X-ray irradiation given in Bai & Goodman (2009) is based on the radiative transfer model of two bremsstrahlung-emitting coronal rings located at the height of  $10 R_{\odot}$  from the rotation axis and a similar distance above and below the disk midplane. This model also takes the Compton scattering and photoionization absorption into account. Bai & Goodman (2009) followed the approach of Igea & Glassgold (1999), who studied the X-ray ionization of the inner (on the order of a few au) regions of protoplanetary disks. Igea & Glassgold (1999) found that the ionization structure can be parameterized as a function of only vertical column density for a given radius by scaling down an unattenuated X-ray flux at the disk atmosphere. We adopted the simplified approach of Bai & Goodman (2009) in our ANDES 1+1D iterative modeling of the disk structure. After the iterative calculations of the disk were finished, we utilized the more rigorous method of Bruderer et al. (2009) and recalculated the disk ionization structure, assuming a single-point X-ray source associated with the central star. The X-ray shielding of the gap by the inner disk regions was computed by the 2D ionizing radiation ray tracing without scattering.

Finally, Galactic cosmic rays (CRs) dominate the ionization rate in the disk midplanes when the local gas surface density does not exceed about  $100 \text{ g cm}^{-2}$  or when the stellar wind and magnetic mirroring are not that strong (Dolginov & Stepinski 1994; Gammie 1996; Cleeves et al. 2013; Rab et al. 2017; Padovani et al. 2018). Otherwise, in the densest disk regions shielded from CRs, the decay of SLRs plays a major role. We used the unattenuated CR ionization rate of  $1.3 \times 10^{-17} \text{ s}^{-1}$  and the SLR ionization rate of  $6.5 \times 10^{-19} \text{ s}^{-1}$  (Semenov et al. 2004). In the studied regions of our adopted disk models, neither the gas surface density nor the stellar wind is strong enough to efficiently block the CRs, so the impact of SLRs on the disk midplane ionization is negligible.

Last but not least, for each iterative modeling step, the radial CO and H<sub>2</sub> column densities were calculated. They were used to compute the UV shielding factors, using an interpolation table from Lee et al. (1996) (see also Semenov & Wiebe 2011; Visser et al. 2009).

### 2.2.3 Chemical model

Next, we used the computed physical structures of the disk and performed time-dependent chemical modeling as post-processing with the ALCHEMIC code (Semenov et al. 2010). The gas-grain network is based on the osu.2007 rate file with updates as of June 2013 from the KIDA database<sup>1</sup> (see Wakelam et al. (2012)). The network is supplied with a set of approximately 1 000 reactions with high-temperature barriers from Harada et al. (2010) and Harada et al. (2012). This network was extended by using a statistical branching approach with a set of deuterium fractionation reactions and it includes up to triply-deuterated species (see Albertsson et al. 2013, 2014b). Primal isotope exchange reactions for H<sub>3</sub><sup>+</sup>, CH<sub>3</sub><sup>+</sup>, and C<sub>2</sub>H<sub>2</sub><sup>+</sup> from Roberts & Millar (2000), Gerlich et al. (2002), Roberts et al. (2004), and Roueff et al. (2005) were included. Ortho and para forms of H<sub>2</sub>, H<sub>2</sub><sup>+</sup>, and H<sub>3</sub><sup>+</sup> isotopologs were considered. The corresponding nuclear spin-state exchange processes were added from experimental and theoretical studies (Gerlich 1990; Flower et al. 2004; Walmsley et al. 2004; Flower et al. 2006; Pagani et al. 2009; Hugo et al. 2009; Honvault et al. 2011; Sipilä et al. 2013).

The assumed grains are spherical nonporous silicate particles with the material density of  $3 \text{ g cm}^{-3}$  and a radius of  $0.1 \mu\text{m}$ . Each grain provides around  $1.88 \times 10^6$  surface sites (Biham et al. 2001). The gas-grain interactions include the freeze-out of neutral species and electrons to dust grains with a 100% sticking probability. In addition, the dissociative recombination and radiative neutralization of molecular ions on charged grains and grain recharging are taken into account. As desorption mechanisms for ices, we considered thermal, CR-, UV-driven, and reactive desorption processes. An FUV photodesorption yield of  $1 \times 10^{-5}$  was adopted. In addition, FUV-driven photodissociation reactions inside ice mantles were implemented as in Garrod & Herbst (2006) and Semenov & Wiebe (2011). Surface recombination is assumed to proceed via the classical Langmuir-Hinshelwood mechanism (e.g., Hasegawa et al. 1992). The ratio between diffusion and desorption energies of surface reactants is assumed to be 0.4. Hydrogen tunneling through rectangular reaction barriers with a thickness of  $1 \text{ \AA}$  was computed using Eq. (6) from (Hasegawa et al. 1992). For each act of surface recombination, the efficiency of reactive desorption of the reaction products directly into the gas phase was assumed to be 1% (Garrod et al. 2007; Vasyunin & Herbst 2013).

Our chemical network consists of 1268 species made of 13 elements and 38812 reactions. As initial abundances, we used the so-called low metals set of mainly atomic abundances (except H<sub>2</sub> and HD) from (Lee et al. 1998). Table 2.3 summarizes the initial

<sup>1</sup><http://kida.obs.u-bordeaux1.fr>

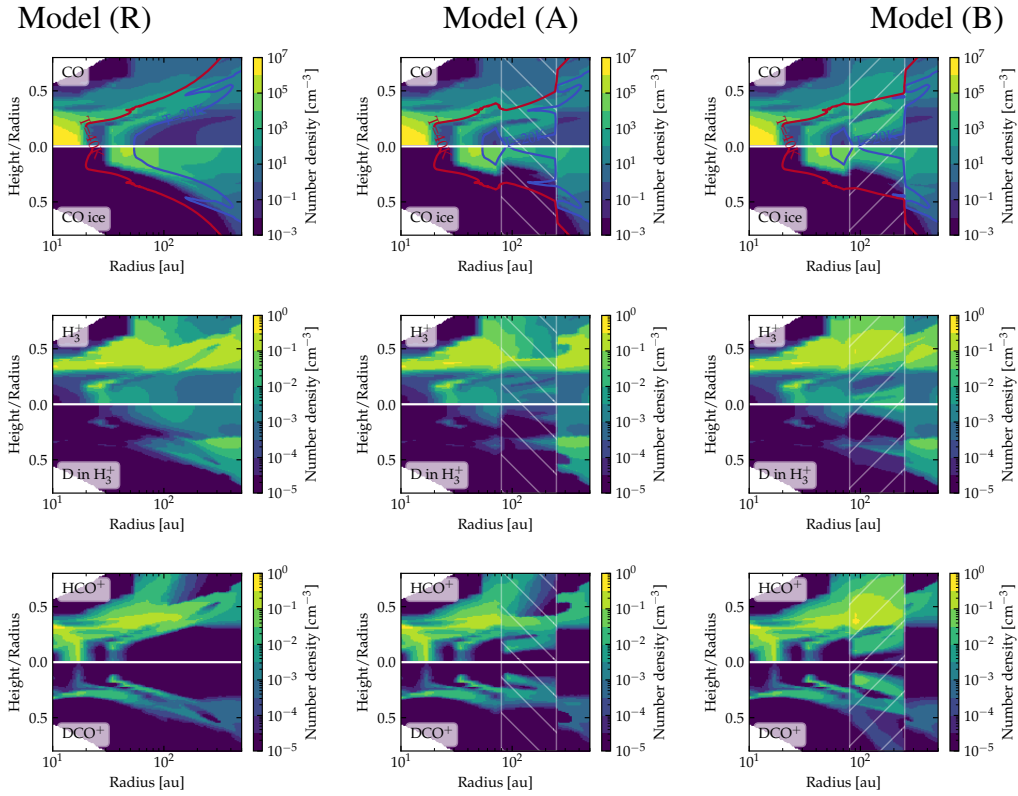


Figure 2.2: Chemical structures of the three protoplanetary disk models. The left panels are for the reference model (R), the middle panels are for the gas-poor gap model (A), and the right panels are for the gas-rich gap model (B). Different species are shown in the top and bottom halves of each panel. D in  $\text{H}_3^+$  is the total number of D atoms in  $\text{H}_3^+$  isotopologs. The location of the gap is shown as a hatched background. The gas isotherms of 20 and 40 K are shown in blue and red in the upper panels, respectively, highlighting the CO snowline location and shape.

relative abundances (wrt the total amount of hydrogen nuclei). The ALCHEMIC code and the chemical network were used to model the chemical evolution of the disk over an evolutionary time span of 1 Myr for all three physical structures that were considered.

With our large gas-grain chemistry network with deuterium fractionation, it was not practical to add another full set of  $^{13}\text{C}$  and  $^{18}\text{O}$  reactions. That is why we opted for simple scaling relations when deriving abundances of  $^{13}\text{C}$  and  $^{18}\text{O}$ -bearing isotopologs of CO and  $\text{HCO}^+$ . We assumed that the  $\text{H}^{13}\text{CO}^+$  abundances are equal to 1% of the  $\text{HCO}^+$  abundances, while  $\text{C}^{18}\text{O}$  abundances are equal to 0.2% of the  $^{12}\text{CO}$  abundances (Wilson & Rood 1994). This simplistic approach does not take selective photodissociation of CO isotopologs and isotopic  $^{13}\text{C}$ -exchange reactions into account, which may lead to uncertainties in the adopted  $\text{H}^{13}\text{CO}^+$  and  $\text{C}^{18}\text{O}$  abundances by a factor of 3–5 (e.g., Visser et al. 2009; Miotello et al. 2014, 2018). Since we mainly focus on analyzing the behavior of abundance and line ratios, rather than absolute values, such a discrepancy should not affect the major underlying trends.

## 2.2.4 Line radiative transfer

To test whether the radial variations in the chemical structures could become visible in the emission images, we have used the computed physical and chemical structures of the disk and performed LTE line radiative transfer with LIME v1.9.4 (LIne Modeling Engine) by

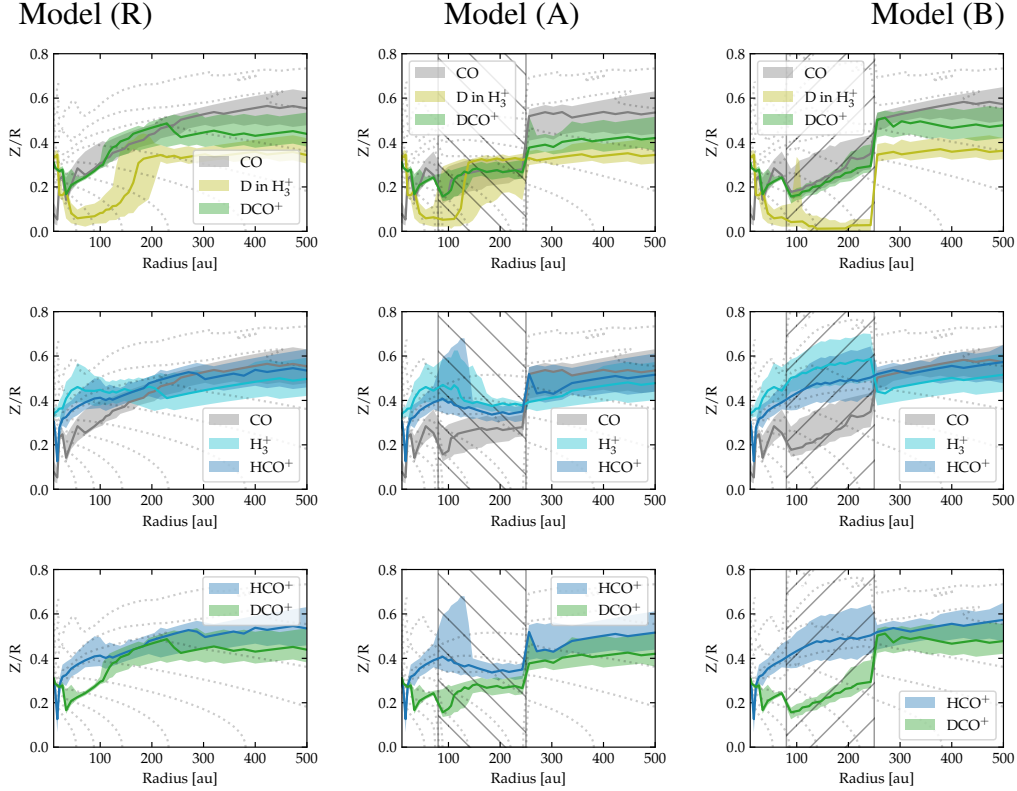


Figure 2.3: Vertical mass distribution of  $\text{H}_3^+$ , deuterium in  $\text{H}_3^+$  isotopologs,  $\text{CO}$ ,  $\text{HCO}^+$ , and  $\text{DCO}^+$  as a function of the radius. The color-filled stripes show the vertical location of the 25, 50, and 75 mass percentiles (bottom border, median line, and top border, respectively). Half of the total molecular gas mass is located within the corresponding stripe. The dotted contour lines show the gas isodensities from  $1 \times 10^{-18}$  to  $1 \times 10^{-14} \text{ g cm}^{-2}$  with a logarithmic step of  $10^{0.5}$ , which is the same as in the top panel of Fig. 2.1. The left panel is the reference model (R), the middle panel is the gas-poor gap model (A), and the right panel is the gas-rich gap model (B). The location of the gap is shown as a hatched background. When molecules are co-spatial, their mass distributions overlap (e.g., as in the case of deuterated isotopologs of  $\text{H}_3^+$  in the model (A)).

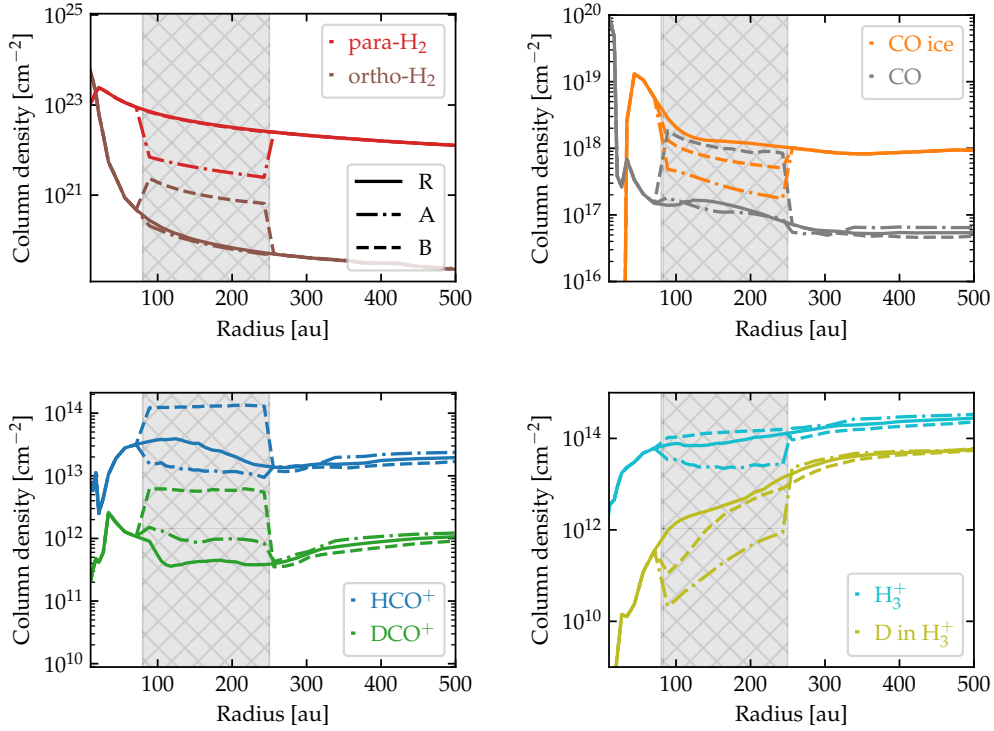


Figure 2.4: Radial profiles of the vertical column densities of the selected molecules. D in  $\text{H}_3^+$  is the total number of D atoms in  $\text{H}_3^+$  isotopologs. The solid lines correspond to the reference model (R), the dash-dotted lines to the gas-poor model (A), and the dashed lines to the gas-rich model (B). The location of the gap is shown by the gray rectangle.

Brinch & Hogerheijde (2010). We used the corresponding spectroscopic and collisional rate data from the Leiden Atomic and Molecular Database (LAMDA: Schöier et al. 2005). Other key input parameters for LIME are listed in Table 2.4.

We tested the LTE line radiative transfer calculations, both with and without the dust opacities taken into account, and we did not notice any significant differences in the continuum-subtracted line emission for the low-J  $\text{HCO}^+$  and CO isotopolog lines in the studied low-density regions of the disk. As the dust continuum is usually subtracted from the science-ready observational data and since the LIME computations, which include dust opacities, take much longer, we only show the results obtained for the pure gas emission case. For each synthetic image, we ran 50 instances of LIME and then averaged them to reduce the noise. As global emission distributions look similar for the J=5–4, 4–3, and 3–2 transitions, we focus on the J=3–2 results.

Table 2.2: Properties of the disk models.

Model	Gas gap [au]	Gas column density (inside the gap)	Dust gap [au]	Dust-to-gas mass ratio (inside the gap)
(R) Reference disk	no	$100 \text{ g cm}^{-2} \left(\frac{r}{1 \text{ au}}\right)^{-1}$	no	0.01
(A) Gas- and dust-poor gap	80 – 250	$0.1 \times$ (Reference)	80 – 250	0.01
(B) Gas-rich, dust-poor gap	no	(Reference)	80 – 250	0.001

Table 2.3: Initial Chemical Abundances.

Species	Abundance $n(\text{X}) / n(\text{H})$	Species	Abundance $n(\text{X}) / n(\text{H})$
ortho- $\text{H}_2$	$3.75 \times 10^{-1}$	S	$9.14 \times 10^{-8}$
para- $\text{H}_2$	$1.25 \times 10^{-1}$	Si	$9.74 \times 10^{-9}$
He	$9.75 \times 10^{-2}$	Fe	$2.74 \times 10^{-9}$
O	$1.80 \times 10^{-4}$	Na	$2.25 \times 10^{-9}$
C	$7.86 \times 10^{-5}$	Mg	$1.09 \times 10^{-8}$
N	$2.47 \times 10^{-5}$	Cl	$1.00 \times 10^{-9}$
HD	$1.55 \times 10^{-5}$	P	$2.16 \times 10^{-10}$

Table 2.4: LIME input parameters.

Parameter	Internal name	Value
Minimal spatial scale	minScale	1 au
Number of grid points	pIntensity	$10^5$
Number of sink points	sinkPoints	3000
Velocity resolution	velres	$20 \text{ m s}^{-1}$
Distance to the source	distance	100 pc

## 2.3 Results

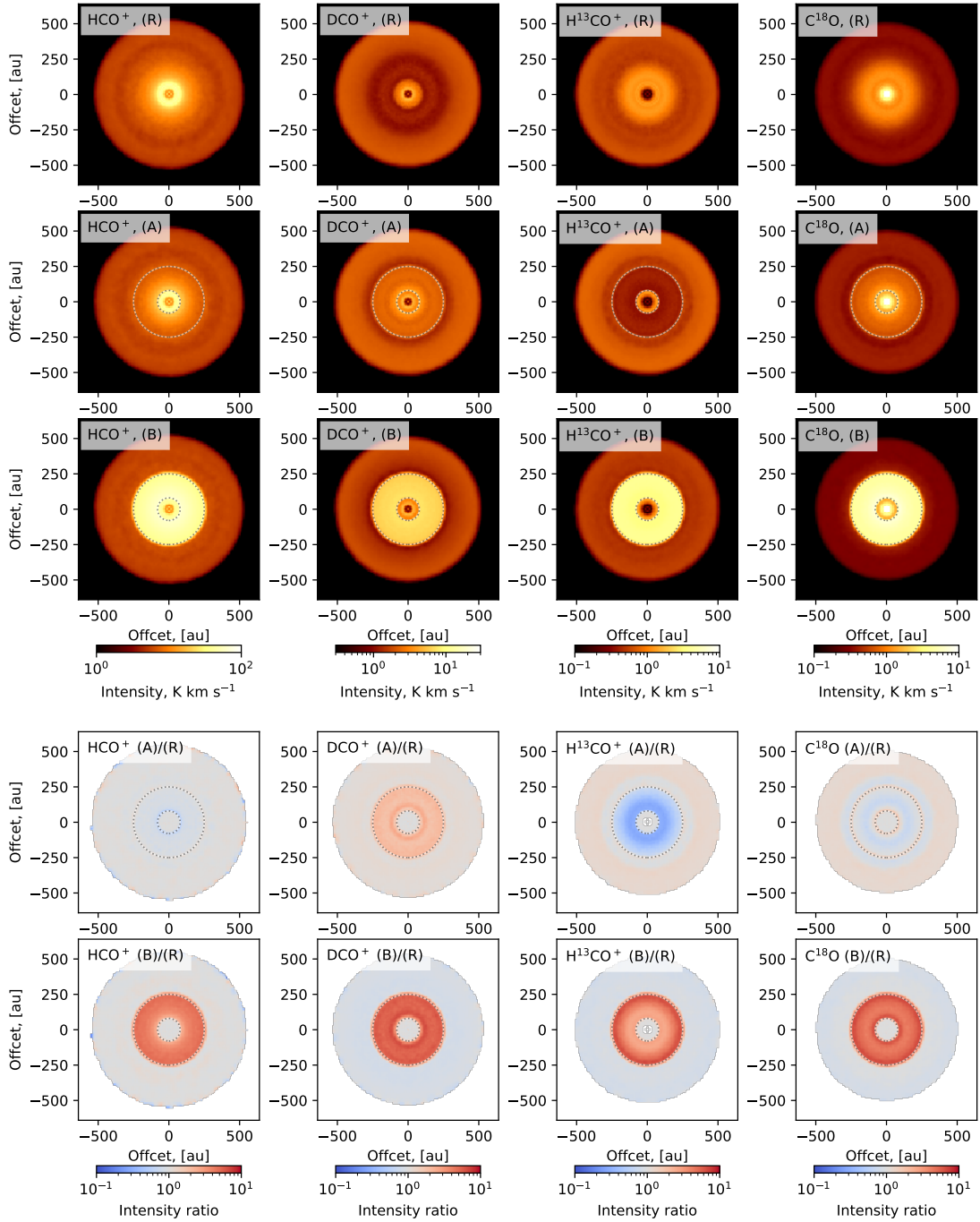


Figure 2.5: Integrated intensity 0th-moment maps. From left to right:  $\text{HCO}^+$ ,  $\text{DCO}^+$ ,  $\text{H}^{13}\text{CO}^+$ , and  $\text{C}^{18}\text{O}$ , all  $J=3-2$ . From the top to the bottom row: the reference model (R), the gas-poor gap model (A), the gas-rich model (B), the ratio (A)/(R), and the ratio (B)/(R). The gap boundaries are marked by the two dotted lines. The optically thick  $\text{HCO}^+$  emission is not significantly affected by the presence of the gas-poor gap. In contrast, the  $\text{C}^{18}\text{O}$  and particularly  $\text{H}^{13}\text{CO}^+$  intensities decrease inside the gas-poor gap, while the  $\text{DCO}^+$  intensity increases inside this gap.

### 2.3.1 Reference model (R)

The reference model does not have any density gaps. Its gas surface density is set by the power law (Eq. 2.1) with  $\Sigma_{1\text{au}} = 100 \text{ g cm}^{-2}$ . This type of monotonous surface density profile still leads to rather nonmonotonous abundance structures (see Fig. 2.2). This nonhomogeneous abundance distribution is typical of disk models with gas-grain chemistry, which are sensitive to the local variations in temperature, density, ionization, and high-energy radiation intensities (e.g., Semenov & Wiebe 2011).

In our reference disk model, the self-shielded CO extends far into the disk atmosphere, until the height-to-radius ratio of  $\sim 0.5$  and above (Figs. 2.2 & 2.3). The CO snowline is located at about 30 au in the midplane. Inside the radius of 20 au, the gas-phase CO exists all the way through the disk down to the midplane. The CO molecules are efficiently converted to CO<sub>2</sub> in a region between  $\sim 20 - 30$  au, causing the gas-phase CO abundances to decrease at height-to-radius ratio below  $\sim 0.2$ . Outside of 30 au, the gas-phase CO resides in the molecular layer above the height and radius scales of  $\sim 0.1 - 0.3$ . The CO ice is mainly concentrated in the midplane at  $r \gtrsim 30$  au, and the height-to-radius ratio below  $\sim 0.3$ .

The distribution of the H<sub>3</sub><sup>+</sup> isotopologs sensitively depends on the local ionization rate and the local gas density, since its primary production mechanism involves the ionization of H<sub>2</sub> followed by the ion-molecule reactions of H<sub>2</sub><sup>+</sup> with H<sub>2</sub>. Consequently, in the dense midplane, where ionization rates are low, the abundances of H<sub>3</sub><sup>+</sup> isotopologs decrease, but they never disappear entirely as they do for the gas-phase CO. A key difference between the main H<sub>3</sub><sup>+</sup> isotopolog and its minor D-isotopologs is that the molecular layer of the deuterated H<sub>3</sub><sup>+</sup> ions is shifted closer to the cold disk midplane compared to that of H<sub>3</sub><sup>+</sup> (Fig. 2.3, left panels). This is because unlocking D from HD via deuterium exchange reactions most rapidly proceeds at temperatures below  $\sim 20 - 100$  K and is particularly efficient when CO is frozen out and when H<sub>2</sub> mainly exists in the para form (e.g., Flower et al. 2006; Albertsson et al. 2013; Sipilä et al. 2013; Teague et al. 2015; Huang et al. 2017). This leads to a situation when abundances of, for example, H<sub>2</sub>D<sup>+</sup> can become comparable to the H<sub>3</sub><sup>+</sup> abundances in some disk locations, while their vertically-integrated column density would still differ by a factor of  $\sim 10 - 100$  (Fig. 2.2 and 2.4, bottom left panels). Panels with the label "D in H<sub>3</sub><sup>+</sup>" show the total number of D atoms in H<sub>3</sub><sup>+</sup> isotopologs (H<sub>2</sub>D<sup>+</sup>, HD<sub>2</sub><sup>+</sup>, and D<sub>3</sub><sup>+</sup>).

The global distribution of the HCO<sup>+</sup> isotopologs is determined by the distribution of their parental species, the gaseous CO and the H<sub>3</sub><sup>+</sup> isotopologs. In general, the HCO<sup>+</sup> and DCO<sup>+</sup> abundances do follow the H<sub>3</sub><sup>+</sup> and CO gas-phase distributions and they are absent in the CO depletion region. However, there are still major differences between these ions. First, the DCO<sup>+</sup> molecular layer is, by necessity, co-spatial with the upper part of the H<sub>3</sub><sup>+</sup> deuterated isotopolog layer, where CO is still not completely frozen out (Fig. 2.3, top left panel). Second, because of that, the DCO<sup>+</sup> layer is located beneath the HCO<sup>+</sup> layer and thus probes slightly different physical conditions in the disk (Fig. 2.3, bottom left panel).

As a result of localized variations in the chemical structure, the vertical column densities of the HCO<sup>+</sup> isotopologs and other key species in the gap-free reference model do show the presence of weak chemical gaps at outer radii or  $r > 100$  au (Fig. 2.4). Furthermore, these chemical gaps affect the line excitation and appear as emission gaps on the ideal synthetic spectra for the reference disk model with the monotonous global physical structure (see Fig. 2.5). The appearance of these chemical gaps is different for various HCO<sup>+</sup> isotopologs and C<sup>18</sup>O, and it depends on their line optical depths and/or the location of the emitting layer. Thus, when taking molecular emission gaps at face value, one could misinterpret the data as being indicative of real physical gaps in the disk gas, while it may not be the case.

### 2.3.2 Gas-poor model (A)

The lower amount of dust and gas leads to higher temperatures, larger pressure scale heights, and hence lower densities in the gas-poor gap model compared to the reference model (Fig. 2.1, middle panels). The reduced opaqueness of the disk matter in the gas-poor gap results in a vertical shift of the molecular layers down toward the midplane (Figs. 2.2 and 2.3, middle panels). While the vertical column density of  $\text{H}_2$  and  $\text{H}_3^+$  and the total (ice and gas) CO concentration decrease by a factor of  $\sim 10$  inside the gap, the vertical column density of gaseous CO almost remains intact. The balance between the CO photodissociation and freeze-out is similar in the shifted CO layer inside the gap, just as in the gap-free reference model (Fig. 2.4, top right panel). Naturally, the total amount of CO ice, which dominates CO concentration outside the CO snowline, is lower in the gas-poor gap model (A) compared to the reference model (R).

This vertical shift of the CO molecular layer in the gas-poor gap brings it closer to the molecular layer of the  $\text{H}_3^+$  D-isotopologs, but moves it away from the main  $\text{H}_3^+$  molecular layer (Fig. 2.3, middle panels). It leads to an increase in the rate of the  $\text{DCO}^+$ -forming reaction, which is proportional to a product of deuterated isotopologs of  $\text{H}_3^+$  and CO volume densities. However, it also leads to an opposite effect for the  $\text{HCO}^+$  abundances. Consequently, the column density of  $\text{HCO}^+$  decreases by a factor of  $\sim 3$ , whereas the column density of  $\text{DCO}^+$  increases by a similar factor (Fig. 2.4, bottom left panel).

These chemical effects remain visible in the emission maps. Therefore, the gas-poor gap model leads to weaker  $\text{H}^{13}\text{CO}^+$  emission inside the gap, while the chemically-unaffected, optically thin  $\text{C}^{18}\text{O}$  and optically-thick  $\text{HCO}^+$  emission remain relatively unaffected. In contrast, the  $\text{DCO}^+$  emission increases inside the gas-poor gap (Fig. 2.5). This effect is very similar to the observed behavior of  $\text{DCO}^+$ ,  $\text{H}^{13}\text{CO}^+$ , and  $\text{C}^{18}\text{O}$  in AS 209 (Huang et al. 2017; Favre et al. 2019).

### 2.3.3 Gas-rich, dust-poor model (B)

Similarly to the gas-poor model (A), the disk model where the gap is only devoid from dust, model (B) shows higher temperatures and slightly lower volume densities compared to the reference model (R) (Fig. 2.1, right panels). The smaller dust column density in the gas-rich gap leads to lower extinction of the ionizing and dissociating radiation and makes molecular freeze-out less efficient. This also shifts the molecular layers closer to the midplane, as in the previous gap model (Figs. 2.2 and 2.3, right panels).

The dust-depleted gap with the same amount of gas as in the reference model leads to about a 10 times higher column density of gaseous CO and a  $\sim 2 - 3$  times lower column density of the CO ice (Fig. 2.4). The higher concentration of gaseous CO in the cold midplane region makes reactions with the  $\text{H}_3^+\text{D}$ -isotopologs faster, while a higher concentration of CO in the molecular layer also boosts the production of  $\text{HCO}^+$ . Thus, the model with the dust-poor gap leads to a similar increase in the column densities of  $\text{HCO}^+$ ,  $\text{DCO}^+$ , and CO. This strong increase in the molecular concentrations is imprinted into the corresponding increase in the  $\text{HCO}^+$ ,  $\text{DCO}^+$ , and  $\text{C}^{18}\text{O}$  emission in the dust-poor gap (Fig. 2.5). Thus, using the single ALMA Band 6 or NOEMA Band 3 spectral setups with  $\text{DCO}^+$  and the CO isotopolog or the two setups with the  $\text{HCO}^+$ ,  $\text{H}^{13}\text{CO}^+$ , and  $\text{DCO}^+$  ions, one could distinguish between gas-poor and dust-poor disk gaps and estimate the overall depletion of gas and/or dust there.

## 2.4 Discussion

### 2.4.1 Model uncertainties and future development

The version of ANDES used in this study simulates each disk radius independently, thus limiting us in the modeling approaches for ionizing radiation transport that is consistent with the thermal structure. The X-rays and stellar energetic particles from the star cause significant heating in the gas, affecting its vertical structure and ionization fraction. The 2D nature of a gap must have an impact on the underlying chemical structure and thus it should also affect the gas thermal balance. Consistent 2D modeling with accurate modeling of the gas thermal balance will be implemented in the future 2D version of ANDES<sub>2D</sub>, first presented in Molyarova et al. (2017, 2018), which is being actively developed.

From the chemical point of view, the calculated abundances of simple species in our model suffer from intrinsic uncertainties due to the reaction rate uncertainties, which are on the order of a factor of 3 for  $\text{HCO}^+$  isotopologs and less than a factor of 2 for the gas-phase CO (Vasyunin et al. 2008; Albertsson et al. 2013; Iqbal et al. 2018). In addition, our chemical network does not include reactions involving isotopologs except for deuterium, and hence we had to rescale the abundances of  $\text{HCO}^+$  and CO to get the  $\text{H}^{13}\text{CO}^+$  and  $\text{C}^{18}\text{O}$  abundances. This simplification may introduce additional chemical uncertainty by a factor of 2-3 for both these minor isotopologs. The main reason for that is the computational demands required for our model with deuterium fractionation. A further increase in the number of species from  $\sim 1250$  in the current version to  $> 2000 - 5000$  species in the network that also includes key  $^{13}\text{C}$ - and  $^{18}\text{O}$ -isotopologs would increase the computation time of the chemical evolution by at least a factor of 10, and we decided to leave the more detailed analysis for future studies.

### 2.4.2 Comparison with previous studies

Carney et al. (2018) have studied the gap at 40–60 au between the two dusty rings in the protoplanetary disk around HD 169142. In contrast to our case,  $\text{DCO}^+$   $J=3-2$  emission intensity decreases in this gap. The thermo-chemical structure of the HD 169142 disk was simulated with the DALI code (Bruderer et al. 2014). To reproduce the observed behavior, Bruderer et al. (2014) assumed the low gas densities in both the gap and the inner dust ring, similar to our gas-poor model (A). While the authors do not show the  $\text{HCO}^+$  radial profiles, the behavior of the  $\text{DCO}^+$  emission alone is neither consistent with the  $\text{DCO}^+$  observations of AS 209 nor with our modeling. The first reason for this inconsistency could be a stronger gas density depletion, estimated as a factor of 40 in their model, in comparison to our factor of 10 depletion. In their case, the  $\text{DCO}^+ / \text{H}_2$  ratio inside the gap is lower by a factor of  $\sim 20$  in comparison with the outer dust ring. This is somewhat similar to the increase we have in the gas-poor model (A). The second major difference is that this is a Herbig Ae disk (the stellar mass is  $1.65 M_\odot$ ). Compared to our cold T Tauri disk with the CO snowline located at  $\sim 30$  au, the CO snowline in the HD 169142 disk is likely located beyond 50 au. Thus, the gap at 40–60 au in HD 169142 could be inside the CO snowline and not outside, as in our model.

Teague et al. (2017) have studied the dip in the CS emission at the radius of  $r \sim 80 - 90$  au in TW Hya, which coincides with one of the (sub)mm dust gaps in this disk. They computed a set of models with different maximal depths of the Gaussian gap ( $\Sigma_x/\Sigma_A = 0.3(B), 0.55(C), 1(D)$ ). They considered several cases of the gap, both with and without gas inside. The model that qualitatively reproduces the observed CS radial profile, especially its second derivative, was model C with an intermediate gap depth.

The behavior of the CS emission in TW Hya is similar to that of  $\text{HCO}^+$  in our model. In Fig. 2.6 we show the CS column density derived from our model in comparison with  $\text{HCO}^+$  and  $\text{DCO}^+$ . CS is more sensitive to the lowering of the dust-to-gas ratio because it unlocks more carbon from CO by photodissociation and due to less efficient freeze out. In the gas-poor gap model (A), there is no significant difference in the CS abundance with respect to the reference model (R). On the other hand, in the case of the gas-rich gap model (B), the CS abundance increases stronger than the abundance of  $\text{HCO}^+$  with respect to the reference model (R). It is also consistent with the results of Teague et al. (2017) for their gas-rich model *Cd*. Thus, CS, together with  $\text{DCO}^+$ , can also serve as a probe for gas depletion in disk gaps if  $\text{H}^{13}\text{CO}^+$  data are not available.

Finally, Favre et al. (2019) performed the thermo-chemical modeling to fit the observed CO isotopologs emission in AS 209. For the outer gap at  $\sim 100$  au, they modeled the depletion of both gas and dust. Unlike this work, they assumed that the dust surface density is depleted by a factor of 100, while the gas surface density is depleted by only a factor of 2.5 – 10. Our results are consistent with their modeling results, as the stronger gas depletion reproduces the CO observations in the gap better. While they have shown the ALMA data for the  $\text{DCO}^+$   $J=3-2$  emission, the modeling involving deuterated chemistry has been left for the forthcoming paper. The azimuthally averaged  $\text{DCO}^+$  and  $\text{C}^{18}\text{O}$  emission line profiles and the location of the assumed gaps are shown in Fig. 2.7. The profiles were normalized to have the same slope in the outer disk. The increase in the  $\text{DCO}^+$  flux and the decrease in  $\text{C}^{18}\text{O}$  in comparison to their outer disk slope at the location of the gaps are clearly visible, as in our gas-poor model (A) (Fig. 2.5, second and fourth rows).

However, our modeling does not fit the AS 209 observations quantitatively. The stellar mass of  $0.5 M_{\odot}$  and thus the relatively low luminosity that we adopted in our models are typical for low-mass T Tauri stars. However, the type K4-5 AS 209 star is more luminous and massive and its disk is likely warmer than our disk models (Teague et al. 2018). Compared to our disk models, the CO snowline in the AS 209 disk is located at  $\sim 30-40$  au (or about 10 au farther out from the central star). Still, it does not change the main conclusion of our study because the outer gap in AS 209 is located outside of the CO snowline, as in our models, leading to similar chemical effects for the  $\text{HCO}^+$  isotopologs.

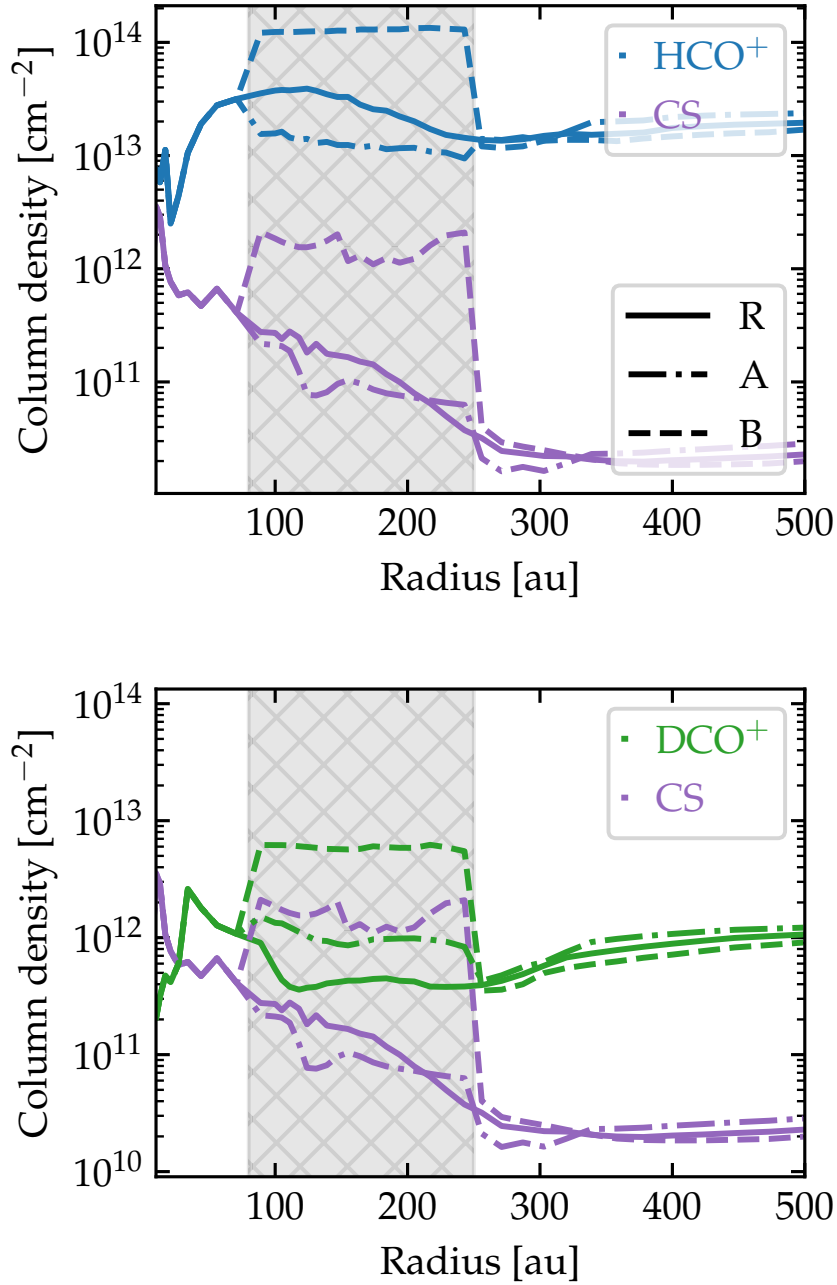


Figure 2.6: Column densities of CS (purple) in comparison with the  $\text{HCO}^+$  (blue) and  $\text{DCO}^+$  (green) column densities. The solid line denotes the reference model (R), the dash-dotted line is the gas-poor model (A), and the dashed line is the gas-rich model (B). The location of the gap is shown by the gray box.

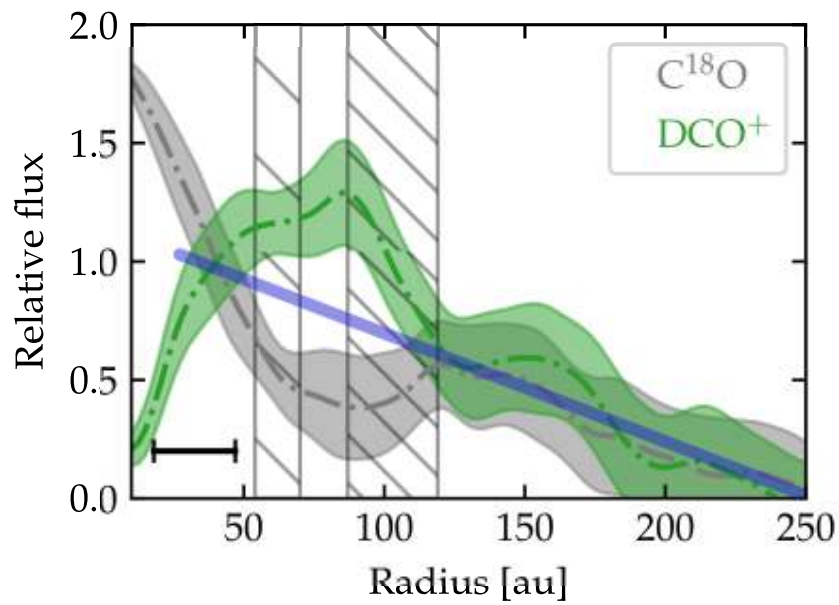


Figure 2.7: Azimuthally averaged profiles of  $DCO^+$  (green) and  $C^{18}O$  (gray) emission line fluxes from Favre et al. (2019). The profiles were normalized to have the same slope outside of the gap (120 - 250 au); the slope is shown in blue. There is an increase in  $DCO^+$  emission and a decrease in  $C^{18}O$  emission intensity at the gap location in comparison with it. In the bottom left corner of the image, the beam size of  $0.23''$  is shown. The locations of the gaps are shown by the hatched boxes.

## 2.5 Conclusions

We present detailed physical-chemical and line radiative transfer simulations of protoplanetary disks, both with and without a wide gap. For that, we used the ANDES thermochemical model to calculate 1+1D thermal and density disk structures and included various ionization sources (FUV, X-rays, SEP, CRs, and SLRs). Next, we used the gas-grain chemical code ALCHEMIC with a deuterated network to calculate molecular abundances in the disk. Finally, we utilized LIME for the line radiative transfer to produce the ideal synthetic images in molecular lines of the  $\text{HCO}^+$  isotopologs and  $\text{C}^{18}\text{O}$ . Three disk models were considered: the reference gap-free model, the model with the gas-poor gap where both gas and dust surface densities are depleted by a factor of 10, and the gas-rich gap model where solely the dust surface density is depleted by a factor of 10.

Our simulations reveal that in using the  $\text{HCO}^+$  and  $\text{CO}$  isotopologs, one could observationally distinguish between various types of the disk gaps (gas-poor versus gas-rich). The most convenient proxy of the gas or dust depletion in the disk gaps is either the  $\text{DCO}^+/\text{H}^{13}\text{CO}^+$  and  $\text{DCO}^+/\text{HCO}^+$  line ratios (using two ALMA Band 6 or NOEMA Band 3 setups) or the  $\text{DCO}^+/\text{C}^{18}\text{O}$  line ratio (using single ALMA Band 6 or NOEMA Band 3 spectral setups). Together with high-resolution dust continuum data, these ratios allow one to estimate the degree of the gas or dust depletion in the disk gaps. Namely, if most of the emission lines appear brighter inside the (sub)mm dust gap, especially  $\text{H}^{13}\text{CO}^+$ , it means that the gas in the gap is not strongly depleted. In contrast, if  $\text{C}^{18}\text{O}$  or  $\text{H}^{13}\text{CO}^+$  emission decreases while the  $\text{DCO}^+$  emission increases inside the gap, it means that the disk gap is substantially depleted in both gas and dust. Finally, the results of our study using the gas-poor disk model are in accordance with the ALMA observations of AS 209, where  $\text{C}^{18}\text{O}$  and  $\text{DCO}^+$  emission inside the outer  $\sim 100$  au gap shows the opposite behavior. Thus, using intensity ratios of  $\text{DCO}^+$  and  $\text{C}^{18}\text{O}$  or the  $\text{HCO}^+$  isotopologs, one might get invaluable information about the disk gap physics and the gap clearing mechanisms.

## Acknowledgements

The authors thank Cecile Favre for sharing the azimuthally averaged emission line profiles for AS 209 ALMA observations. The authors acknowledge the Python open-source community. This work was done using the open-source packages NumPy, SciPy, AstroPy, and Matplotlib. D.S. acknowledges support by the Deutsche Forschungsgemeinschaft through SPP 1833: “Building a Habitable Earth” (SE 1962/6-1). V.A. acknowledges the support of the Large Scientific Project of the Russian Ministry of Science and Higher Education “Theoretical and experimental studies of the formation and evolution of extra-solar planetary systems and characteristics of exoplanets” (project No. 13.1902.21.0039). T.H. acknowledges support from the European Research Council under the Horizon 2020 Framework Program via the ERC Advanced Grant Origins 83 24 28. This research has made use of NASA’s Astrophysics Data System Bibliographic Services.

## **Chapter 3**

**Lack of other molecules in CO-rich debris disks: Is it primordial or secondary gas?**

---

The nature of the gas in CO-rich debris disks remains poorly understood, as it could either be a remnant from the earlier Class II phase or of secondary origin, driven by the destruction of icy planetesimals. The aim of this work was to elucidate the origin of the gas content in the debris disks via various simple molecules that are often detected in the less-evolved Class II disks.

We present millimetre molecular line observations of nine circumstellar disks around A-type stars: four CO-rich debris disks (HD 21997, HD 121617, HD 131488, HD 131835) and five old Herbig Ae protoplanetary disks (HD 139614, HD 141569, HD 142666, HD 145718, HD 100453). The sources were observed with the Atacama Large Millimeter/submillimeter Array (ALMA) in Bands 5 and 6 with 1–2'' resolution. The Herbig Ae disks are detected in the CO isotopologs, CN, HCN, HCO<sup>+</sup>, C<sub>2</sub>H, and CS lines. In contrast, only CO isotopologs are detected in the debris disks, showing a similar amount of CO to that found in the Herbig Ae protoplanetary disks.

Using chemical and radiative transfer modelling, we show that the abundances of molecules other than CO in debris disks are expected to be very low. We consider multiple sets of initial elemental abundances with various degrees of H<sub>2</sub> depletion.

We find that the HCO<sup>+</sup> lines should be the second brightest after the CO lines, and that their intensities strongly depend on the overall CO/H<sub>2</sub> ratio of the gas. However, even in the ISM-like scenario, the simulated HCO<sup>+</sup> emission remains weak as required by our non-detections.

*Published as Smirnov-Pinchukov et al. (2022b) in MNRAS by Grigorii V. Smirnov-Pinchukov, Attila Moór, Dmitry A. Semenov, Péter Ábrahám, Thomas Henning, Ágnes Kóspál, A. Meredith Hughes, and Emmanuel di Folco. TH was the principal investigator of the observational proposals, with other authors, except for GS, being co-investigators. AM has performed the data reduction, line flux extraction, and provided an overview of the field for the introduction. DS has developed the earlier version of the code ALCHEMIC used in the project. All co-authors have contributed to the discussions of the methods and the results. I have performed chemical and radiative transfer, partially based on the software developed for Chapter 2, compared the line fluxes with the model predictions, prepared the figures.*

*techniques: interferometric – circumstellar matter – stars: individual: HD 21997, HD 121617, HD 131488, HD 131835, HD 141569, HD 100453, HD 139614, HD 142666, HD 145718 – stars: early-type*

---

## 3.1 Introduction

Recent line observations at millimetre wavelengths, mostly carried out with the ALMA interferometer, have revealed the presence of CO gas around about one and half dozen main-sequence stars known to harbour optically thin circumstellar debris dust material (Hughes et al. 2018). The observed dust and gas are at least partially co-located at a radial distance of tens of astronomical units (au) from the host stars. The derived CO masses display a large spread of at least five orders of magnitude, with roughly bimodal distribution. While about half of the sample has a low CO mass of  $\lesssim 10^{-4} M_{\oplus}$ , there are at least six disks with the CO mass  $> 0.01 M_{\oplus}$ , a value that overlaps with that of the more-evolved, less massive protoplanetary disks. The CO-rich debris disks are found exclusively around young (10–50 Myr) A-type stars (Kóspál et al. 2013; Moór et al. 2017, 2019). The host stars of disks with lower CO content show a greater diversity: their spectral types range between A and M, and though this subsample is also predominantly young (10–50 Myr, Dent et al. 2014; Lieman-Sifry et al. 2016; Marino et al. 2016; Matrà et al. 2019), it includes two older systems, Fomalhaut and  $\eta$  Crv with ages of 0.44 Gyr and 1–2 Gyr, respectively (Marino et al. 2017; Matrà et al. 2017).

Dust grains in debris disks are thought to be derived from collisions of larger solids up to the size of planetesimals (Wyatt 2008; Hughes et al. 2018). The emerging second-generation small dust particles are continuously removed from the system by interaction with the stellar radiation and the possible stellar wind. If the planetesimals are made not only of rock but contain also ice, their collisions and erosion can lead to the liberation of different gas molecules (Zuckerman & Song 2012; Kral et al. 2017). The lifetime of the released gas molecules in debris disks is limited due to rapid photodissociation in the absence of large amount of opaque dust grains. Considering only UV photons from the interstellar radiation field (ISRF), the photodissociation lifetime of unshielded CO molecules is only  $\sim 120$  yr (Visser et al. 2009; Heays et al. 2017). With such a short lifetime, only the gas content of disks with lower CO masses could be explained within the framework of secondary gas disk models.

However, as recent studies demonstrated (Kral et al. 2019; Cataldi et al. 2020; Marino et al. 2020), assuming sufficiently high (but still realistic) gas production rates from the icy bodies, neutral atomic carbon gas – mainly produced via photodissociation of CO and CO<sub>2</sub> – can become optically thick for UV photons that otherwise would dissociate CO molecules. This extra shielding by the carbon gas prolongs the photodissociation lifetime of CO significantly (Rollins & Rawlings 2012), allowing larger CO masses to accumulate in debris disks. At sufficiently high densities, self-shielding of CO gas becomes important too, further increasing the lifetime of the CO molecules in these optically thin disks. A detailed modelling of these shielding processes shows that even the secondary gas scenario may work for explaining the formation of the CO-rich debris disks (e.g. Kral et al. 2019; Moór et al. 2019; Marino et al. 2020).

Debris disks emerge after the dispersal of Class II protoplanetary disks which are made of gas-rich primordial material. Considering that all known CO-rich debris disks are young and probably represent the very early phase of debris disk evolution, Kóspál et al. (2013) raised an alternative scenario (see also Péricaud et al. 2017; Nakatani et al. 2021) that CO-rich debris disks actually have a hybrid nature, where secondary debris dust and long-lived residual primordial gas from the preceding Class II disk phase coexist. In this model, the necessary shielding of CO is related to the presence of leftover H<sub>2</sub> molecules. Should such hybrid disks exist, it would imply that during the transition from protoplanetary to debris disk the evolution of the gas and dust components can be decoupled from each other. The origin of gas in the CO-rich debris disks is still under

debate, with recent observational pieces of evidence suggesting that in some disks, the gas could indeed be of second generation (e.g., Hughes et al. 2017; Kral et al. 2017, 2019).

One possibility to decide which of the above scenarios works would be to investigate the chemistry in the CO-rich disks. Whatever the origin of the gas in the CO-rich debris disk is, CO may not be the only abundant gas component. In younger, less-evolved Class II protoplanetary disks a number of major C-, O-, N-, S-bearing polyatomic molecules have also been detected (e.g. Dutrey et al. 2014a; Öberg & Bergin 2021; Pegues et al. 2021). In our Solar System, the primitive bodies such as comets have partly retained the primordial volatile matter left from its formation epoch. The cometary ices are mainly made of water, carbon monoxide, and carbon dioxide. In addition to these constituents, about two dozen other molecules (e.g. CH<sub>4</sub>, C<sub>2</sub>H<sub>2</sub>, H<sub>2</sub>CO, HCN) with lower abundances have been detected in cometary atmospheres (Bockelée-Morvan & Biver 2017). The gas mixture of a secondary disk is expected to contain the same species, complemented with their photodissociation products. The relative proportions of the individual constituents depend on the ice composition of the local exocomets, the mechanism that leads to the gas release, the UV radiation environment, and the shielding efficiency.

Contrary to this, the gas mixture in a hybrid disk is thought to be dominated by the long-lived primordial H<sub>2</sub> molecules. In addition, there could be different primordial residual gas species as well as secondary gas components released from the icy comets situated in the disk. The presence of the large amount of H<sub>2</sub> in such a disk can lead to a significantly different chemical environment than in an H<sub>2</sub>-poor secondary gas disk.

Detecting other molecules than CO and thus better understanding the composition of the gas in debris disks can help us to elucidate the origin of the gas and, if the gas proves to be of secondary origin, to constrain the ice abundance of exocomets. Motivated by these opportunities, there already have been several attempts to survey the molecular content of gas-bearing debris disks. Matrà et al. (2018) used the ALMA interferometer and the Submillimeter Array (SMA) to search for several molecules (including CN, HCN, and HCO<sup>+</sup>) toward  $\beta$  Pic, the nearest known gaseous debris disk. Kral et al. (2020) targeted HD 121191 and HD 129590 with the ALMA interferometer to look for CN molecules. Finally, recently Klusmeyer et al. (2021) presented a deep molecular survey of the debris disk around 49 Cet. They have targeted five molecules (HCN, CN, HCO<sup>+</sup>, SiO, and CH<sub>3</sub>OH) with ALMA to characterise the molecular chemistry. These millimeter surveys resulted in non-detections for all species. The favourable edge-on or nearly edge-on orientation of disks around  $\beta$  Pic and 49 Cet allows to probe the gas material by measuring absorption lines in their optical/ultraviolet spectra (Hobbs et al. 1985; Roberge et al. 2014). Though, the application of this technique for  $\beta$  Pic resulted in the detection of many different atomic species, even in these studies, only CO was the only detected molecule (e.g. Vidal-Madjar et al. 1994; Roberge et al. 2000, 2006). Moreover, the explored material is more related to regions located much closer to the star.

The four objects mentioned above can be classified as low or medium CO mass systems in the known sample of gas-bearing debris disks.  $\beta$  Pic and HD 129590 with their CO masses of  $M_{\text{CO}} \lesssim 10^{-4} M_{\oplus}$  probably have pure secondary origin (Cataldi et al. 2018; Matrà et al. 2018; Kral et al. 2020). HD 121191 and 49 Cet are more CO-rich, raising the possibility that their gas material may be primordial (Hughes et al. 2008; Moór et al. 2017, 2019). Nevertheless, based on their estimated CO masses,  $\sim 0.0025 M_{\oplus}$  for HD 121191 (Moór et al. 2017; Kral et al. 2020) and  $\sim 0.01 M_{\oplus}$  for 49 Cet (Moór et al. 2019), even these systems are not the most CO-rich debris disks.

Our present study focuses on the molecular inventory of four other CO-rich debris disks: HD 21997, HD 121617, HD 131488, and HD 131835 (Kóspál et al. 2013; Moór

et al. 2017). The estimated CO content of these disks is higher ( $0.02\text{--}0.1 M_{\oplus}$ ) than those discussed in the previous paragraph, making the hybrid scenario attractive in the case of these CO-rich disks. Using deep ALMA observations, we search for five molecules (CN, HCN,  $\text{HCO}^+$ ,  $\text{C}_2\text{H}$ , and CS) in these debris disks, compare the gas composition with that seen in primordial disks around mature Herbig Ae stars, and perform chemical simulations to learn if the observed gas composition could be consistent with the hybrid disk hypothesis.

We discuss the target selection process in Section 3.2. Then, we describe the observations and data reduction in Section 3.3. The results of the observations and the measured line fluxes and their upper limits are presented in Section 3.4. In Section 3.5 we are aiming to interpret the data and provide the details of our modelling strategy. The final conclusions are drawn in Section 3.6.

## 3.2 Targets and selected molecules

Observations of rare CO isotopologs ( $C^{18}O$  and  $^{13}CO$ ) implied CO gas masses of  $>0.01 M_{\oplus}$  in six gas-bearing debris disks so far. Out of these systems, 49 Cet was already surveyed for several molecules by ALMA (Kluskemper et al. 2021), while for HD 32297, no CO isotopolog data were available at the time when our target list was compiled. Therefore, the remaining four CO-rich debris disks, HD 21997, HD 121617, HD 131488, and HD 131835 were selected as targets of this study. All these disks are hosted by young A-type stars. HD 121617, HD 131488, and HD 131835 are members of the  $\sim 16$  Myr old (Pecaut & Mamajek 2016) Upper Centaurus Lupus subgroup of the Scorpius-Centaurus (Sco-Cen) association, while HD 21997 belongs to the somewhat older ( $\sim 42$  Myr, Bell et al. 2015) Columba association.

To place into context the line strengths measured in our survey we constructed a reference sample of primordial disks. Previous studies focusing on molecular composition of protoplanetary disk material mostly targeted disks around young low-mass stars (e.g., Öberg et al. 2010; Oberg et al. 2011; Guilloteau et al. 2016). Although some systems with Herbig Ae hosts have also been included in these studies, these targets were selected from the most massive, most gas-rich objects. For comparison with our debris disk sample, therefore we observed the same molecules in four nearby ( $<160$  pc), older, less gas-rich primordial disks around Herbig Ae stars, HD100453, HD139614, HD142666, and HD145718. These four objects also belong to different subgroups of the Sco-Cen association. Based on their ages (8 – 10 Myr, Table 3.1) these disks represent a late phase of the protoplanetary disk evolution and thus are deemed as direct predecessors of the younger CO-rich debris disks.

Moreover, our sample includes HD 141569, a disk around a  $\sim 6$  Myr old Herbig Ae star. Although this system is likely younger than any other in our sample (including the four protoplanetary disks) and the star exhibits signs of accretion, the dust and CO gas content of the disk resembles more that of CO-rich debris disks (Moór et al. 2019; Di Folco et al. 2020). As an explanation of the observed characteristics, a recent study of the system suggests that while the inner disk is rather protoplanetary alike, the outer disk region (our measurements mainly probe that) is more evolved and might act like a debris disk (Di Folco et al. 2020). This object, thus, likely represents an intermediate stage between the protoplanetary and debris disk phases (e.g., Hughes et al. 2018). The availability of good quality  $^{13}CO$  and/or  $C^{18}O$  measurements in the literature or the ALMA archive was another relevant consideration in their selection. The fundamental properties of the selected nine systems are summarised in Table 3.1.

In order to test the compositional similarities of CO-rich debris disks and protoplanetary disks, we selected a list of molecules for our study. We target five molecules, HCN, CN,  $HCO^+$ ,  $C_2H$ , and CS, which are routinely observed in protoplanetary disks, and whose line emission is typically only slightly weaker than that of  $^{13}CO$  (e.g., Öberg et al. 2010; Guilloteau et al. 2013, 2016; Bergner et al. 2019; Miotello et al. 2019). The same molecules could also be used to test the similarity of the composition to solar systems' comets. In addition to the three most abundant components,  $H_2O$ , CO, and  $CO_2$ , spectroscopic observations of cometary comas revealed two dozen other molecules (Bockelée-Morvan & Biver 2017). HCN is a commonly detected component whose relative abundance to water (the dominant cometary volatile) ranges between 0.08 and 0.25% in the observed comets. CN molecules are also detectable in comets. However, contrary to HCN, they are not primary volatiles released from the nucleus but instead form in the coma e.g. via photodissociation of HCN (Mumma & Charnley 2011). Due to its long photodissociation lifetime, which is barely behind that of CO molecules, CN is considered to

Table 3.1: Overview of the sample. Distance estimates are taken from Bailer-Jones et al. (2021). Group membership information is taken from the literature (Bell et al. 2015; de Zeeuw et al. 1999; Hoogerwerf 2000), abbreviations in this column are as follows – COL: Columba moving group; LCC: Lower Centaurus Crux association; UCL: Upper Centaurus Lupus association; US: Upper Scorpius association. For debris systems we quote the age of the group to which the given object belongs, while for Herbig Ae objects individual age estimates are listed from Murphy et al. (2021) and Wichittanakom et al. (2020). Fractional luminosities ( $L_{\text{disk}}/L_*$ ) of the debris discs are taken from Moór et al. (2017), while similar data of the protoplanetary sample are from Dent et al. (2005) and Meeus et al. (2012). The listed  $^{13}\text{CO}$  ( $L_{^{13}\text{CO}}$ ) and  $\text{C}^{18}\text{O}$  luminosities ( $L_{\text{C}^{18}\text{O}}$ ) refer to the J=2–1 rotational transition, except for HD 131835 (marked by asterisk) where the J=3–2 data are quoted. For HD 139614, HD 142666, and HD 145718 the CO luminosity data are derived from analysis of archival ALMA line observations obtained in the framework of ALMA project 2015.1.01600.S (PI: O. Panic). For the rest of the sample, including both the remaining Herbig stars and the debris discs, the luminosity values are computed based on CO line fluxes, obtained by the ALMA or NOEMA arrays and taken from the literature (Di Folco et al. 2020; Kóspál et al. 2013; Moór et al. 2017; van der Plas et al. 2019, Moór et al. in prep.) References used in the last column: (1): Bailer-Jones et al. (2021); (2): Bell et al. (2015); (3): Dent et al. (2005); (4): de Zeeuw et al. (1999); (5): Di Folco et al. (2020); (6): Hoogerwerf (2000); (7): Kóspál et al. (2013); (8): Meeus et al. (2012); (9): Moór et al. (2017); (10): Moór et al. in prep. (11): Murphy et al. (2021); (12): Pecaut & Mamajek (2016); (13): van der Plas et al. (2019); (14): Wichittanakom et al. (2020).

Target name	Spectral Type	Distance (pc)	Group	$T_{\text{eff}}$ (K)	$L_*$ ( $L_{\odot}$ )	$M_*$ ( $M_{\odot}$ )	Age (Myr)	$L_{\text{disk}}/L_*$	$L_{^{13}\text{CO}}$ ( $10^{17}\text{W}$ )	$L_{\text{C}^{18}\text{O}}$ ( $10^{17}\text{W}$ )	Ref.
HD 21997	A3V	$69.6 \pm 0.1$	COL	8300	10.4	1.75	42	$5.7 \times 10^{-4}$	3.5	1.5	1,2,7,9
HD 121617	A1V	$117.5 \pm 0.5$	UCL	9050	14.9	1.92	16	$4.8 \times 10^{-3}$	6.4	1.0	1,6,9,12
HD 131488	A1V	$151.4^{+0.6}_{-0.8}$	UCL	9000	13.5	1.88	16	$5.5 \times 10^{-3}$	9.8	5.3	1,6,9,12
HD 131835	A2V	$129.1^{+0.5}_{-0.4}$	UCL	8400	10.3	1.75	16	$3.0 \times 10^{-3}$	11.5*	5.8*	1,4,9,10,12
HD 141569	B9.5V/A0Ve	$111.3^{+0.3}_{-0.4}$	-	9500	21.9	2.06	5.9	$9.0 \times 10^{-3}$	13.0	<1.1	1,5,8,14
HD 100453	A9Ve	$103.7 \pm 0.2$	LCC	7250	7.1	1.48	11.0	$6.2 \times 10^{-1}$	8.5	3.7	1,4,8,13,14
HD 139614	A7Ve	$133.1^{+0.5}_{-0.4}$	UCL	7650	6.7	1.52	10.8	$3.9 \times 10^{-1}$	41.4	16.4	1,6,8,11
HD 142666	A8Ve	$145.5 \pm 0.4$	US	7250	12.0	1.64	7.8	$3.3 \times 10^{-1}$	23.9	9.8	1,6,8,14
HD 145718	A5Ve	$153.9^{+0.5}_{-0.4}$	US	7750	11.2	1.64	8.7	$1.0 \times 10^{-1}$	29.1	15.5	1,3,6,14

be the most promising molecule for detection in secondary gas material after CO (Matrà et al. 2018).  $C_2H$  is also not a primary volatile, but can be produced via the photodissociation of  $C_2H_2$ , a molecule already detected in several comets (Bockelée-Morvan & Biver 2017). The detection of  $HCO^+$  is less common, mostly limited to one Solar system comet, the Hale-Bopp (Veal et al. 1997), where it is suggested to be formed via chemical reactions in the coma (Lovell et al. 1997; Milam et al. 2004).

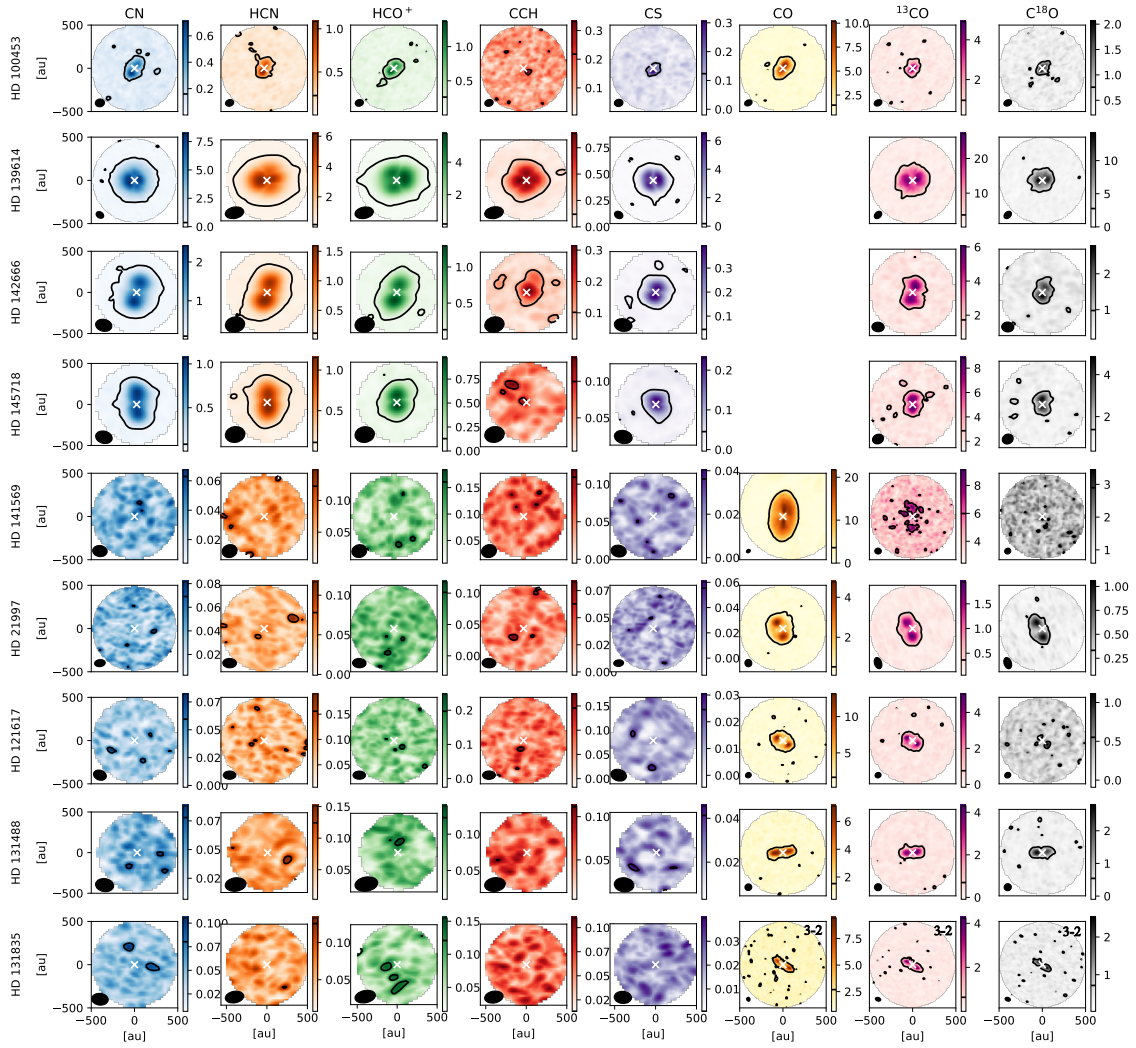


Figure 3.1: Peak brightness temperature for the observed disks. Contours show  $3\sigma$  noise level.  $\text{HCO}^+$ , HCN, CN, and  $\text{C}_2\text{H}$  were observed within the project, and CO isotopologs represent archival ALMA data. Data for HD 141569  $^{12}\text{CO}$  are taken from Di Folco et al. (2020). HD 131835 is shown in CO isotopologs J=3-2 transitions, HD 141569 is in  $^{12}\text{CO}$  J=3-2, the others are in CO isotopologs J=2-1. The color bar units are K.

### 3.3 Observations and data reduction

Observations of our targets were performed with the ALMA 12m Array during 2018 and 2019 in the framework of two projects (2017.1.01545.S and 2018.1.01429.S, PI: Th. Henning). The main parameters of these observations – including their dates, the number of antennas, the baseline ranges of the array configurations, as well as the applied flux, bandpass, and phase calibrators – are listed in Table 3.2. HD 131488 and HD 131835 as well as HD 142666 and HD 145718 are situated close to each other in the sky, allowing us to observe these pairs together in the same scheduling blocks.

Considering the typical low gas temperatures (Kóspál et al. 2013; Hughes et al. 2017) and the possible low density of potential collisional partners in CO-bearing debris disks, which can result in low excitation temperatures, we observed the lower transitions for the selected molecules. To observe the targeted lines, we defined one spectral setup in Band 5 and one in Band 6 for each object. Hyperfine transitions of the  $\text{C}_2\text{H}$  N=2–1 line, as well as the J=2–1 lines of  $\text{HCO}^+$  and HCN, were measured simultaneously in Band 5 using three spectral windows, each with a spectral resolution of 488.28 kHz ( $\sim 0.83 \text{ km s}^{-1}$ ). This

Table 3.2: Observational parameters

Target name	Project code	Obs. date	Antennas #	Baselines (m)	Band	Calibrators		Int. time (m)	
						Flux	Bandpass		
HD 21997	2018.1.01429.S	2019-03-20	44	15-314	5	J0423-0120	J0423-0120	J0329-2357	34
HD 21997	2018.1.01429.S	2019-03-11	44	15-314	6	J0423-0120	J0423-0120	J0329-2357	31
HD 100453	2018.1.01429.S	2018-12-06	45	15-784	5	J1107-4449	J1107-4449	J1132-5606	27
HD 100453	2018.1.01429.S	2018-12-19	45	15-500	6	J1107-4449	J1107-4449	J1132-5606	24
HD 121617	2017.1.01545.S	2018-05-28	43	15-457	5	J1427-4206	J1427-4206	J1321-4342	47
HD 121617	2017.1.01545.S	2018-08-18	45	15-314	6	J1427-4206	J1427-4206	J1424-4913	42
HD 131488	2017.1.01545.S	2018-07-09	44	15-314	5	J1517-2422	J1517-2422	J1457-3539	35
HD 131835	2017.1.01545.S	2018-07-09	44	15-314	5	J1517-2422	J1517-2422	J1457-3539	35
HD 131488	2017.1.01545.S	2018-07-16	43	15-314	6	J1427-4206	J1427-4206	J1457-3539	32
HD 131835	2017.1.01545.S	2018-07-16	43	15-314	6	J1427-4206	J1427-4206	J1457-3539	31
HD 139614	2017.1.01545.S	2018-08-24	45	15-500	5	J1617-5848	J1617-5848	J1555-4150	25
HD 139614	2017.1.01545.S	2018-04-01	44	15-704	6	J1427-4206	J1427-4206	J1604-4441	22
HD 141569	2017.1.01545.S	2018-08-24	43	15-314	5	J1550+0527	J1550+0527	J1557-0001	25
HD 141569	2017.1.01545.S	2018-04-01	42	15-284	6	J1517-2422	J1517-2422	J1557-0001	22
HD 142666	2017.1.01545.S	2018-07-04	44	15-314	5	J1517-2422	J1517-2422	J1551-1755	24
HD 145718	2017.1.01545.S	2018-07-04	44	15-314	5	J1517-2422	J1517-2422	J1551-1755	24
HD 142666	2017.1.01545.S	2018-05-30	43	15-314	6	J1517-2422	J1517-2422	J1551-1755	22
HD 145718	2017.1.01545.S	2018-05-30	43	15-314	6	J1517-2422	J1517-2422	J1551-1755	22

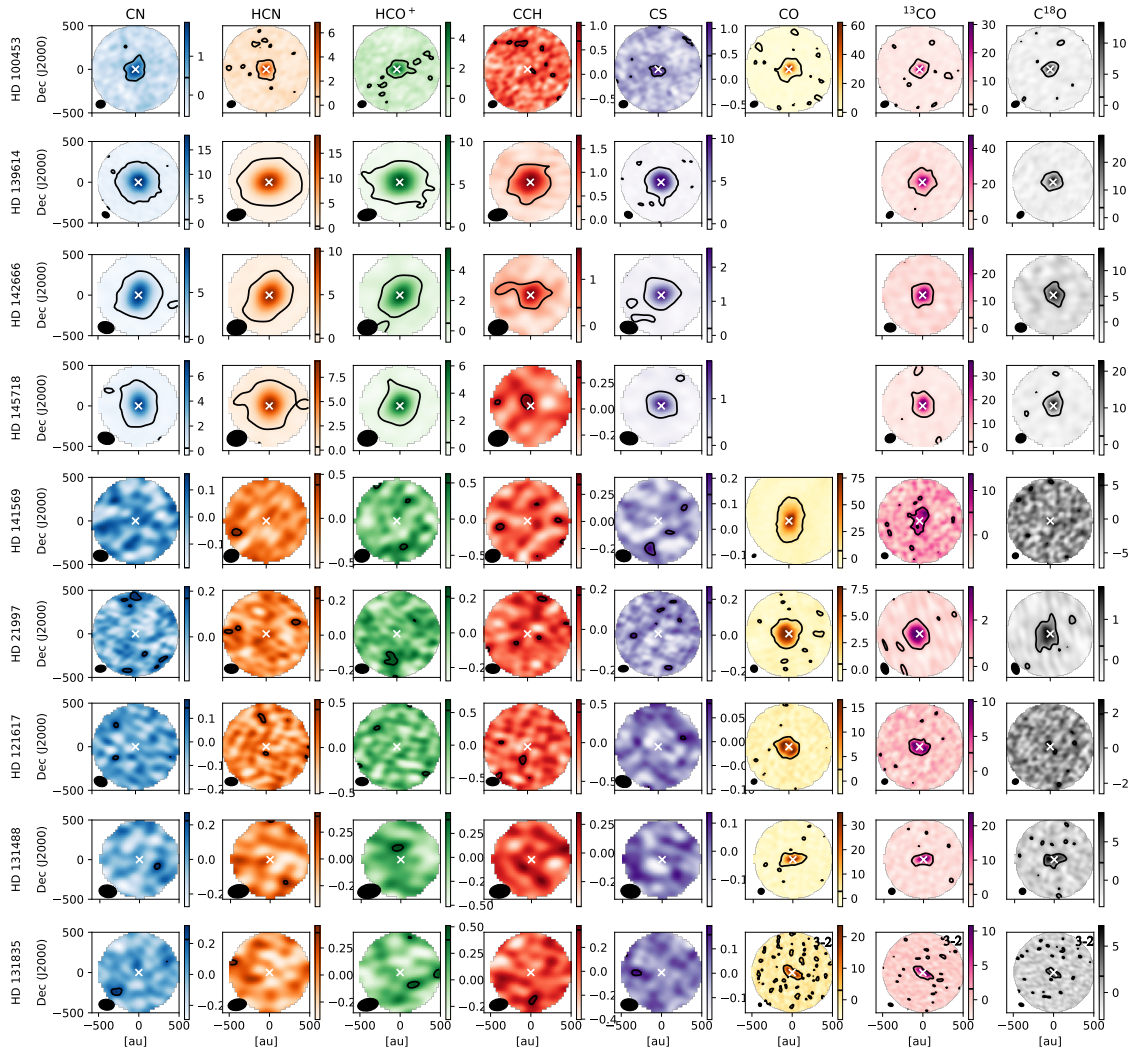


Figure 3.2: Moment zero maps for the observed disks. HD 131835 is shown in CO isotopologs J=3-2 transitions, the other are in CO isotopologs J=2-1. The velocity range was selected based on CO emission data cubes. The colorbar units are K km / s. Data for HD 141569  $^{12}\text{CO}$  are taken from Di Folco et al. (2020).

Table 3.3: List of the transitions used in our analysis. Note that in the case of C<sub>2</sub>H and CN our observations covered more transitions but those were not utilized in our work. Rest frequencies are taken from the Splatalogue database (<https://www.cv.nrao.edu/php/splat/>).

Molecule	Transition	Rest frequency (GHz)
C <sub>2</sub> H	$N = 2 - 1, J = \frac{5}{2} - \frac{3}{2}, F = 3 - 2$	174.6632220
	$N = 2 - 1, J = \frac{3}{2} - \frac{1}{2}, F = 2 - 1$	174.6676850
HCN	$J = 2 - 1$	177.2611115
HCO <sup>+</sup>	$J = 2 - 1$	178.3750563
CN	$N = 2 - 1, J = \frac{5}{2} - \frac{3}{2}, F = \frac{5}{2} - \frac{3}{2}$	226.8741908
	$N = 2 - 1, J = \frac{5}{2} - \frac{3}{2}, F = \frac{7}{2} - \frac{5}{2}$	226.8747813
	$N = 2 - 1, J = \frac{3}{2} - \frac{1}{2}, F = \frac{3}{2} - \frac{1}{2}$	226.8758960
CS	$J = 5 - 4$	244.9355565

resulted in a total bandwidth of 937.5 MHz (over 1920 channels) in the spectral window, which targeted the C<sub>2</sub>H line. Centred at 174.96 GHz, this window covered the hyperfine lines of C<sub>2</sub>H. The other two spectral windows at 177.27 and 178.2 GHz have a total bandwidth of 468.75 MHz (over 960 channels) each. Two additional spectral windows with a bandwidth of 1.875 GHz (128 channels), centred at 187.5 and 189.4 GHz were used to measure the Band 5 continuum. In Band 6 the correlator was set up with four spectral windows. Hyperfine transitions of CN N=2–1 were observed with a spectral resolution of 488.28 kHz ( $\sim 0.65 \text{ km s}^{-1}$ ) in a window centred at 226.65 GHz. With the 1920 available channels, this provides a total bandwidth of 937.5 MHz. Exploiting the capabilities of ALMA, in addition to the primarily targeted molecules, we also searched for additional molecular lines using the coarsest spectral resolution (976.56 kHz,  $\sim 1.2 \text{ km s}^{-1}$ ) in two basebands centred at 242.1 and 244.68 GHz. The fourth window, focused on measuring the dust continuum, has a central frequency of 229.00 GHz and provides a bandwidth of 1.875 GHz. The integration time ranged from 22 to 47 minutes per source, see Table 3.2. The frequencies of the transitions we used in our analysis are summarized in Table 3.3.

Calibration and flagging of the raw data sets were performed in the Common Astronomy Software Applications (CASA, version 5.1.1, McMullin et al. 2007) using the standard ALMA reduction scripts. Prior to line imaging, we subtracted continuum emission from the obtained visibilities using the UVCONTSUB task of CASA. We fitted first-order polynomials to the line-free channels in the  $uv$  space. Using the continuum-subtracted data, we applied the TCLEAN task to construct spectral cubes of line observations. Natural weighting was adopted. The channel width was rebinned to  $0.9 \text{ km s}^{-1}$  for C<sub>2</sub>H, HCO<sup>+</sup> and HCN lines and to  $0.75 \text{ km s}^{-1}$  for CN observations, respectively. In the coarse-resolution Band 6 measurements, a channel width of  $1.25 \text{ km s}^{-1}$  was used. While the remaining part of this chapter focuses on the analysis of the molecular line results, for completeness in Appendix 3.7 we briefly summarise the processing and analysis of the continuum data.

### 3.4 Results and analysis

By inspecting the obtained data cubes, we found significant CN, HCN, and HCO<sup>+</sup> emission towards all four targeted H Ae protoplanetary disks (HD 100453, HD 139614, HD 142666, and HD 145718), while the C<sub>2</sub>H line was detected only in HD 139614 and HD 142666 (Figs. 3.1, 3.3). The J=5 – 4 transition of the CS molecule (Band 6, 244.9355565 GHz) was also detected in one of the additional coarse-resolution spectral windows in all four disks.

In the detected cases, zeroth moment maps were constructed by integrating over the velocity ranges of the significant line emission. The selected ranges are in good agreement with those inferred from the CO measurements of the same disks. The integrated line fluxes were derived by using elliptical apertures that were fitted to the observed velocity-integrated emission. To estimate flux uncertainties, we randomly distributed 16 identical elliptical apertures in the background region and computed the standard deviation of the fluxes obtained in them.

In the case of CN and C<sub>2</sub>H, the spectral ranges cover several hyperfine transitions. For CN, the integrated maps, and thus the derived fluxes, are related to the  $N = 2 - 1$ ,  $J = \frac{5}{2} - \frac{3}{2}$  transition, which consists of three blended hyperfine transitions ( $F = \frac{7}{2} - \frac{5}{2}$ ,  $\frac{5}{2} - \frac{3}{2}$ , and  $\frac{3}{2} - \frac{1}{2}$ ), while for C<sub>2</sub>H the line fluxes are the sum of two hyperfine transitions ( $F = 3 - 2$  and  $2 - 1$ ) of the  $N = 2 - 1$ ,  $J = \frac{5}{2} - \frac{3}{2}$  line. No C<sub>2</sub>H emission was detected toward HD 100453 and HD 145718. In these cases, we computed upper limits for the integrated line flux. To this end, we determined the velocity range of the expected line by using the HCN measurement of the given object as a template. We selected HCN because, on average, this line is the brightest among those detected for the given systems in our project. In determining the relevant velocity range, we also considered that the C<sub>2</sub>H is composed of two hyperfine transitions. Then we created zeroth moment maps. Finally, using the same elliptical aperture as in the corresponding HCN observations, we computed the  $3\sigma$  upper limits.

None of the four CO-rich debris disks, nor the disk around HD 141569 exhibited detectable line emission in any data cubes. For the calculation of the upper limits, we used the method described above, with the difference that we utilised the <sup>12</sup>CO measurements of the given sources as a template. The CO measurements were taken from the ALMA archive and the template data cubes were smoothed using the `IMSMOOTH` CASA task to obtain the same synthesised beam as that of the given line. We used the same channel width for these templates for the line measurements where upper limits are to be determined. Thus, we used 0.9 km s<sup>-1</sup> for the C<sub>2</sub>H, HCO<sup>+</sup>, and HCN measurements and 0.75 km s<sup>-1</sup> for the CN observations. For the CN and C<sub>2</sub>H data, we considered the hyperfine structure, which is resulted in broader velocity ranges to be used in the analysis. In the case of HD 21997, ~50% of the channels covering the HCO<sup>+</sup> line were flagged during the calibration process not to be used for scientific analysis. Therefore, this upper limit estimate was obtained by slightly shifting the velocity range to a non-flagged part of the spectrum. The measured integrated line fluxes are summarised in Table 3.5.

We present the resulting peak brightness maps in Fig. 3.1. The first five rows are disks around Herbig Ae stars (HD 100453, HD 139614, HD 142666, HD 145718), followed by the more evolved disk HD 141569. The latter four rows show debris disks data (HD 21997, HD 121617, HD 131488, HD 131835). We also present moment zero maps in the Appendix (3.2).

Figure 3.4 shows the measured CN, HCN, HCO<sup>+</sup>, C<sub>2</sub>H, and CS line flux ratios with respect to the <sup>13</sup>CO (2–1) (left panel) and C<sup>18</sup>O (2–1) (right panel) lines for our targets. Since for HD 141569 only an upper limit is available for the C<sup>18</sup>O line flux, it is not

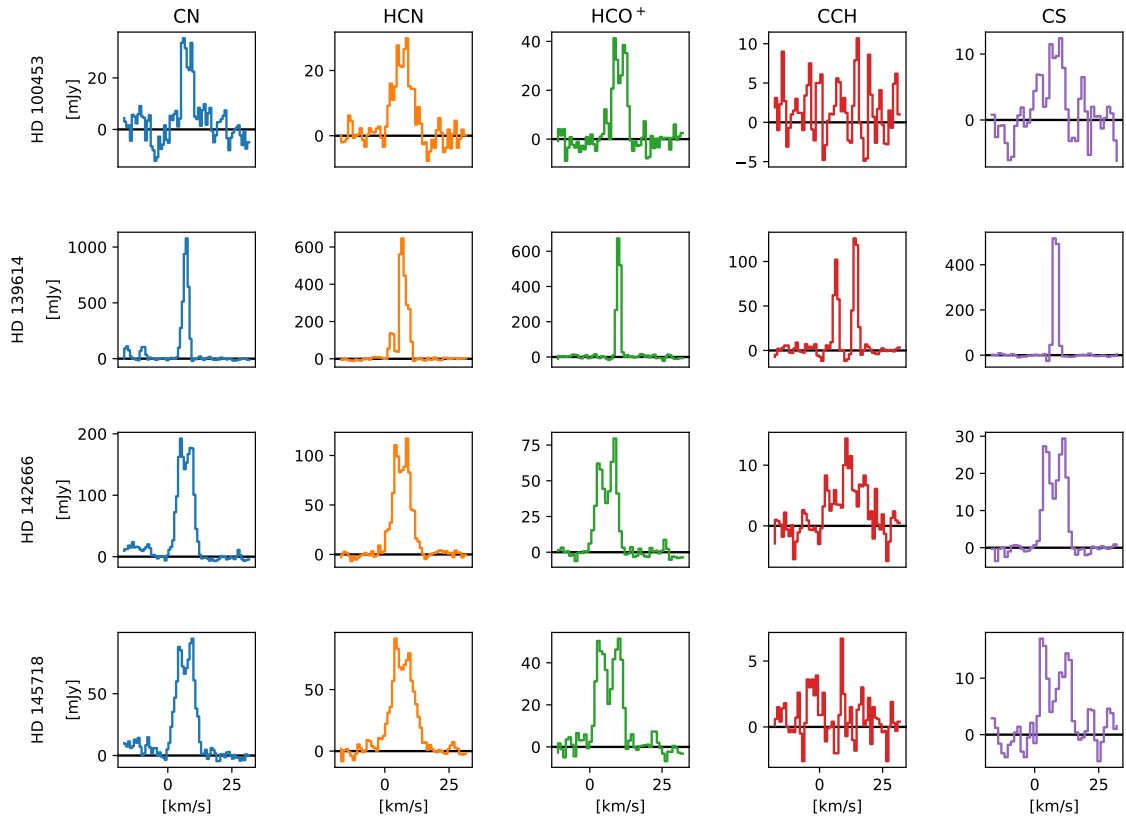


Figure 3.3: CN, HCN, HCO<sup>+</sup>, C<sub>2</sub>H, and CS emission line profiles of the observed Herbig disks.

shown in the corresponding panel. Apart from the case of C<sub>2</sub>H measurements, the four protoplanetary disks are clearly separated from the debris disks and from HD 141569 in these plots. This is especially striking for the CN, HCN, and HCO<sup>+</sup> lines, even for HD 100453 – that exhibits the lowest line ratios – the obtained ratios are at least 4× higher than the corresponding average upper limits of the debris disk sample. These results suggest that molecular abundances or physical conditions of the gas in the CO-rich debris disks is very different from those in the protoplanetary disks around Herbig Ae stars. We also find that HD 141569 more resembles debris disks than our protoplanetary disk sample, similar to the previous results based on its dust and CO content (see Sect. 3.2).

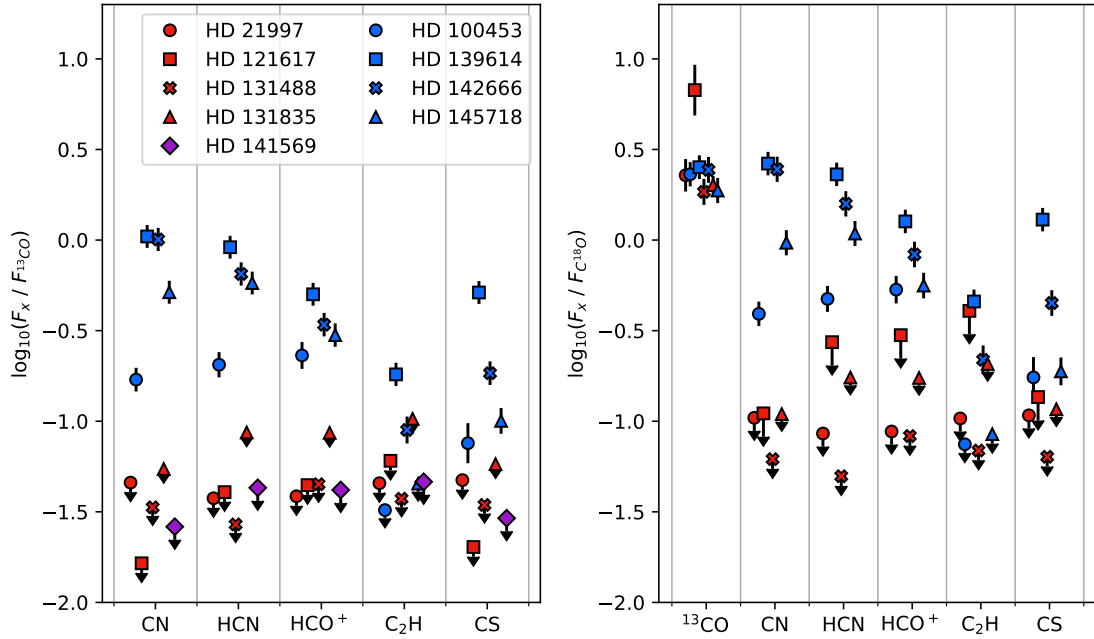


Figure 3.4: Line flux ratios of CN, HCN, HCO<sup>+</sup>, C<sub>2</sub>H, and CS molecules with respect to the <sup>13</sup>CO 2–1 (left) and C<sup>18</sup>O 2–1 (right) lines. The CN, HCN, HCO<sup>+</sup>, C<sub>2</sub>H, and CS line fluxes are from Table 3.5. The <sup>13</sup>CO and C<sup>18</sup>O data of HD 121617, HD 131488, and HD 21997 are from Moór et al. (2017) and Kóspál et al. (2013). For HD 131835, only the 3–2 rotational transition of <sup>13</sup>CO and C<sup>18</sup>O has been measured (Moór et al., in prep.) from which we estimated the 2–1 line fluxes. In the case of optically thick <sup>13</sup>CO, the obtained 3–2 line flux was scaled by  $(\nu_{3-2}/\nu_{2-1})^2 = 2.25$ , while for the optically thin C<sup>18</sup>O emission we assumed that local thermodynamical equilibrium holds and that the gas temperature is 20 K, resulting in a 3–2 to 2–1 line flux ratio of 2.3. As for the younger targets, CO flux data of HD 100453 and HD 141569 are taken from van der Plas et al. (2019) and Di Folco et al. (2020), respectively. For the remaining three objects, HD 139614, HD 142666, and HD 145718, we inferred the necessary flux data from the analysis of archival ALMA line observations (all belong to the project 2015.1.01600.S, PI: O. Panic).

Table 3.4: Basic properties of CO gas component in the debris disk subsample. The listed CO mass estimates are based on analysis of optically thin C<sup>18</sup>O line observations. References in the last column: (1): Kóspál et al. (2013); (2): Kral et al. (2019); (3): Moór et al. (2017); (4): Pawellek et al. (in prep.).

Object	$R_{\text{in, gas}}$ (au)	$R_{\text{out, gas}}$ (au)	$M_{\text{CO}}$ ( $M_{\oplus}$ )	Ref.
HD 21997	< 25	133	0.06	1
HD 121617	50	100	0.02	3
HD 131488	35	140	0.10	3,4
HD 131835	50	130	0.04	2,3

## 3.5 Discussion

### 3.5.1 Photodissociation of molecules

Does the striking difference between the observed line ratios in the protoplanetary and the debris disk samples provide a clear hint that the gas in these debris disks is of secondary origin? Before examining this in more detail (Sect. 3.5.2), it is worth summarising how sensitive the studied molecules are to the UV radiation and which shielding mechanisms could protect them from photodissociation in an H<sub>2</sub>-rich hybrid versus an H<sub>2</sub>-poor secondary environment.

The photodissociation rate of a given molecule can be estimated as  $k = k_0\theta$ , where  $k_0$  is the unattenuated photodissociation rate of the molecule, while  $\theta$  is the shielding function (Heays et al. 2017). The latter function considers all other species that can shield the specific molecule against UV photons. An important difference between protoplanetary and debris disks is that optically thin dust cannot effectively attenuate the UV radiation in the debris disks.

In addition to the possible self-shielding of different molecules, in a hybrid disk dominantly H<sub>2</sub> molecules, while in secondary disks mainly C atoms can contribute substantially to the shielding (Kóspál et al. 2013; Kral et al. 2019). Figure 3.5 shows the photodissociation lifetimes ( $\tau = 1/k$ ) of the targeted molecules and CO for the various H<sub>2</sub> or neutral atomic carbon column densities. We took into account only the interstellar UV radiation field in our calculations. The unattenuated photodissociation rates, as well as the corresponding shielding functions, were taken from Heays et al. (2017).

As Fig. 3.5 clearly demonstrates, CO and HCO<sup>+</sup> molecules have quite long unattenuated photodissociation lifetimes, and could be efficiently shielded by both H<sub>2</sub> molecules and C atoms. In contrast, CN, HCN, C<sub>2</sub>H, and CS can absorb UV photons at wavelengths longward of 110 nm, outside the wavelength interval where the H<sub>2</sub> molecules and C atoms can provide effective shielding. Without shielding at these long wavelengths, the latter four molecules have only short photodissociation lifetimes both in hybrid and shielded secondary disks, while in protoplanetary environments they could still be protected from UV by the optically thick dust. The observed low line ratios of these four species to CO in the debris disk sample, therefore, do not necessarily preclude the hybrid scenario (Fig. 3.4). In the case of more shielded HCO<sup>+</sup>, the longer photodissociation timescale and higher concentrations would be expected even in the optically thin debris disks. Using a physico-chemical and radiative transfer modelling, we examine below in more detail how the observed line ratios could constrain the nature of the CO-rich debris disks.

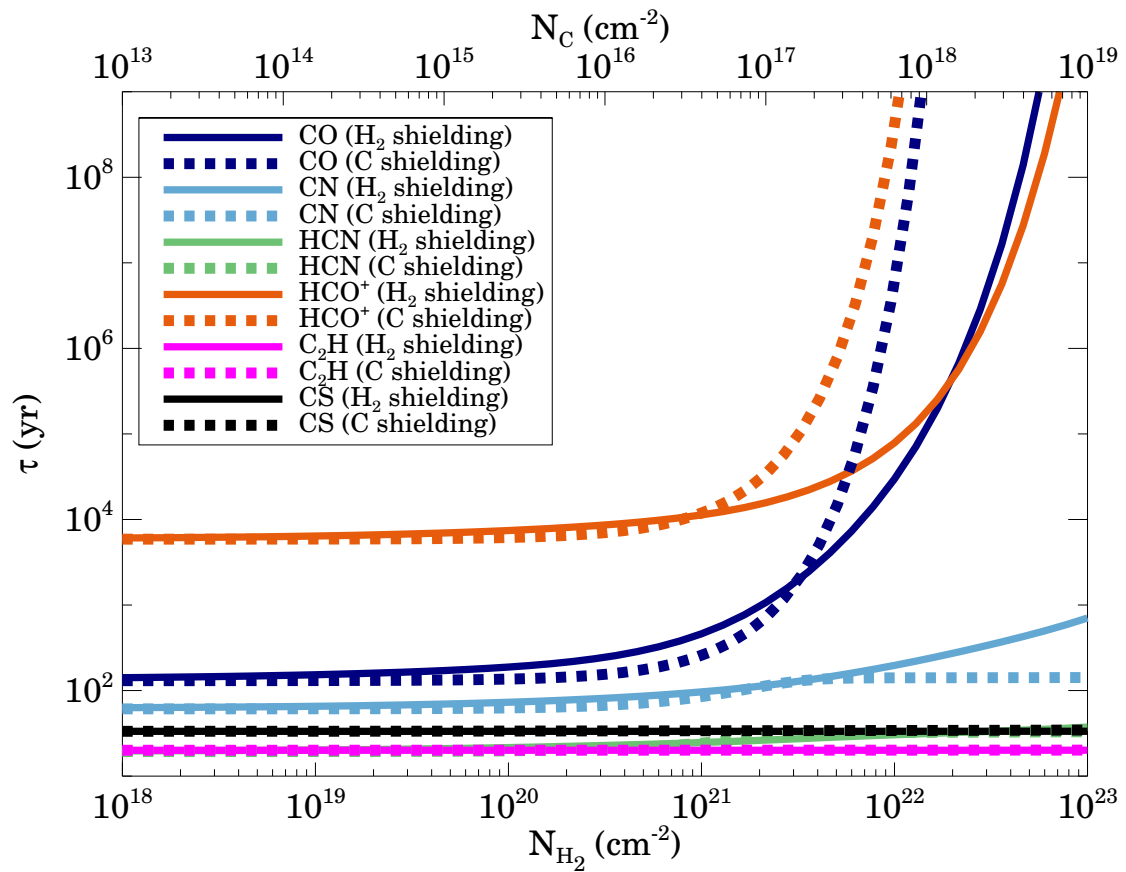


Figure 3.5: Photodissociation lifetimes of the CN, HCN, HCO<sup>+</sup>, C<sub>2</sub>H, CS, and CO molecules in the interstellar radiation field, considering possible shielding by hydrogen molecules or carbon atoms.

Table 3.5: Integrated line fluxes and  $3\sigma$  upper limits for our targets. Uncertainties in parentheses are quadratic sums of the measurement errors and the overall calibration uncertainty (assumed to be 10%).

Target name	$S_{\text{CN}}$ (mJy km s <sup>-1</sup> )	$S_{\text{HCN}}$ (mJy km s <sup>-1</sup> )	$S_{\text{HCO}^+}$ (mJy km s <sup>-1</sup> )	$S_{\text{CCH}}$ (mJy km s <sup>-1</sup> )	$S_{\text{CS}}$ (mJy km s <sup>-1</sup> )
HD 100453	153±6 (16)	185±12 (22)	208±19 (28)	<29.1	69.5±16.3 (17.7)
HD 139614	2790±47 (283)	2433±32 (245)	1338±23 (136)	484±16 (51)	1369±19 (138)
HD 142666	1296±15 (130)	836±15 (85)	439±12 (46)	115±10 (15)	237±7 (25)
HD 145718	721±19 (75)	811±14 (82)	419±16 (45)	<63.4	141±11 (18)
HD 141569	<31.4	<51.5	<50.1	<55.6	<35.0
HD 21997	<37.6	<30.8	<31.6	<37.3	<38.8
HD 121617	<8.7	<21.5	<23.5	<32.0	<10.7
HD 131488	<16.4	<13.2	<22.0	<18.3	<16.9
HD 131835	<12.7	<20.2	<20.1	<24.0	<13.5

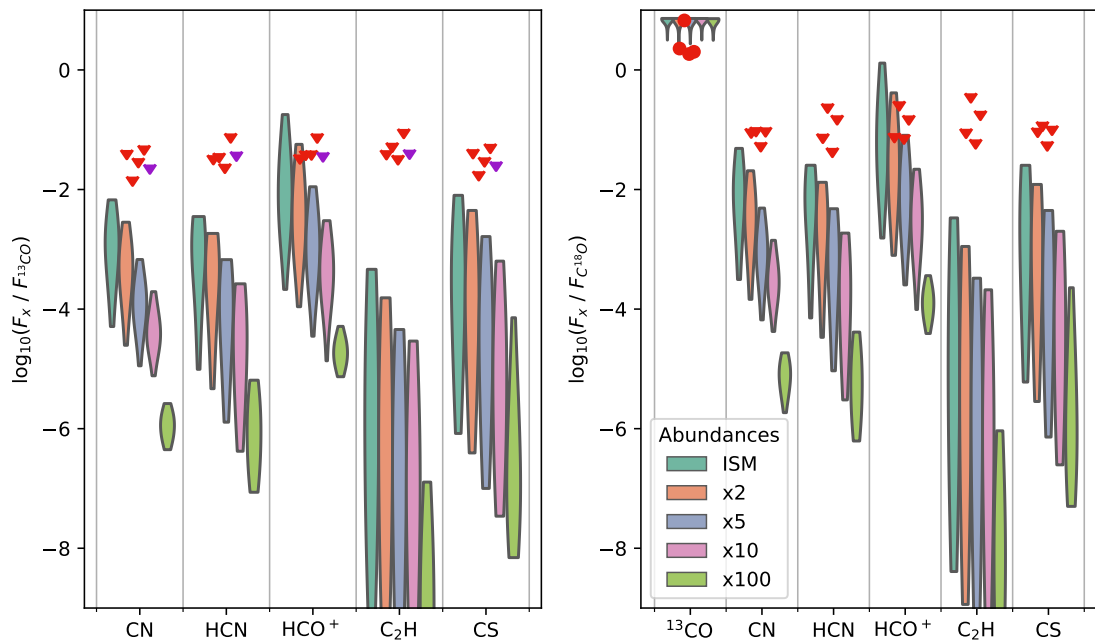


Figure 3.6: Scattered dots: observed line ratios, red for debris disks, purple for HD 141569. Circles are detections, and triangles are the upper limits. Violin bars: distributions of the modelled debris disk line ratios using primordial ISM-like and secondary hydrogen-depleted elemental ratios. Non-detection of CN, HCN, C<sub>2</sub>H, and CS in debris disks is fully reproduced. Significantly higher HCO<sup>+</sup> line fluxes are computed with the debris disk models using the H<sub>2</sub>-rich, ISM-like initial abundances as compared with the H<sub>2</sub>-poor case.

Table 3.6: Initial Chemical Abundances.

Species	Abundance (ISM-like) $n(X) / n(H)$	Abundance ( $H_2$ and He are 100× depleted) $n(X) / n(H)$
$H_2$	$5.00 \times 10^{-1}$	$5.00 \times 10^{-1}$
He	$9.75 \times 10^{-2}$	$9.75 \times 10^{-2}$
C	$7.86 \times 10^{-5}$	$7.86 \times 10^{-3}$
N	$2.47 \times 10^{-5}$	$2.47 \times 10^{-3}$
O	$1.80 \times 10^{-4}$	$1.80 \times 10^{-2}$
S	$9.14 \times 10^{-8}$	$9.14 \times 10^{-6}$
Si	$9.74 \times 10^{-8}$	$9.74 \times 10^{-6}$
Mg	$1.09 \times 10^{-8}$	$1.09 \times 10^{-6}$
Fe	$2.74 \times 10^{-9}$	$2.74 \times 10^{-7}$
Na	$2.25 \times 10^{-9}$	$2.25 \times 10^{-7}$
Cl	$1.00 \times 10^{-9}$	$1.00 \times 10^{-7}$
P	$2.16 \times 10^{-10}$	$2.16 \times 10^{-8}$

### 3.5.2 Chemical and line flux modelling

To reproduce detections of the CO isotopologs and non-detections of  $HCO^+$ , CN, HCN,  $C_2H$ , and CS in debris disks, we have utilised the ALCHEMIC chemical model (Semenov et al. 2010) and the RADEX line radiative transfer code (van der Tak et al. 2010), and adopted a temperature-density grid. Given that the observed CO emission appears as a relatively narrow ring-like structure in optically thin debris disks, we assume a rather tight variation of temperature and UV radiation strength within the gas emitting area. These physical conditions have been used to calculate time-dependent chemical evolution using the single-point ALCHEMIC chemical kinetics code and an up-to-date gas-grain chemical network (based on the KIDA'17 database with recent updates; Wakelam et al. (2012, 2015)). The model includes gas-phase reactions, X-ray and UV photodissociation and photoionisation, cosmic ray-induced processes, as well as molecular freeze-out onto dust grain surfaces, surface reactions, and thermal and non-thermal desorption of ices. This chemical model is identical to the model used in Smirnov-Pinchukov et al. (2020), with the only exception of non-inclusion of deuterium, and hence it is only briefly summarised here.

We have modelled chemical evolution over a temperature range between 10 and 300 K and densities between  $10^3$  and  $10^7$   $cm^{-3}$  (or between  $\approx 4 \times 10^{-21}$  and  $4 \times 10^{-17}$   $g\ cm^{-3}$ ). The unattenuated UV field from the star was set to be equal to the vertical ISRF (Draine & Lee 1984). The absorption of UV photons was considered in the radial direction only, in a range between  $\tau = 0$  and  $\tau = 1$ , which corresponds to the observed optical depth in debris disks, which are relatively dust-poor. Since primordial (sub-)micron-sized dust has already evolved and became severely depleted, we decided to set the corresponding dust-to-gas mass ratio to a value of  $10^{-10}$  for 0.1  $\mu m$ -sized grains, effectively turning off dust-surface reactions. The ionisation rate was set to  $1.3 \times 10^{-17}$   $s^{-1}$ , corresponding to a galactic cosmic ray ionisation rate. High-energetic particle flux and X-ray radiation from the evolved main-sequence star were neglected, as these are much milder compared to the pre-main-sequence phase. Non-inclusion of X-ray and high energy particle radiation from the star does not affect the conclusions, as the higher intensity of ionising radiation in the model increases  $HCO^+$ , thus increasing the area in the parameter space forbidden by the observational data.

We have considered five sets of initial abundances. The first so-called “low metals”

set of mainly atomic abundances from Lee et al. (1998) describes the elemental content of the ISM that is available for gas or icy chemistry. It is often used to model protoplanetary disks, assuming a full chemical “reset” scenario (Eistrup et al. 2016; Drozdovskaya et al. 2016; Smirnov-Pinchukov et al. 2020). In the other four sets, we multiplied the relative abundances of all species other than hydrogen and helium by a factor of 2, 5, 10, and 100, respectively. These four cases represent a scenario when a debris disk gas is partly replenished by secondary, collisionally-generated H<sub>2</sub>-poor gas. Using the above chemical model, we have calculated the abundance evolution over 1 Myr for constant physical conditions. This timespan was long enough to reach a chemical equilibrium within 1–100 kyr for the observed, chemically simple molecules (depending on density). The final molecular concentrations have been used for the line radiative transfer simulations.

We have calculated the line brightness temperatures with the non-LTE RADEX code. The collisional cross-section and other spectroscopic data from the Leiden Atomic and Molecular Database (LAMDA) have been utilised (Schöier et al. 2005). Since <sup>13</sup>C and <sup>18</sup>O are not included in the chemical network, we have used fixed isotopic ratios  $C^{12}/C^{13} = 77$  and  $O^{16}/O^{18} = 560$  to scale down the resulting molecular abundances (Wilson & Rood 1994). We have calculated the line brightness temperatures assuming the length of the emitting gas column of 15 au and a line full width at half maximum (FWHM) of 1 km s<sup>-1</sup>. The collision partner densities have been taken from the chemical simulations. We have calculated the CN brightness temperature using hyperfine components from (Flower & Lique 2015).

The results of the debris disk line simulations are presented in Fig. 3.6. Using violin bars, we show the smoothed distribution of the simulated line ratios for the modelled disk cells. We also overplot this figure with the observed line ratios and their upper limits, similar to Fig. 3.4. As it can be clearly seen from Fig. 3.6, all line intensities other than HCO<sup>+</sup> are expected to be below the detection limits, regardless of the initial abundances and position in the temperature-density parameter space. In the H<sub>2</sub>-poor cases, the modelled CN, HCN, HCO<sup>+</sup>, C<sub>2</sub>H, and CS line intensities relative to the CO emission are predicted to decrease monotonically with the hydrogen depletion factor for the same range of the CO densities.

We present the constraints on the parameter space for a single-point debris disk model in Fig. 3.7. We select a temperature range between 20 and 70 K and the CO volume density between 1 and 10<sup>4</sup> cm<sup>-3</sup>. Our upper boundary to the debris disk gas density is calculated by dividing the measured <sup>13</sup>CO and C<sup>18</sup>O masses by the fitted area and the scale heights of the corresponding CO emitting rings estimated from the modelling (Table 3.4). Disk midplane densities are shown in Fig. 3.7 as black lines. With red contours, we show the regions in the parameter space, for which the predicted HCO<sup>+</sup> J=2-1/<sup>13</sup>CO J=2-1 flux ratio is higher than the detection limit.

The selected parameter space partially yields higher HCO<sup>+</sup> intensities than the upper limit set by our observations. That leaves a possibility that deeper observations could allow detecting HCO<sup>+</sup> in debris disks if their gas retains ISM-like composition and is H<sub>2</sub>-rich. In such disks, the HCO<sup>+</sup> J=2-1 line would become detectable if the gas is warmer than 20 K and the CO density is about 3 – 300 cm<sup>-3</sup>. If a debris disk possesses an extended tenuous atmosphere, the HCO<sup>+</sup> emission from this region also contributes to the total HCO<sup>+</sup> line flux and hence increase the resulting HCO<sup>+</sup>/CO line ratio. With the currently available data, we estimate that the contribution of the debris disk atmosphere to the total HCO<sup>+</sup> line flux is negligible even in the H<sub>2</sub>-rich ISM case. Follow-up higher-resolution CO or more sensitive HCO<sup>+</sup> observations combined with feasible thermochemical modelling are required to provide tighter constraints on the CO/H<sub>2</sub> ratios in these disks.

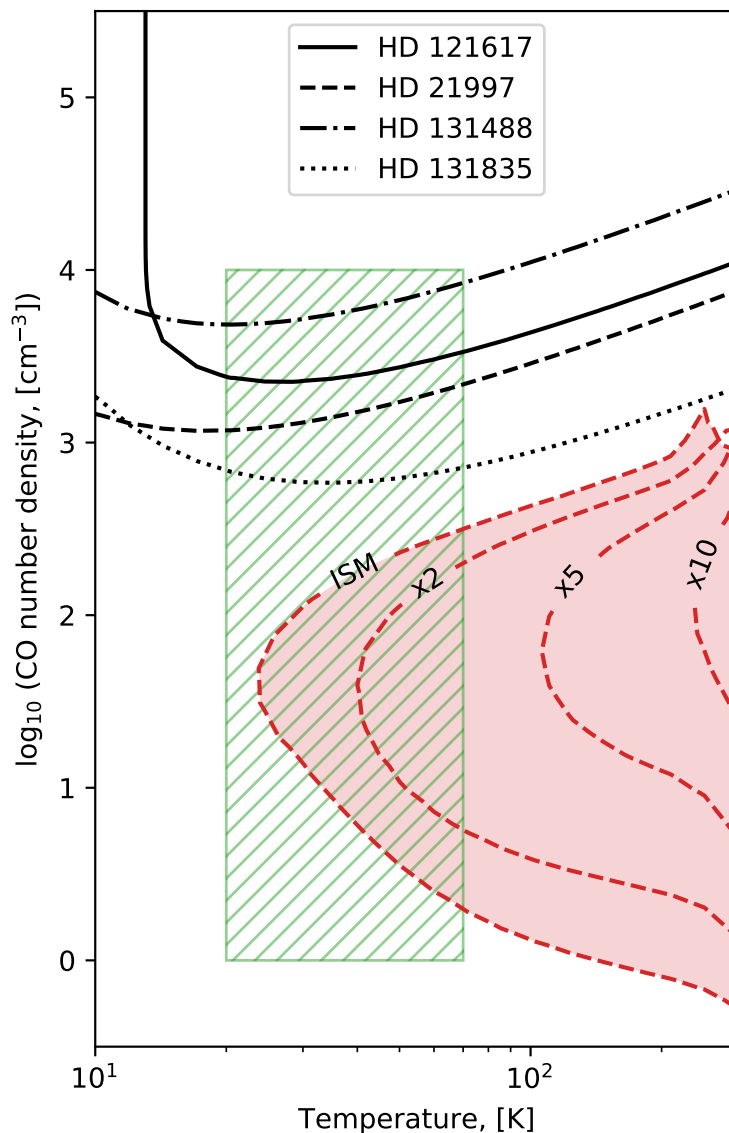


Figure 3.7: Modelled parameter space. Black lines: midplane densities at which the observed CO isotopolog brightness temperatures become fitted in the four debris disks. Green rectangle: a range of temperatures and densities representative of the debris disks. Red filled contours: parameter combinations that lead to bright, detectable HCO<sup>+</sup> line emission (compared to the <sup>13</sup>CO intensity), which contradicts the HCO<sup>+</sup> non-detections in the debris disks. Each red dashed contour corresponds to the different initial abundance sets. For the ISM-like or moderately H<sub>2</sub>-depleted abundances, the low-density regions of the debris disk shall contribute to the HCO<sup>+</sup> emission, which could be detected by deeper ALMA observations. If H<sub>2</sub> is more severely depleted, by a factor of 5 or larger, HCO<sup>+</sup> molecules cannot form in sufficient amount under the debris disk conditions.

The alternative scenario, where the disk gas is already partially or fully depleted of  $\text{H}_2$  shows lower  $\text{HCO}^+$  abundances and hence the  $\text{HCO}^+$  fluxes. Our model with the lowest  $\text{H}_2$  depletion factor of 2 still produces enough  $\text{HCO}^+$  to overcome the current detection limit at higher temperatures ( $> 40$  K) and volume densities about  $80 \text{ cm}^{-3}$ . However, starting from a higher  $\text{H}_2$  depletion factor of 5, all the predicted  $\text{HCO}^+$   $J=2-1/^{13}\text{CO}$   $J=2-1$  flux ratios fall below the current detection limit.

Lower  $\text{H}_2$  concentrations (with respect to CO) in the  $\text{H}_2$ -poor cases lead to the less efficient formation of the main driver of the gas-phase chemistry,  $\text{H}_3^+$ . This, in turn, makes abundances of all observed molecules apart from CO also lower by factors of at least several or higher. According to our KIDA-based model,  $\text{H}_3^+$  is produced via  $\text{H}_2 + \text{H}_2^+$  reaction driven by the cosmic ray ionization of  $\text{H}_2$ . Next,  $\text{H}_3^+$  can react with CO and form  $\text{HCO}^+$  and atomic H.  $\text{H}_3^+$  can also react with atomic C and produce  $\text{CH}^+$  and  $\text{H}_2$ . Another starting route for hydrocarbon chemistry is a slow radiative association reaction between  $\text{C}^+$  and  $\text{H}_2$  that leads to  $\text{CH}_2^+$ . Both  $\text{CH}^+$  and  $\text{CH}_2^+$  can react with  $\text{H}_2$ , forming bigger  $\text{CH}_n^+$  ions ( $n = 3 - 5$ ). These light hydrocarbon ions can be neutralised by dissociative recombination with electrons and then undergo carbon insertion reactions with  $\text{C}^+$ , forming larger  $\text{C}_2\text{H}_n^+$  species ( $n \geq 0$ ). These  $\text{C}_2$ -hydrocarbon ions can react with  $e^-$  and form neutral  $\text{C}_2$ -hydrocarbons, such as  $\text{C}_2\text{H}$  molecule targeted in our observations.

Furthermore, hydrocarbon chemistry is also a key for the formation of nitriles via ion-molecule or neutral-neutral reactions involving atomic N. A key ion-molecule reaction is  $\text{CH}_3^+ + \text{N} \rightarrow \text{HCNH}^+ + \text{H}$ , followed by dissociative recombination of  $\text{HCNH}^+$  into CN or HCN or HNC (with equal probability). Slower barrierless neutral-neutral reactions between N and either CH or  $\text{CH}_2$  produce H and either CN or HCN/HNC. Thus, the lack of  $\text{H}_2$  in the scenario when debris disk has secondary origin could explain the overall deficit of molecular species other than CO.

### 3.5.3 Effect of hydrogen depletion on disk scale height

An alternative method to estimate hydrogen depletion of a debris disk using ALMA is based on direct measurements of their vertical temperature and density structure (Hughes et al. 2017; Kral et al. 2019). In the case of hydrostatic equilibrium, the vertical scale height is defined by the molar mass and temperature. In the simplest case of an isothermal and geometrically thin disk atmosphere, scale height  $H$  is defined as:

$$H = \sqrt{\frac{RT}{\mu} \frac{r^3}{GM}}, \quad (3.1)$$

where  $R$  is the ideal gas constant,  $T$  is the gas temperature,  $\mu$  is the gas molar mass,  $r$  is the radial distance to the star,  $G$  is the gravitational constant, and  $M$  is the stellar mass. The measurements of the scale height were performed below, for example, for the edge-on debris disk around 49 Ceti Hughes et al. (2017) estimated that the disk scale height is smaller by 25% compared to the value predicted from the temperature measurements and assuming the ISM-like,  $\text{H}_2$ -rich gas.

In the case of hydrogen depletion, the gas molar mass becomes higher, as it is not dominated by the molecular hydrogen and helium any more. The molar mass of a gas mixture could be calculated as:

$$\mu = \frac{\sum_i X_i \mu_i}{\sum_i X_i}, \quad (3.2)$$

where  $X_i$  is an abundance of the  $i$ -th species, and  $\mu_i$  is its molar mass.

To illustrate this effect, we use the elemental abundances from Table 3.6 and scale abundances of all the species other than molecular hydrogen and helium by uniform fac-

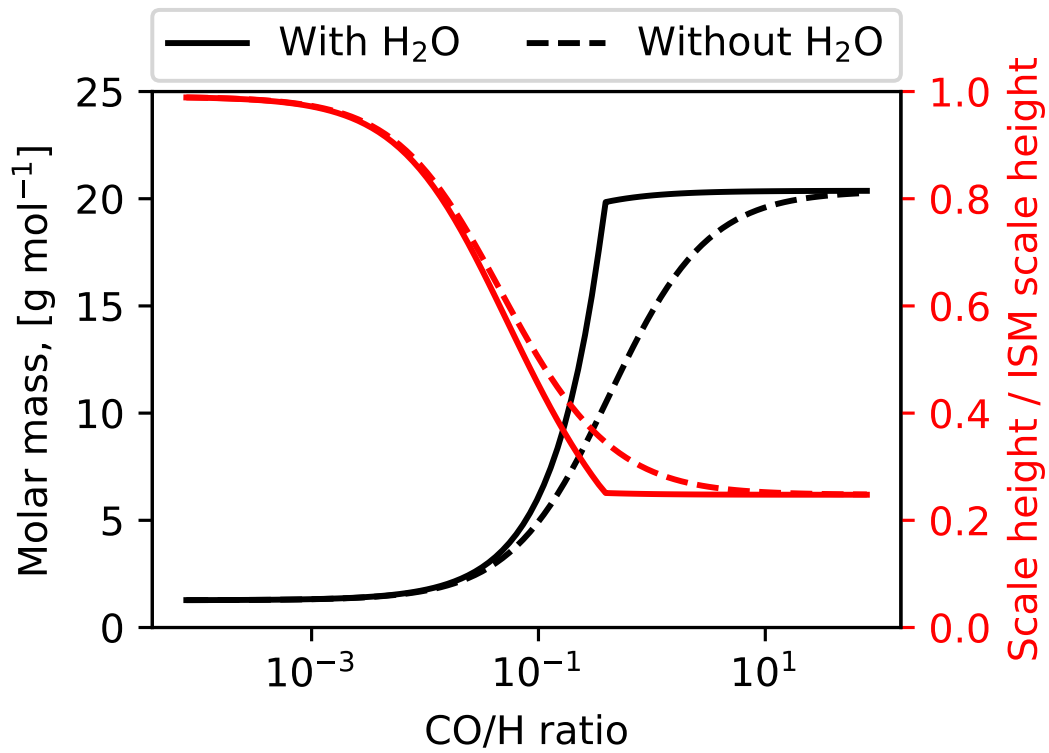


Figure 3.8: Gas molar mass (black) and disk scale height (red) as a function of relative CO abundance with respect to hydrogen. Solid line: gas consisting of CO, H<sub>2</sub>O, N, H<sub>2</sub>, He. Dashed line: gas consisting of CO, O, N, H<sub>2</sub>, He.

tors of 1 (ISM-like) to  $10^6$  (hydrogen is almost fully depleted). The resulting elemental abundances are then reshuffled into various major molecules, assuming simplistic chemistry. First, all available carbon is assumed to be locked in CO molecules. Then, the remaining oxygen and available hydrogen are assumed to form water molecules. After that, the remaining hydrogen (if any) is assumed to be bound in  $H_2$  molecules. As water can be rapidly photodissociated in the optically thin debris disk, we consider two extreme cases – with and without water formation. The resulting gas molar masses and the corresponding scale heights for an isothermal, 30 K disk are shown in Fig. 3.8. The effect of hydrogen depletion on the disk scale height becomes noticeable as soon as the CO/H ratio is above  $\sim 10^{-2}$ . For example, the scale height measured in the 49 Ceti disk by (Hughes et al. 2017) would correspond to the CO/H ratio of about  $2 \times 10^{-2}$  in this case.

If there is a vertical temperature gradient, the hydrostatic equilibrium and the corresponding ideal gas equation are as follows:

$$\begin{cases} \frac{dP(z)}{dz} = -\rho(z)g_z = -\rho(z)\frac{GM_z}{(r^2+z^2)^{3/2}} \\ P(z) = \frac{\rho(z)RT(z)}{\mu} \end{cases} \quad (3.3)$$

By differentiating the ideal gas equation and assuming that the gas molar mass  $\mu$  is constant, one derives:

$$\frac{dP(z)}{dz} = \frac{R}{\mu} \left( T(z) \frac{d\rho(z)}{dz} + \rho(z) \frac{dT(z)}{dz} \right) \quad (3.4)$$

Combining the above equations, we can get the equation to measure the local gas molar mass directly:

$$\mu = -\frac{RT(z)(r^2+z^2)^{3/2}}{GM_z} \left( \frac{d \ln \rho(z)}{dz} + \frac{d \ln T(z)}{dz} \right) \quad (3.5)$$

If vertical density  $\rho(z)$  and temperature  $T(z)$  profiles could be reliably measured from the observations, the gas molar mass could also be derived from this Eq. 3.5. This would require further high-resolution ALMA observations of the multi-J CO lines in edge-on-oriented debris disks, as has been tried for 49 Ceti.

## 3.6 Conclusions

We present ALMA Band 5 and 6 observations of four debris disks (HD 21997, HD 121617, HD 131488, HD 131835), and five old Herbig Ae disks (HD 139614, HD 141569, HD 142666, HD 145718, HD 100453). We run the standard CASA pipeline with natural weighting to produce continuum images and emission lines data cubes. We have measured fluxes in elliptical apertures and estimated the noise by comparison with other apertures at other locations of the data cube. All disks were detected in the dust continuum and CO isotopologs, while other targeted lines (CN, HCN, HCO<sup>+</sup>, C<sub>2</sub>H, and CS) were only detected in the Herbig Ae disks. The upper limits of the flux ratios to CO isotopolog lines in debris disks were found to be significantly lower than the ratio in Herbig Ae disks, except for C<sub>2</sub>H, which we did not detect in all the Herbig Ae disks, and thus do not have strict constrain.

We performed detailed chemical modelling using a parameter grid to find physical conditions and elemental abundance combinations that could reproduce this behaviour. We found that in the optically thin debris disks, where molecules other than CO and H<sub>2</sub> are rapidly photodissociated, HCO<sup>+</sup> is the only relatively abundant and potentially detectable molecule. This requires the emitting gas to be warmer than 20 K and the CO density to be low, about 3 – 300 cm<sup>-3</sup>. In the scenario when the debris disk is of secondary origin and is hydrogen-poor, the predicted molecular abundances and hence line fluxes are significantly lower. In this case, the calculated line fluxes scale with the degree of the hydrogen depletion.

We also propose that higher-resolution studies of the vertical distribution of the debris disk gas could be used to constrain its elemental composition. The lack of hydrogen and helium in the scenario when the gas is collisionally produced should increase the gas molar mass above the ISM-like value of 2.3 g mol<sup>-1</sup>, resulting in the noticeable decline in the local scale height.

The spatial resolution and reached sensitivity of our ALMA observations did not allow us to verify the exact origin of the gas in the studied four debris disks. Thus, future detection(s) of HCO<sup>+</sup> or the CO data obtained at higher resolution are needed to provide a clearer view on the nature of the debris disk gas.

## Acknowledgements

This research makes use of the following ALMA data: ADS/JAO.ALMA#2017.1.01545.S and 2018.1.01429.S. ALMA is a partnership of ESO (representing its member states), NSF (USA) and NINS (Japan), together with NRC (Canada) and NSC and ASIAA (Taiwan) and KASI (Republic of Korea), in cooperation with the Republic of Chile. The Joint ALMA Observatory is operated by ESO, AUI/NRAO and NAOJ. This work has made use of data from the European Space Agency (ESA) mission *Gaia* (<https://www.cosmos.esa.int/gaia>), processed by the *Gaia* Data Processing and Analysis Consortium (DPAC, <https://www.cosmos.esa.int/web/gaia/dpac/consortium>). Funding for the DPAC has been provided by national institutions, in particular the institutions participating in the *Gaia* Multilateral Agreement. This research has made use of the VizieR catalogue access tool, CDS, Strasbourg, France (DOI : 10.26093/cds/vizieR). The original description of the VizieR service was published in A&AS 143, 23. A.M. and P. Á. acknowledge support from the grant KH-130526 of the Hungarian NKFIH. D.S. acknowledges financial support by the Deutsche Forschungsgemeinschaft through SPP 1833: “Building a Habitable Earth” (SE 1962/6-1). A.M.H. is supported by a Cottrell Scholar Award from the Research Corporation for Science Advancement. This work was supported by “Programme National de Physique Stellaire” and “Programme Physique et Chimie du Milieu Interstellaire”(PNPS and PCMI from INSU/CNRS). Authors acknowledge the impact of the open-source Python community, and, particularly, the developers and maintainers of Astropy, NumPy, Matplotlib, seaborn, pandas.

## Data Availability

The data underlying this chapter are available in the ALMA Science Archive and can be accessed with (2017.1.01545.S and 2018.1.01429.S, PI: Th. Henning).

### 3.7 App. A: Results of the continuum observations

Our observations enabled us to characterise the continuum emission of the nine disks at 1.27 mm (in Band 6) and 1.65 mm (in Band 5). Although the data analysis is performed in the visibility space, for completeness, continuum images of the disks are also presented in Fig. 3.9. We used the `UVMULTIFIT` package (ver. 3.0, Martí-Vidal et al. 2014) to fit the obtained visibility data in the  $uv$  plane by a geometrical model. Only channels free from line emission were considered. The data weights in the measurement set were updated with the `STATWT` task before the fitting process. We adopted an elliptical Gaussian model, where the axis ratio (computed from the inclinations) and the position angle ( $PA$ ) were fixed based on literature data (see Table 3.7) leaving four free parameters: the positional offsets with respect to the phase center, the total flux density of the fitted component ( $F_{\nu}$ ), and the full width half maximum (FWHM) of the major axis. In the case of HD 121617 the axis ratio and the  $PA$  were also fitted because these parameters are less constrained in the literature than for the other targets. After the fitting, we used the `CASA TCLEAN` task to image the residuals obtained as the difference of the measurement and best fit model. We found that the images of HD 141569 display an extended residual emission implying the presence of an additional broader disk component. This is in good agreement with the findings of previous high-resolution millimeter continuum observations of the source (White & Boley 2018; Miley et al. 2018; Di Folco et al. 2020). With this in mind, for this target, we used a two-component model. For the Band 5 observation, where the central component could not be resolved, a combination of a point source and an elliptical Gaussian was adopted, while the shorter wavelength data was fitted by combining two elliptical Gaussian components.

Comparing the centre of the fitted models with the Gaia EDR3 positions of the stars (corrected for proper motion) we found no significant offsets. The obtained flux densities and disk sizes (FWHMs of the major axes) with their uncertainties are presented in Table 3.7. The quoted uncertainties of the flux densities in parentheses are quadratic sums of the measurements errors and absolute calibration errors. The latter component is conservatively assumed to be 10%<sup>1</sup>.

---

<sup>1</sup>According to the ALMA Technical handbook ([https://arc.iram.fr/documents/cycle6/ALMA\\_Cycle6\\_Technical\\_Handbook.pdf](https://arc.iram.fr/documents/cycle6/ALMA_Cycle6_Technical_Handbook.pdf)) the accuracy of the flux calibration is  $\leq 10\%$  in these bands.

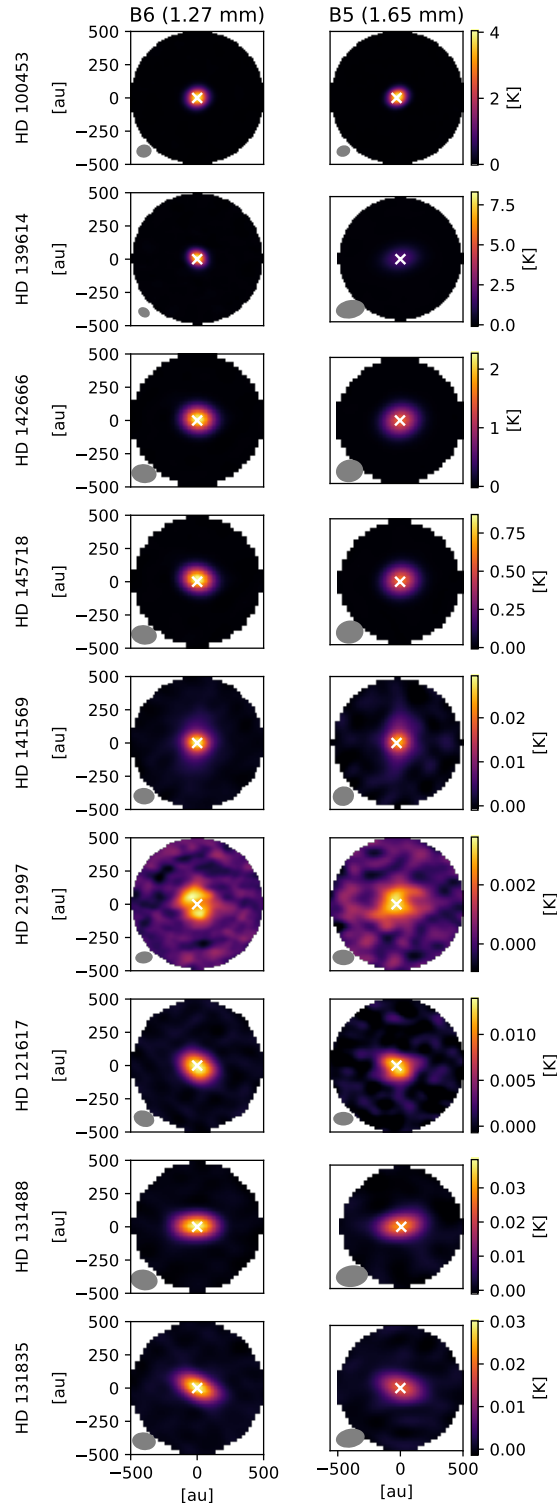


Figure 3.9: ALMA Band 5 and Band 6 continuum emission for the observed disks. To produce these images we used the CASA task `tclean` function with a Briggs robust parameter of 0.5 and considered data from all line-free channels. The colorbar units are K.

Table 3.7: Continuum results. Flux densities and disc sizes (FWHMs of the major axes) are derived by fitting the obtained visibility data. Apart from the case of HD 121617, where these parameters are also estimated from our measurements, inclination and positional angle data are taken from the literature (for references see the last column).

Target name	Wavelength (mm)	$F_\nu$ (mJy)	FWHM (arcsec)	$i$ (deg.)	$PA$ (deg.)	Ref.
HD 21997	1.27	1.88±0.14 (0.23)	3.3±0.2	32.9	21.5	Moór et al. (2013)
	1.65	1.21±0.17 (0.21)	3.4±0.4			
HD 121617	1.27	1.67±0.05 (0.17)	1.34±0.06	43.9±3.0	53.5±4.0	
	1.65	0.92±0.05 (0.10)	1.42±0.13	43.4±8.6	59.8±12.3	
HD 131488	1.27	2.86±0.04 (0.29)	1.17±0.05	82	96	Moór et al. (2017)
	1.65	1.64±0.04 (0.17)	1.10±0.11			
HD 131835	1.27	2.59±0.04 (0.26)	1.44±0.05	79	59	Kral et al. (2019)
	1.65	1.40±0.05 (0.15)	1.53±0.10			
HD 141569	1.27	1.55±0.10 (0.18)	0.39±0.12	53	356	Di Folco et al. (2020)
		2.47±0.17 (0.30)	3.51±0.20			
	1.65	0.74±0.07 (0.10)	-			
		1.66±0.15 (0.22)	3.25±0.31			
HD 100453	1.27	218.1±1.3 (21.8)	0.64±0.01	29.5	151.0	van der Plas et al. (2019)
	1.65	110.9±0.8 (11.1)	0.65±0.01			
HD 139614	1.27	191.5±0.6 (19.2)	0.50±0.01	17.6	276.5	Muro-Arena et al. (2020)
	1.65	98.1±0.7 (9.8)	0.49±0.01			
HD 142666	1.27	120.3±0.2 (12.0)	0.41±0.01	62.2	162.1	Huang et al. (2018b)
	1.65	67.9±0.1 (6.8)	0.44±0.01			
HD 145718	1.27	44.8±0.7 (4.5)	0.30±0.01	70.4	1.0	Ansdell et al. (2020)
	1.65	26.0±0.3 (2.6)	0.28±0.03			

## **Chapter 4**

# **Machine learning-accelerated chemistry modeling of protoplanetary disks**

---

With the large amount of molecular emission data from (sub)millimeter observatories and incoming James Webb Space Telescope infrared spectroscopy, access to fast forward models of the chemical composition of protoplanetary disks is of paramount importance.

We used a thermo-chemical modeling code to generate a diverse population of protoplanetary disk models. We trained a K-nearest neighbors (KNN) regressor to instantly predict the chemistry of other disk models.

We show that it is possible to accurately reproduce chemistry using just a small subset of physical conditions, thanks to correlations between the local physical conditions in adopted protoplanetary disk models. We discuss the uncertainties and limitations of this method.

The proposed method can be used for Bayesian fitting of the line emission data to retrieve disk properties from observations. We present a pipeline for reproducing the same approach on other disk chemical model sets.

*Published as Smirnov-Pinchukov et al. (2022a) in by Grigorii V. Smirnov-Pinchukov, Tamara Molyarova, Dmitry A. Semenov, Vitaly V. Akimkin, Sierk van Terwisga, Riccardo Francheschi, and Thomas Henning. VA has developed ANDES code based on chemical model ALCHEMIC developed by DS. TM has extended ANDES to run grids of models. All co-authors have contributed to the discussions of the methods and the results. I have proposed the original idea, performed all the simulations and machine learning tests, generated figures.*

*astrochemistry – methods: numerical – protoplanetary disks – stars: pre-main sequence – ISM: molecules – submillimeter: planetary systems*

---

## 4.1 Introduction

Time-dependent gas-grain chemical kinetics codes are widely used in the astrochemical modeling of the ISM, protoplanetary disks, and even exoplanetary atmospheres. A typical computational time to calculate the chemical evolution of an isolated volume over  $10^5 - 10^6$  years usually takes about 0.1–10 seconds on a single CPU core, depending on the complexity of the chemical network and variability of the physical conditions. More complex networks – that include deuterium or carbon isotopologues (Albertsson et al. 2013; Yu et al. 2016) or that separately treat reactions on dust surface and in the bulk of icy mantles (Vasyunin et al. 2009; Garrod 2013) – increase the number of reactions and slow down the calculations drastically. For a typical grid size of a 2D protoplanetary disk model of  $100 \times 100$ , a session of chemical kinetics modeling takes at least 15 minutes up to several days on a single CPU core. This is a reasonable timeframe for forward modeling but too long for any retrieval of disk physical parameters based on a fitting of molecular data. Recently, Keil et al. (2022) proposed a new method for deriving the physical parameters of uniform gas clouds using Markov chain Monte Carlo sampling with realistic chemical and radiative transfer modeling and successfully applied it to the L1544 data. However, protoplanetary disks exhibit more complex structures with strong gradients of physical conditions and another approach is thus needed.

With the recent large programs on protoplanetary disk chemistry at the Atacama Large Millimeter/submillimeter Array (ALMA) (MAPS: Öberg et al. (2021); 2021.1.00128.L/AGE-PRO PI: Ke Zhang, in progress; see also Guzmán et al. (2021); Ilee et al. (2021)) and Northern Extended Millimeter Array (NOEMA) (L19ME/PRODIGE, PI: P. Caselli, Th. Henning., in progress, see Semenov et al., in prep.), as well as large, partially spatially unresolved surveys of circumstellar disk populations (ODISEA: Cieza et al. 2019; Ansdell et al. 2016), the amount of available data for analysis expands rapidly. In addition, high angular- and frequency-resolution observations of molecular emission lines in individual disks are now common (e.g., Pegues et al. 2020; Garufi et al. 2020; Pegues et al. 2021). Analyses of such data can be vastly improved if all the lines are taken into account simultaneously (Fedele & Favre 2020; Holdship & Viti 2022). However, protoplanetary disk model retrieval in a Bayesian sense is still in its infancy.

Our goal is to build a function (an estimator) to return the reasonably accurate chemical composition using the smallest possible subset of local physical conditions characterizing the protoplanetary disk. Applications of machine learning techniques are emerging in all fields of astronomy and physics (e.g., Dieleman et al. 2015; Dunjko & Briegel 2018; Carleo et al. 2019; Ribas et al. 2020; Ardévol Martínez et al. 2022), providing a robust, human-independent, and flexible way to find dependencies and correlations within a data set. The approach is also being applied to astrochemistry: among others, Lee et al. (2021) searched for similarities between molecules to propose possible detectable molecules, Grassi et al. (2021) suggested a method to reduce the number of species for chemical kinetics, Holdship et al. (2021) explored a large parameter space to provide time-dependent chemistry, and, most recently, Villadsen et al. (2022) presented a way to predict binding energies of molecules on dust surfaces.

In this work, we present a solution to the problem of chemical model performance. We computed a grid of 540 thermo-chemical protoplanetary disk models, containing more than two million physical bins in various disk environments, but at fixed elemental and dust compositions and at the same age, which we describe in Section 2. We used a K-nearest neighbors (KNN) machine learning (ML) algorithm (Goldberger et al. 2005) to create a robust interpolation between local physical conditions in the disk and the abundances of molecular and atomic species, described in detail in Section 3. Once

Table 4.1: ANDES input grid

Parameter	Value
$M_{\text{star}}$	0.2, 0.3, 0.4, 0.5, 0.8, 1.0 $M_{\odot}$
$M_{\text{disk}}$	0.001, 0.003, 0.01, 0.03, 0.1 $M_{\text{star}}$
$R_c$	20, 50, 80, 100, 130, 170 au
$L_X$	$10^{29}$ , $10^{30}$ , $10^{31}$ erg s <sup>-1</sup>
$T_{\text{star}}, R_{\text{star}}$	$f(M_{\text{star}})$ Yorke & Bodenheimer (2008)
UV excess	$B_{\nu}(T_{\text{eff}} = 10000 \text{ K})$
Accretion rate	$1 \times 10^{-8} M_{\odot} \text{ yr}^{-1}$
Dust opacity	Draine & Lee (1984)
Mean dust grain size	$3.7 \times 10^{-5}$ cm
Dust-to-gas mass ratio	0.01
Grazing angle	0.05
Density power-law slope	-1

Table 4.2: Initial chemical abundances

Species	Abundance $n(\text{X}) / n(\text{H})$	Species	Abundance $n(\text{X}) / n(\text{H})$
ortho-H <sub>2</sub>	0.375	CH <sub>4</sub> ice	$1.8 \times 10^{-5}$
para-H <sub>2</sub>	0.125	CO ice	$6.0 \times 10^{-5}$
HD	$1.55 \times 10^{-5}$	CH <sub>3</sub> OH ice	$4.5 \times 10^{-5}$
H	$5.0 \times 10^{-7}$	CO <sub>2</sub> ice	$6.0 \times 10^{-5}$
He	0.098	CH <sub>4</sub> ice	$1.8 \times 10^{-5}$
Cl	$1.0 \times 10^{-9}$	H <sub>2</sub> O ice	$3.0 \times 10^{-4}$
Si	$8.0 \times 10^{-9}$	H <sub>2</sub> S ice	$6.6 \times 10^{-6}$
Fe	$3.0 \times 10^{-9}$	N <sub>2</sub> ice	$2.1 \times 10^{-5}$
Mg	$7.0 \times 10^{-9}$	NH <sub>3</sub> ice	$2.1 \times 10^{-5}$
Na	$2.0 \times 10^{-9}$	P	$2.0 \times 10^{-10}$

the estimator is trained, the chemistry can be predicted in milliseconds per disk model, making it much faster than the next bottleneck, namely, the line radiative transfer. In Section 4, we demonstrate the performance and limitations of the method on a small set of chemical species. In Section 5, we summarize our findings.

## 4.2 Thermo-chemical protoplanetary disk model grid

Chemical kinetics models, such as *ALCHEMIC* (Semenov et al. 2010), *NAUTILUS* (Ruaud et al. 2016), *UCLCHEM* (Holdship et al. 2017), and *KROME* (Grassi et al. 2014) can be very flexible and include dozens to tens of thousands of parameters. Some of these parameters describe local physical conditions, such as gas and dust density and temperature as well as the local ultraviolet (UV) radiation field. Others are global parameters, for instance, the ionization rate by radioactive nuclides or such details as the probability modifier of a gas particle sticking to a dust grain after a collision, which affect a large fraction of the considered chemical reaction network. The initial elemental or molecular composition of the matter make up another set of important input parameters. In addition, the chemical network itself contains an extensive data set of reaction rates, with only  $\sim 30\%$  of the rate values known to an adequate level of accuracy.

Classical chemical kinetics codes can utilize any combination of these parameters, but most parameters are fixed in real applications. Also, some parameters could correlate between various chemical calculations. For example, it is reasonable to expect that the low-density, high-temperature regions of protoplanetary disks lie in the disk atmosphere, where the chemistry is dominated by a limited set of photo- and gas-phase reactions. On the other hand, cold and dense disk regions are typical for the midplane, where photochemistry is much less important and gas-grain interactions and surface reactions play a major role. This simple observation has led to the idea of constructing simplified chemical models that allow for quick computations that are nonetheless feasible to establish the abundances of simple species such as CO, without the need for full chemical modeling (Williams & Best 2014). Unfortunately, such approaches cannot be easily generalized to predict disk chemical composition for a larger set of observed molecules or important coolants.

To create a reference data set of protoplanetary disks with known chemical structures, we used the *ANDES* astrochemical model of a 2D axisymmetric hydrostatic disk. It employs a chemical network based on the *ALCHEMIC* network (Semenov & Wiebe 2011), with deuterium-bearing molecules and deuterium fractionation included following Albertsson et al. (2013, 2014a). The network describes 1247 species and 38347 reactions, including gas-phase and surface two-body reactions, adsorption and reactive desorption, photoreactions, and ionization or dissociation by X-rays, cosmic rays, and radioactive nuclides (Akimkin et al. 2013; Molyarova et al. 2017, 2018). The rates of surface reactions are adjusted to mimic the chemical inactivity of the bulk icy mantles; they are multiplied by a factor equal to the fraction of the upper layers in the total number of surface particles. Following Eistrup et al. (2016), we adopted an icy molecular initial composition based on the abundances of prestellar cores (Öberg et al. 2011). We ran the time-dependent chemical evolution for the typically assumed age of 1 Myr (Willacy et al. 1998; Aikawa et al. 2002).

The disk physical structure in our models is defined through stellar mass,  $M_{\text{star}}$ , disk mass,  $M_{\text{disk}}$ , and the characteristic radius,  $R_c$ ; these parameters define the distribution of density, temperature, and radiation field in the  $(R, z)$  plane. The stellar mass governs the stellar temperature and luminosity, which are calculated at the age of 1 Myr using the evolutionary models by Yorke & Bodenheimer (2008). The X-ray radiation field is calculated using Bruderer et al. (2009). The interstellar cosmic ray ionization rate was calculated according to Padovani et al. (2018). We create an ensemble of 540 models with different stellar mass  $M_{\text{star}}$ , disk mass,  $M_{\text{disk}}$ , critical radius,  $R_c$ , and stellar X-ray luminosity,  $L_X$ , to cover a wide range of physical conditions typical for protoplanetary disks:  $M_{\text{star}} = 0.2 \dots 1.0 M_{\odot}$ ,  $M_{\text{disk}} = 0.1 \dots 10 \% M_{\text{star}}$ ,  $R_c = 20 \dots 170$  au,

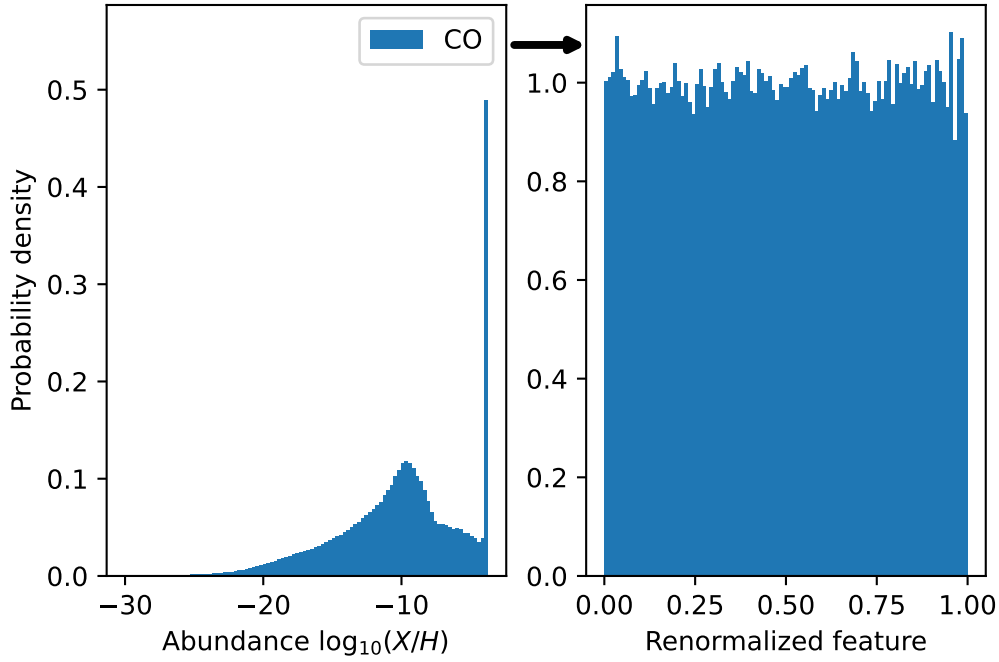


Figure 4.1: Example of the re-normalization of  $\log_{10} X_{\text{CO}}$  abundance prior to interpolation. The peak at  $-4$  in the unnormalized data corresponds to the condition when all the available C and O form CO.

and  $L_X = 10^{29...31} \text{ erg s}^{-1}$ . Each model includes 50 logarithmically spaced radial points in the range of  $R = 0.1...1000 \text{ au}$  and 80 vertical points in the range of  $z/R = 0...1$ . The dust size distribution is described by a power law with a  $-3.5$  exponent between  $5 \times 10^{-7}$  and  $2.5 \times 10^{-3} \text{ cm}$ . The UV radiation field for photoreactions is calculated using dust opacities based on Draine & Lee (1984). An averaged grain size of  $3.7 \times 10^{-5} \text{ cm}$  is adopted for surface reaction rates. The UV excess from accretion is defined as  $L_{\text{acc}} = 1.5 G \dot{M}_{\text{acc}} M_{\text{star}} / R_{\text{star}}$ . The effective temperature of the accretion region is assumed to be 10000 K. A summary of these parameters is presented in Table 4.1. With 4000 spatial points in each model, we have 2 160 000 points in total, sampling the chemical model output in conditions typical of protoplanetary disks. The total computing resource usage for the data generation took about 1 core year.

### 4.3 KNN estimator training

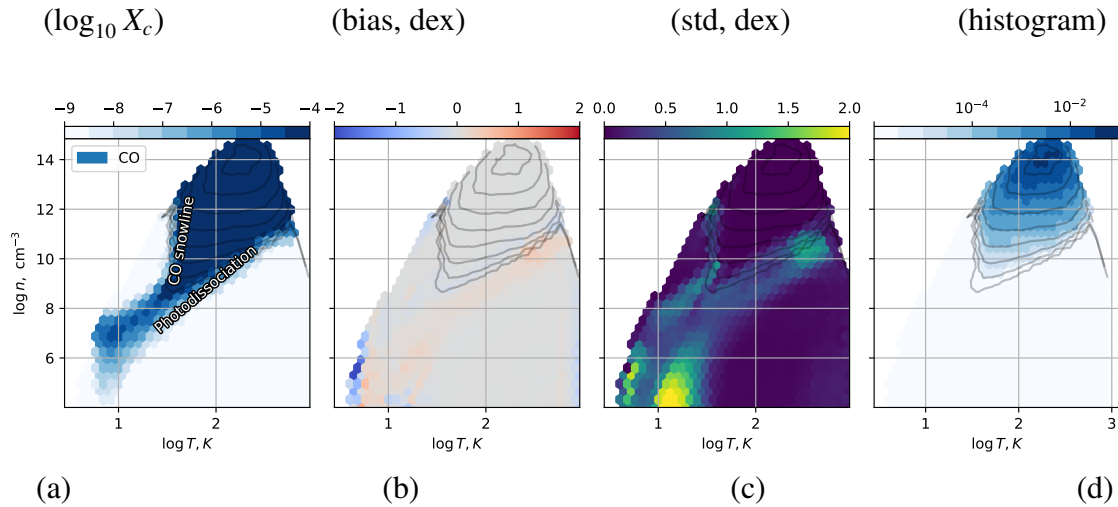


Figure 4.2: Performance of ML-accelerated chemistry predictions for CO. (a): mean  $\log_{10}$  predicted relative abundance as a function of local temperature, gas density, and ionization rate. Darker areas correspond to larger relative (to H atoms) abundance. (b): median of the difference between the predicted values and test set data (bias, dex), in dex, as a function of temperature and density. Gray areas correspond to an unbiased fit. (c): the standard deviation between the predicted values and test set data, in dex (std, dex). (d): relative density (histogram) of species within the data points, with contours, which are also present on other panels. Various regions of the protoplanetary disk are described on panel (a). A detailed description of the processes leading to this figure is in the main text. Other molecules are shown in Fig. 4.3.

First, we built a data frame using `pandas` (Reback et al. 2021), which contains a subset of local physical parameters and a set of selected chemical species. For demonstration purposes, we chose CO,  $\text{HCO}^+$ ,  $\text{DCO}^+$ , and electrons, relevant to ionization studies (Smirnov-Pinchukov et al. 2020; Aikawa et al. 2021). We also demonstrate the possible applications to other species in Appendix 4.6. We have selected observationally-relevant disk positions with gas number density above  $10^4 \text{ cm}^{-3}$ , resulting in 1 183 212 data points. The subsequent analysis was performed using the `Scikit-learn` python library (Pedregosa et al. 2011). The physical quantities (input features) and the chemical abundances normalized to the total number of H atoms (output features) were renormalized to a uniform distribution in order to make the parameter space more uniformly sampled (see the example in Fig. 4.1). We split the data into a training set (432 disks, 946586 points) and a test set (108 disks, 236626 points). All the points from a single disk model must appear either in the training or a test set to avoid overfitting. The algorithm should predict the new points based on points from the other disks rather than interpolating nearby points of the same disk.

We used the `KNeighborsRegressor` estimator (Goldberger et al. 2005). The algorithm finds the  $k$  nearest data points (in the input feature space) and interpolates the output feature values between them. For robustness, we choose the median value of these data points. The value of  $k$  should be chosen based on the data. If  $k = 1$ , it is a classical “nearest” interpolation. This sort of interpolation is very sensitive to outliers (overfitting) which, in our case, can represent a rare combination of parameters or even a numerical failure of the original chemical kinetics solver within ANDES. If  $k$  is too large, then the local behavior of chemistry cannot be properly caught. In the worst case, where  $k$  equals

the number of data points, the solution would simply represent their median value.

We used cross-validation to choose the value of  $k$  and ensure the quality of the interpolation. In this approach, the training set is divided into 10 parts (splits), with all points from each disk being in the same split. The estimator is trained on 9/10 of the training data set and its performance is benchmarked against the remaining part, using the square sum of errors metric in the renormalized space to quantify the quality of the fit. This is repeated for each split, and the average performance is estimated. Then the same procedure repeats for another value of  $k$ , and this way, the best-performing value of  $k$  is found. The estimator with the best  $k$  is fitted again afterward on the entire training set. The results can be saved as a python binary (“pickle”) file and used as a fast callable function in other applications.

## 4.4 Results and discussion

First, we chose the local gas density, dust temperature, and ionization rate (the minimum set of key physical parameters for chemistry) as input features. We provide an example of the performance of the fit in Fig. 4.2, using the gas-phase CO molecule. As seen in panel (a), CO is abundant in dense regions with a temperature above 30 K. Typically, the CO snowline should be at around 20 K. However, in our modeling, CO is also absent in the gas at higher temperatures due to the chemical transformation into CO<sub>2</sub> on dust grain surfaces (Molyarova et al. 2017; Bosman et al. 2018). At lower densities, which correspond to the outer disk, photodesorption by the interstellar UV and ionizing radiation maintain some amount of CO in the gas phase, enough for self-shielding. Low-density and high-temperature areas belong to the disk atmosphere, where the UV-radiation destroys CO. The fit reproduces this general behavior, showing insignificant systematic error (bias, dex) on the panel (b). The fit scatter (panel c) is especially low ( $< 0.5$  dex) for the inner disk and midplane. Most of the disk CO gas is present in the inner disk and, hence, the fit reproduces the majority of the gas-phase CO in disks with a reasonable level of accuracy. Moreover, the fit correctly predicts low CO abundances outside the CO snowline and in the disk atmosphere. Significant scatter (above 1 dex) is present only at the radiation-sensitive transition zone between the atmosphere and the rest of the disk in the low-density area. The top-left corner (very high density, very low temperature) is not covered by the original data set, as regions with such conditions never appeared in the disk model grid.

Notably, we can reproduce deuterium fractionation. In Fig. 4.3, we show other species included in the estimator's output: HCO<sup>+</sup>, DCO<sup>+</sup>, and  $e^-$ . While electron density is fitted almost perfectly, the HCO<sup>+</sup> and DCO<sup>+</sup> fits show  $\sim 1$  dex scatter in the transition zone between the inner disk and the photodissociation area, where just a small amount of gas is present. Overall, with just three inputs' feature set, the estimator is able to predict the disk chemistry with a good accuracy below 0.5 dex for most of the parameter space.

The addition of more input parameters to the input features further increases the quality of the fit. In Fig. 4.4, we show the model after adding local UV radiation intensity to the set of the input features. We can see a significantly lower scatter in the whole parameter space. Temperature and density remain the best predictors of the disk chemistry, explaining the major variations of  $\gg 5$  dex, with the local ionization rate contributing to  $\sim 1 - 2$  dex and ultraviolet field contributing to  $\sim 1$  dex in relevant disk regions. The impact of ionizing radiation is more important than the UV for the molecules, as they reside in the deeper layers of the disk, while X-ray and cosmic rays penetrate deeper towards the midplane. Even in the three-parameter fit, it is important to take the local UV radiation field into account for the data generation process. Nevertheless, as the UV field is correlated with the combination of other input parameters, it is not necessary to have it as an input feature for the KNN algorithm.

## 4.5 Conclusions

We applied, for the first time, a machine-learning estimator to physical-chemical protoplanetary disk models to predict chemical abundances much more quickly than traditional "full" chemical calculations. Our estimator uses a small and easily-calculated set of local physical parameters as input features: the dust temperature, density, and ionization rate, with the possible addition of a local UV radiation strength. We applied this method to a pre-computed database of 540 protoplanetary disks of various masses, sizes, and stellar properties, including X-ray luminosities. We studied the effectiveness and limitations of the method due to the small input feature set, demonstrating how the addition of a local UV field improves the accuracy for four species in the gas: CO, HCO<sup>+</sup>, DCO<sup>+</sup>, and e<sup>-</sup>.

This approach is general and can be applied not only to this set of species and ANDES thermo-chemical disk models, but also to other species and astrochemical applications. For such purposes, the outputs of other astrochemical models (e.g., Bruderer et al. 2009; Woitke et al. 2009) with relevant physical parameters and desired chemical species abundances can be processed with the same approach. We publish the ANDES-generated data and the Jupyter notebook to reproduce our results on GitHub <sup>1</sup>. These results will be used in an upcoming series of papers to fit the molecular data obtained in the framework of the large observing program on NOEMA, L19ME (PI: Th. Henning). We use this method to rapidly calculate chemical composition for the Bayesian retrieval of disk physical parameters using CO isotopologues (Francheschi et al., in prep.) and a combined fit of CO and HCO<sup>+</sup> isotopologues (Smirnov-Pinchukov et al., in prep).

## Acknowledgements

The authors acknowledge the contribution of the Python open-source community for providing high-quality data analysis tools. All figures were created using `matplotlib` (Hunter 2007). GSP thanks Morgan Fouesneau, Ivelina Momcheva, and Markus Schmalzl for discussions about machine learning at MPIA. TM and VA were supported by the grant 075-15-2020-780 (N13.1902.21.0039) of Ministry of Science and Higher Education of the Russian Federation. TH and DS acknowledge support from the European Research Council under the Horizon 2020 Framework Program via the ERC Advanced Grant Origins 83 24 28.

---

<sup>1</sup>[https://github.com/SmirnGreg/diskchef\\_chemistry](https://github.com/SmirnGreg/diskchef_chemistry)

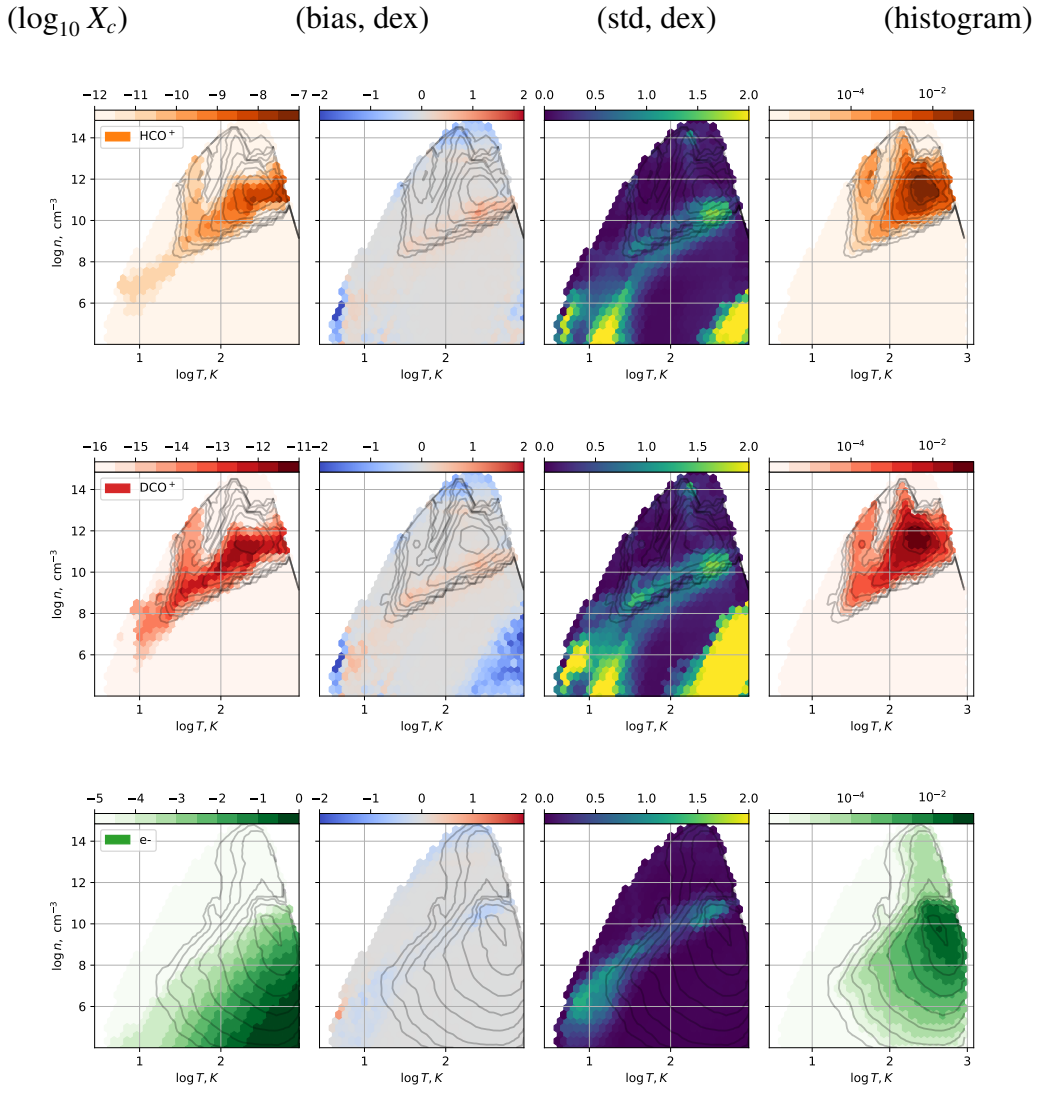


Figure 4.3: Performance of ML-accelerated chemistry predictions for  $\text{HCO}^+$ ,  $\text{DCO}^+$ , and electrons.

## 4.6 App. B: Additional figures

Fig. 4.3 demonstrates the application of the method on  $\text{HCO}^+$ ,  $\text{DCO}^+$ , and electrons for three input features: local temperature, gas density, ionization rate. On the Fig. 4.4 we present the result for the same molecules and CO with the local UV radiation strength added to the features list. In addition, we used our study to demonstrate the summary of the same method application to a larger number of different species, with four input features in Fig. 4.5.

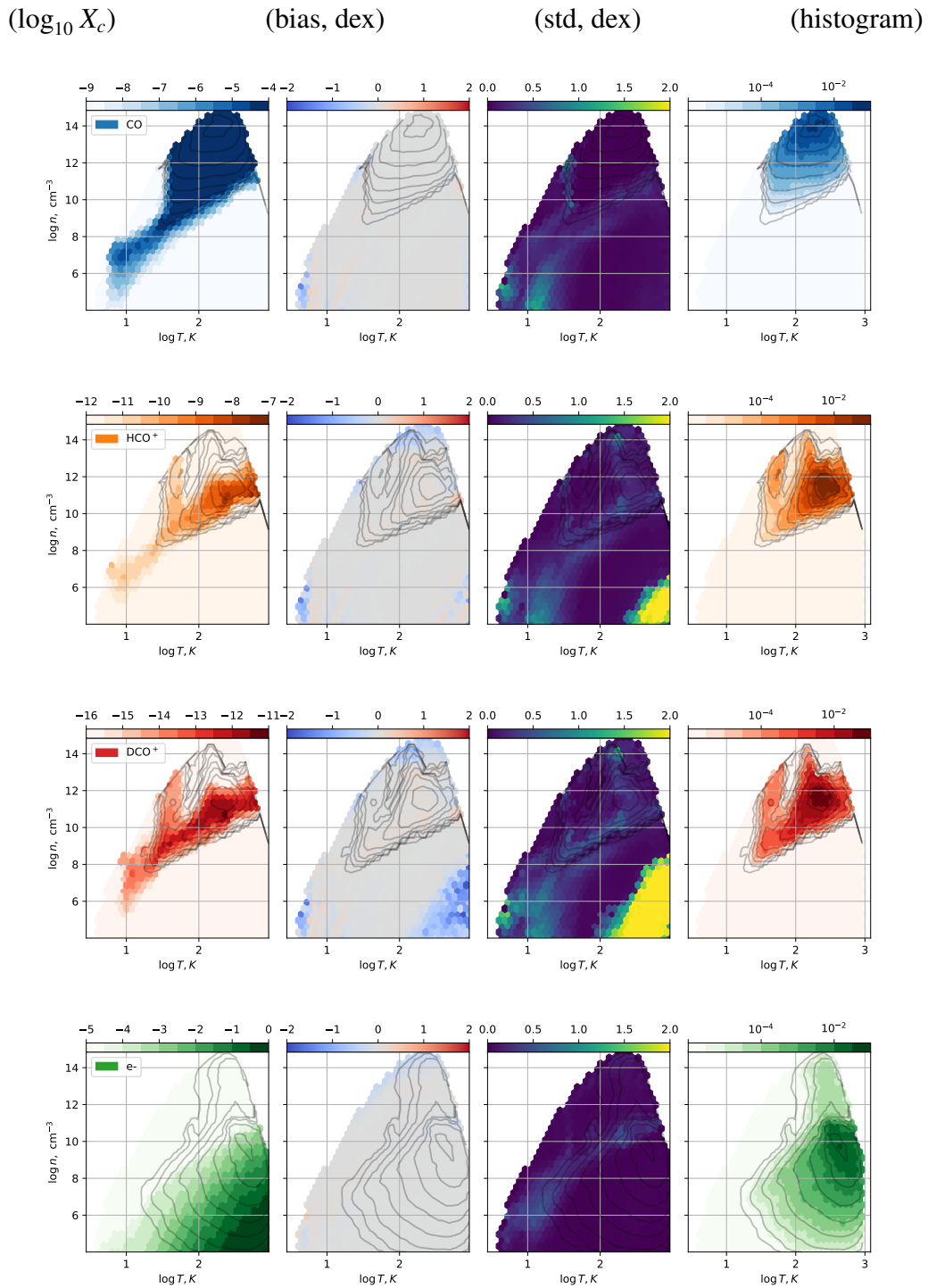


Figure 4.4: Effect of adding UV radiation strength to the set of input features. The panels show the performance of ML-accelerated chemistry predictions, as in Fig. 4.2. Adding UV radiation strength increases the accuracy of the fit, but only slightly in the areas of the parameter space dominated by the selected molecules. Depending on the molecular species and constraints on calculation time, it is not necessary to use UV as a parameter.

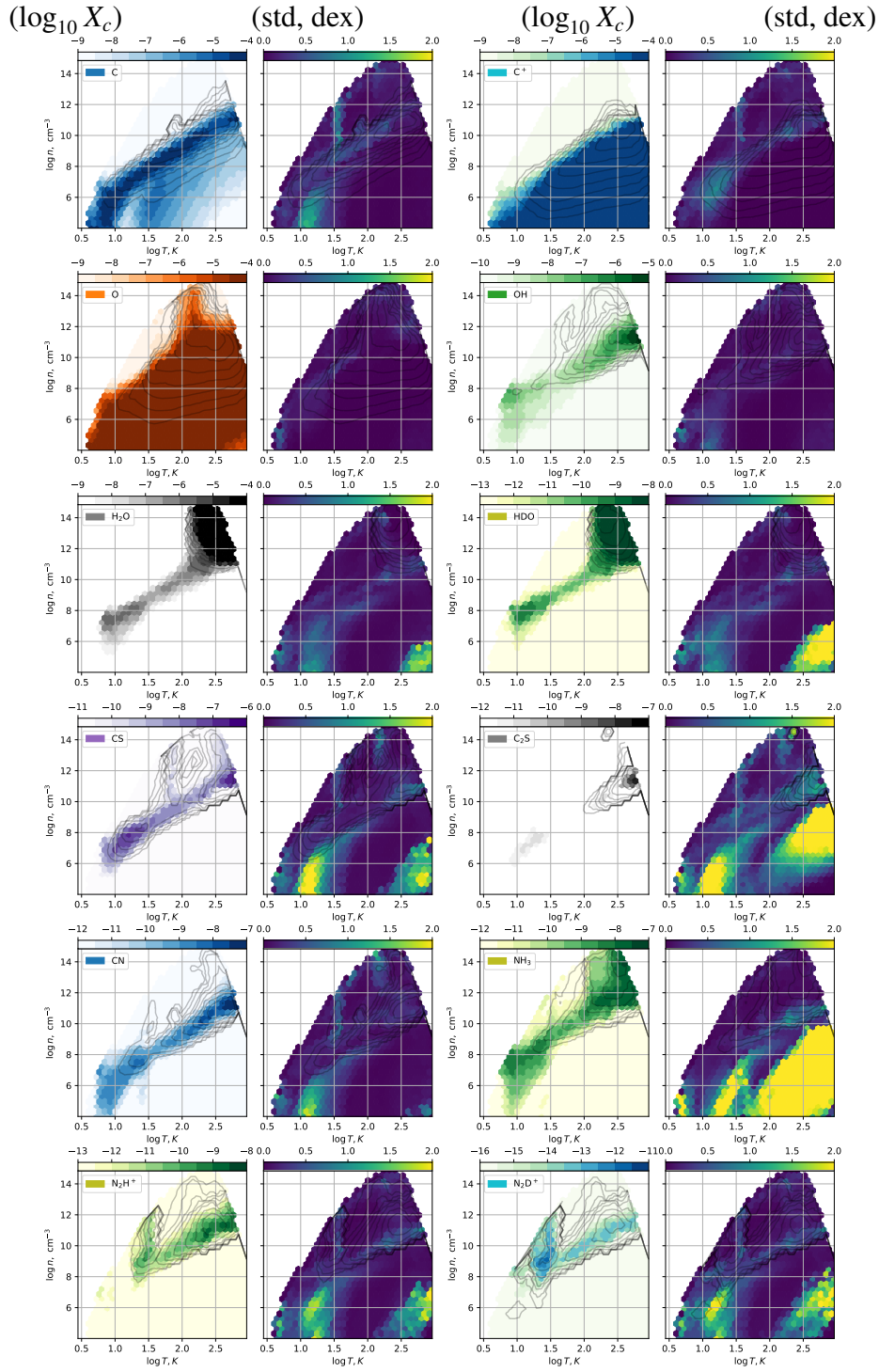


Figure 4.5: Application of the same method to a broader set of species. Performance of ML-accelerated chemistry prediction, same as in Fig. 4.2, based on four input features.

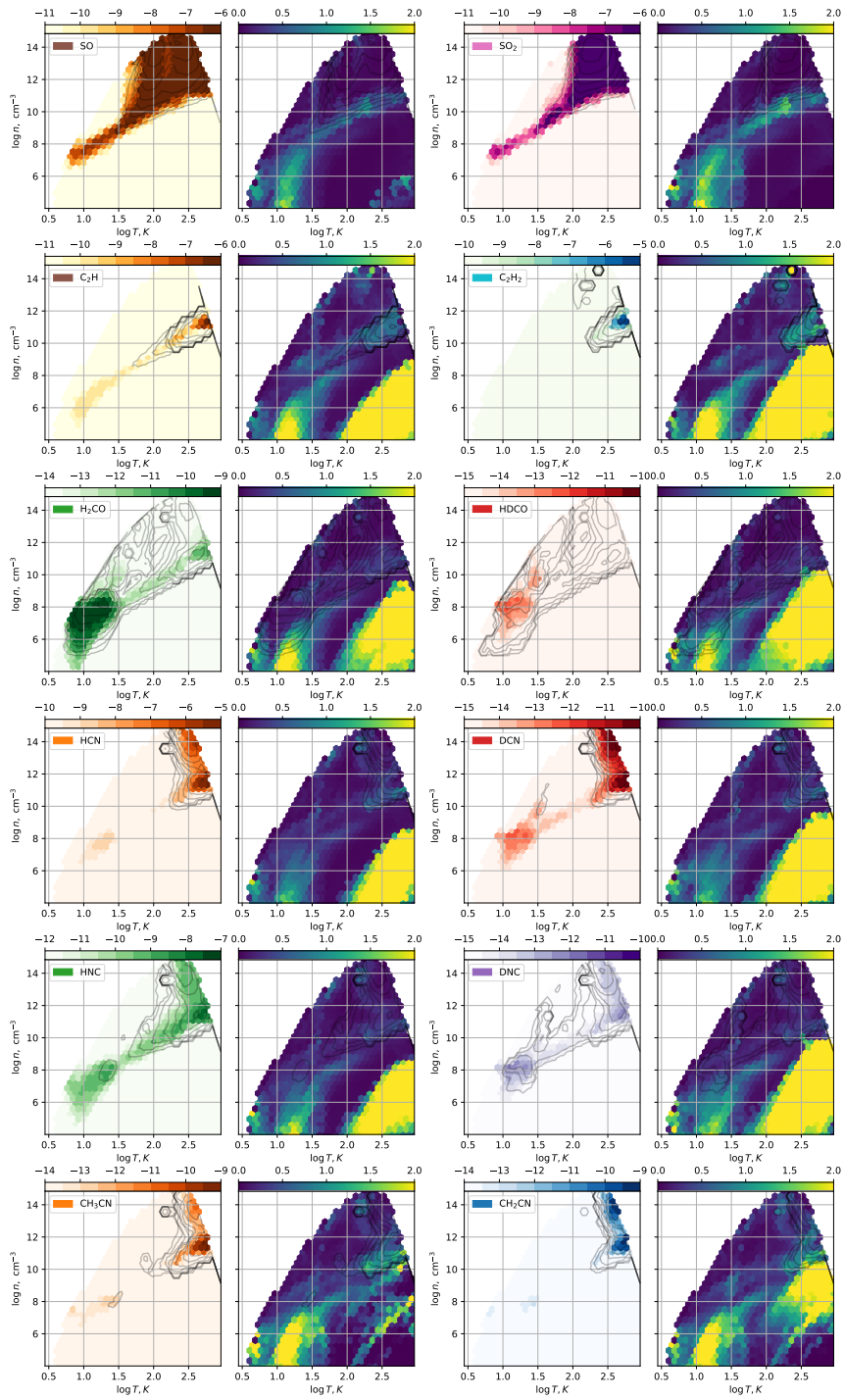


Figure 4.5: continued.

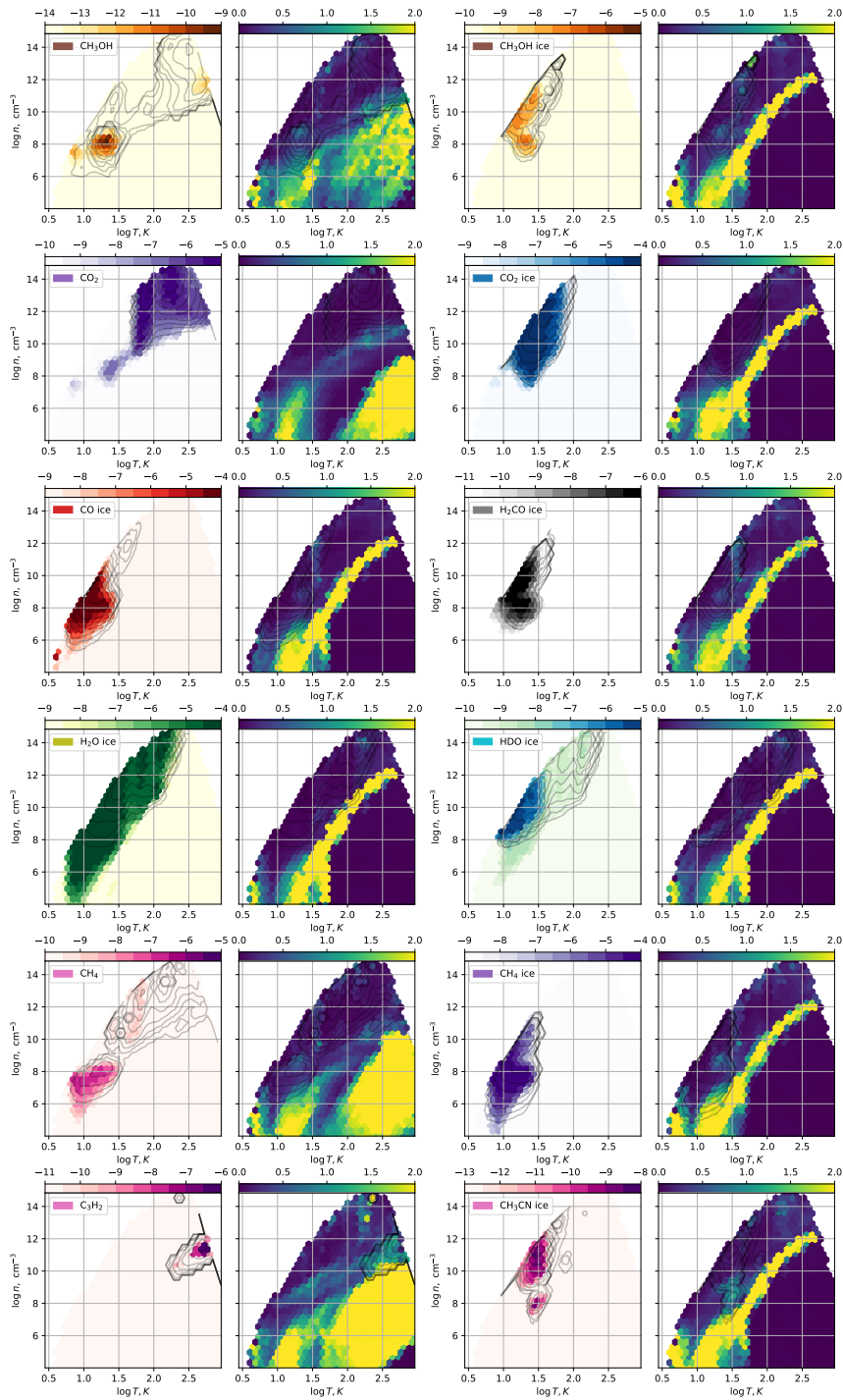


Figure 4.5: continued.



# Chapter 5

## A sample from PRODIGE data

---

In this chapter of the thesis, I provide yet unpublished data and the first application example of the ML-accelerated chemistry described in Chapter 4. Protoplanetary disks DN Tau and CI Tau have been observed in a framework of NOEMA large program L19ME (PRODIGE). Here I demonstrate the channel and moment maps of CO and HCO<sup>+</sup> isotopologs, discuss the pipeline for mapping the physical parameters with the observed emission, and present first, very preliminary, fitting of DN Tau CO isotopologs data.

*Richard Teague and PRODIGE collaboration have participated in the preparation of the proposal S19AW which lead to collection of these data. PRODIGE collaboration includes, among others, Edwige Chapillon, Stephane Guilloteau, Anne Dutrey, Vincent Piètu, Dmitry Semenov, Riccardo Franceschi. The preliminary interferometric data reduction was performed with support by Edwige Chapillon and Stephane Guilloteau. I was the PI of the original proposal and a co-I of the PRODIGE large program. I have tuned and used the pipeline to image the data from the u-v tables, generated the figures, and developed the fitting pipeline DiskCheF which first application is demonstrated in this chapter.*

*astrochemistry – methods: numerical – protoplanetary disks – ISM: molecules – submillimeter: planetary systems – individual: DN Tau, CI Tau*

---

## 5.1 Ionization of protoplanetary disks and formylium isotopologs

There are several primary ionization sources which regulate the ionization state in the protoplanetary disks: stellar and interstellar UV radiation, stellar X-rays, and cosmic ray particles (CRPs). The high energies of CRPs allow them to penetrate the full gas column of a protoplanetary disk over  $100 \text{ g cm}^{-2}$  and, therefore, dominate the ionization in the midplane (Cleeves et al. 2014, 2015b; Ivlev et al. 2016). Conversely, UV radiation is stopped relatively quickly in the upper atmosphere of the disk by  $0.01 \text{ g cm}^{-2}$ . X-rays, with typical energies of  $0.3 - 10 \text{ keV}$ , can penetrate a gas column of up to  $1 \div 10 \text{ g cm}^{-2}$ , dominating the ionization in the intermediate layers (Teague et al. 2015; Igea & Glassgold 1999). Recently proposed Stellar Energetic Particles (SEP) may have a similar ionizing potential, but it sensitively depends on the assumed stellar atmospheric model (Rab et al. 2017). To better understand what drives the disk ionization, one has to understand whether there is a correlation between the stellar X-ray luminosity or mass and the ionization fraction (see e.g., Teague et al. (2015)). A recent proof that the stellar X-rays may indeed dominate the disk ionization came from the observed variability of the optically thin  $\text{H}^{13}\text{CO}^+$  emission in IM Lup due to X-ray flaring (Cleeves et al. 2016).

In order to probe the vertical ionization structure, one has to use different probes that are sensitive to particular ionization sources (Dutrey et al. 2014b). Chemical modeling suggests that  $\text{HCO}^+$ ,  $\text{H}^{13}\text{CO}^+$  and  $\text{DCO}^+$  provide the best opportunity to probe the ionization structure in the “warm molecular layer” of the disk. All  $\text{HCO}^+$  isotopologue abundances are sensitive to the X-ray luminosities (Favre et al. 2015). In the presence of gaseous CO,  $\text{HCO}^+$  is rapidly formed through the proton transfer from  $\text{H}_3^+$ , a direct product of X-ray ionization processes, to CO.  $\text{DCO}^+$  forms via an equivalent deuteron transfer reaction from other  $\text{H}_3^+$  isotopologues. The resulting effect of deuterium fractionation was discussed in the Chapter 2. The  $\text{HCO}^+$  was used as a proxy for ionization in the midplane of the protoplanetary disks in the MAPS sample (Aikawa et al. 2021).

Both  $\text{HCO}^+$  and  $\text{DCO}^+$  therefore exhibit a strong correlation between their column densities and the stellar X-rays reaching their location: higher fluxes yield higher abundance. Both ions are also sensitive to the interstellar UV flux, but are not particularly sensitive to dust grain size and cosmic rays. Changes in the disk mass gives a somewhat similar effect to the impact of X-rays, but we can disentangle it with the combination of optically thick  $\text{HCO}^+$ , moderately optically thick  $\text{DCO}^+$ , and optically thin  $\text{H}^{13}\text{CO}^+$ .  $\text{HCO}^+$  and  $\text{H}^{13}\text{CO}^+$  are cospatial, while  $\text{DCO}^+$  produced by deuterium chemistry lies in deeper, colder regions, which are less affected by X-rays. Thus,  $\text{HCO}^+$  and  $\text{DCO}^+$  provide us with readily observable tracers of disk ionization structure.

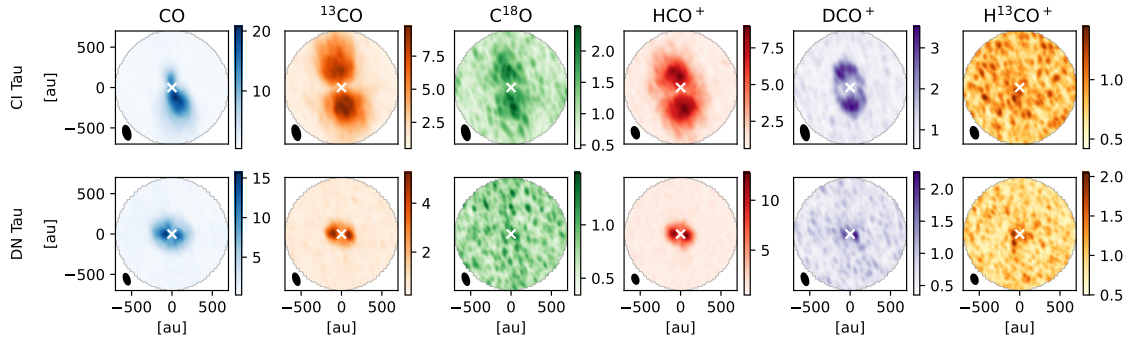


Figure 5.1: CI Tau and DN Tau peak brightness maps. Colorbar units are K.

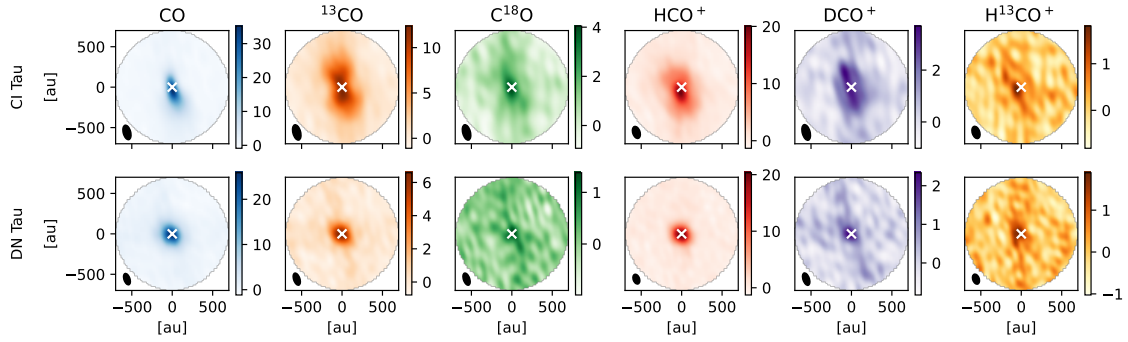


Figure 5.2: CI Tau and DN Tau moment 0 maps. Colorbar units are  $\text{K km s}^{-1}$ .

## 5.2 Observations

We present the two disks (CI Tau and DN Tau) and six lines (CO J=2-1,  $^{13}\text{CO}$  J=2-1,  $\text{C}^{18}\text{O}$  J=2-1,  $\text{HCO}^+$  J=3-2,  $\text{DCO}^+$  J=3-2,  $\text{H}^{13}\text{CO}^+$  J=3-2) out of the complete NOEMA large program PRODIGE (LM19ME, PI: Henning; S19AW, PI: Smirnov-Pinchukov) sample. The disks were chosen for the pilot study as they were studied in the continuum observation program of Long et al. (2018). Each source was observed independently (no track-sharing) with 1 to 4 tracks per spectral setup using the quasars J0438+300 and 0507+179 as phase calibrators, 3C84 as the bandpass calibrator, and LkHa 101 as a flux calibrator. The setup 1 contained CO isotopologs lines and  $\text{DCO}^+$  centered around 224.9 GHz, and the setup 2 contained  $\text{HCO}^+$  and  $\text{H}^{13}\text{CO}^+$  centered around 256.2 GHz. Observations were carried out by 10 antennae. The setup 1 utilized exclusively the C configuration, and setup 2 had  $\approx 33\%$  time in a more sensitive configuration D. The dates of observations are listed in Table 5.1. The raw data were reduced and calibrated at

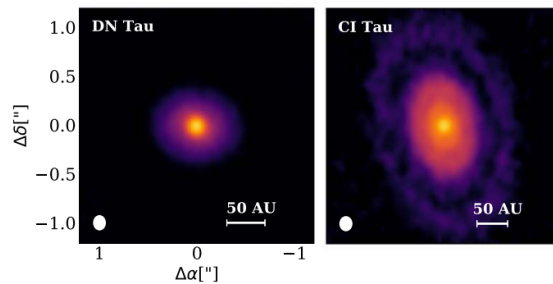


Figure 5.3: DN Tau and CI Tau 1.33 mm continuum maps, adopted from Long et al. (2018).

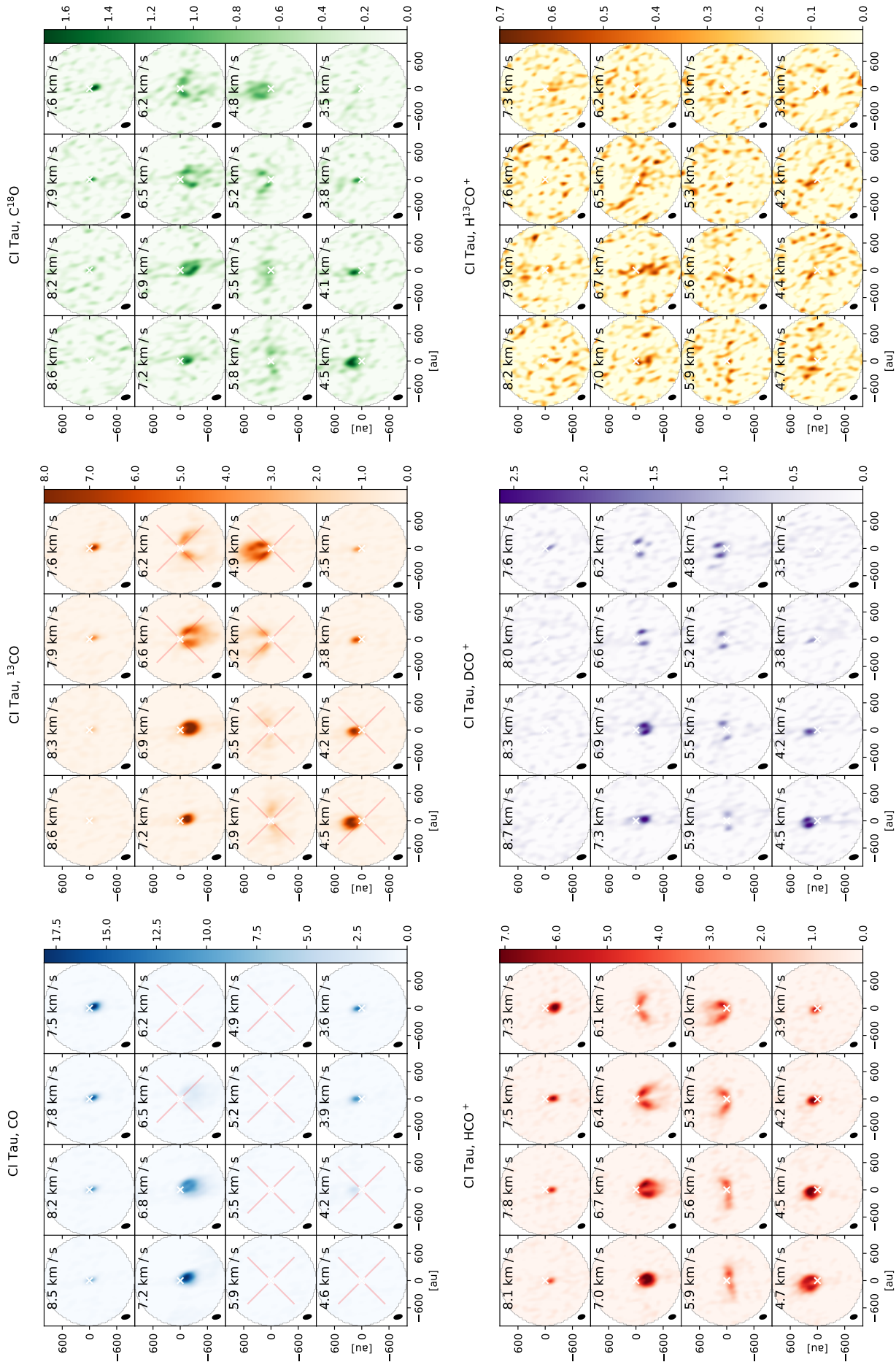


Figure 5.4: CI Tau channel maps from the NOEMA large program PRODIGE. Channels were re-binned by a factor of 4 for visualization purposes. Foreground cloud absorption for CI Tau is seen on CO channel map, between 6.5 and 4.2  $\text{km s}^{-1}$ .

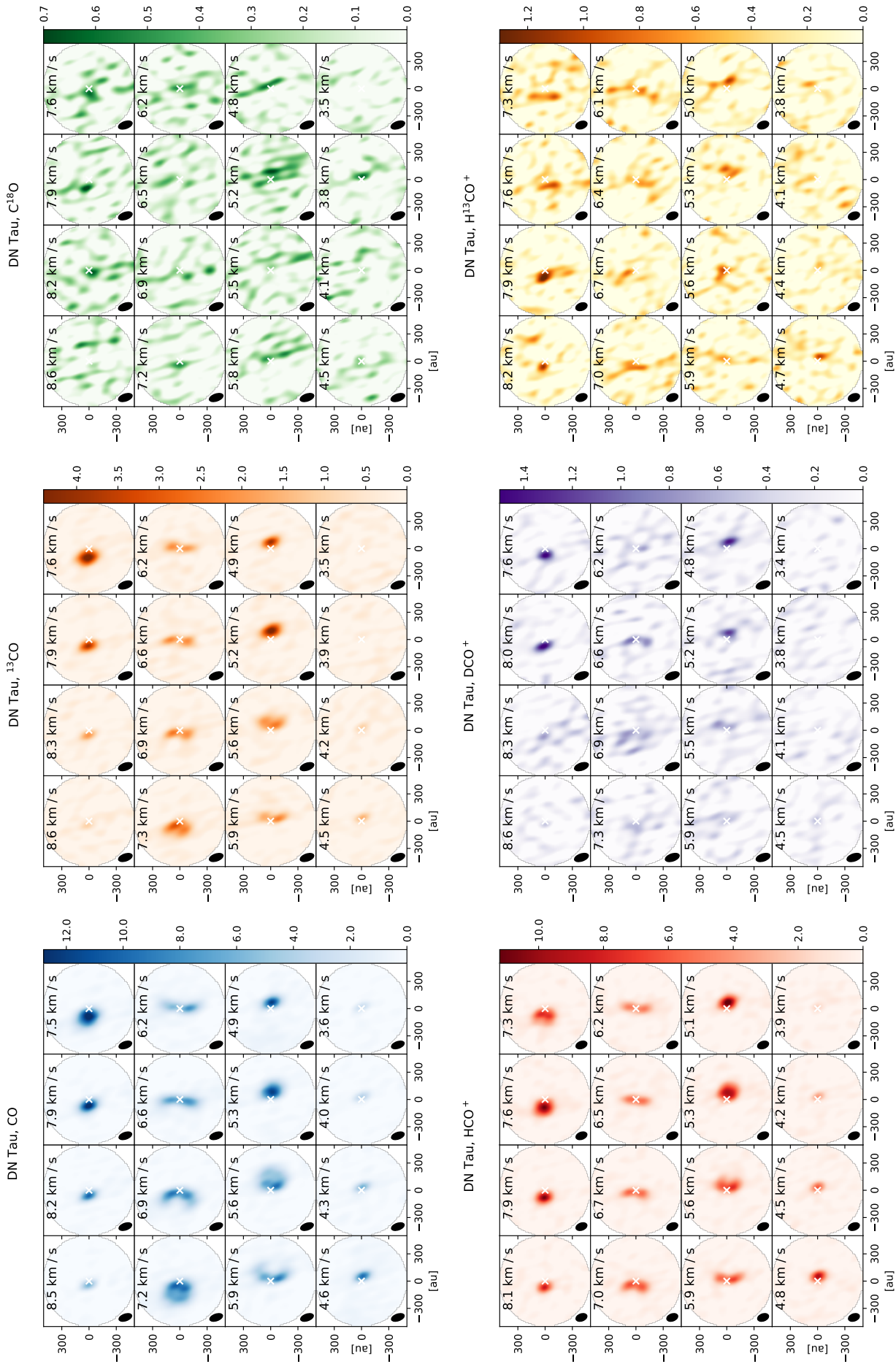


Figure 5.5: DN Tau channel maps from the NOEMA large program PRODIGE. Channels were re-binned by a factor of 4 for visualization purposes.

Table 5.1: Dates of NOEMA S19AW observations

	DN Tau
Setup 1	09-JAN-2020, 11-JAN-2020, 02-APR-2020
Setup 2	C: 27-DEC-2019, 06-JAN-2020; D: 28-DEC-2019, 13-MAR-2020
	CI Tau
Setup 1	13-JAN-2020, 14-JAN-2020, 07-APR-2020
Setup 2	C: 28-DEC-2019, 11-JAN-2020; D: 12-JAN-2020

IRAM. Self-calibration and imaging were performed using the new GILDAS/IMAGER<sup>1</sup> pipeline.

The imaged data cubes are presented on Figs 5.1-5.3. CI Tau is partially obscured by foreground cloud at  $4.2 \div 6.5 \text{ km s}^{-1}$  LSR velocity range, which is seen most prominent in CO and  $^{13}\text{CO}$ . The newly developed fitting procedure described in more details below will be used to analyze these data. The more focused study of these and the rest of the disks when the rest of the data from the program will be available later available (Semenov et al., Francheschi et al., in prep).

<sup>1</sup><https://imager.oasu.u-bordeaux.fr/>

### 5.3 Protoplanetary disk model

Our protoplanetary disk model, used for fitting, is fairly simple, even though the framework DiskCheF we have developed for this purpose allows a very flexible model generation. First, we generate the physical model of protoplanetary disk, following a recipe by Williams & Best (2014). In our implementation, the pipeline is the following:

1. The midplane and atmosphere temperatures are defined as

$$T_{\text{mid/atm}} = T_{\text{mid/atm}, 100 \text{ au}} \left( \frac{r}{100 \text{ au}} \right)^{-q},$$

where  $r$  is local radial distance (distance between the projection of the point on the midplane and the star),  $T_{\text{mid/atm}, 100 \text{ au}}$  are temperatures at radial distance of 100 astronomical units from the star in the midplane and atmosphere, and  $q$  is a slope of the temperature profile. Here and later, the parameters of the models are written in *bold italics*.

2. The pressure scale height  $H_p$  at given radius is defined as

$$H_p(r) = \sqrt{\frac{RT_{\text{mid}}r^3}{GM_{\text{star}}\mu}},$$

where  $R = N_A k_B \approx 8.31 \text{ J mol}^{-1} \text{ K}^{-1}$  is the ideal gas constant,  $G$  is gravitational constant,  $M_{\text{star}}$  is the mass of the star, and  $\mu$  is the molar weight (in  $\text{kg mol}^{-1}$ ) of the gas.

3. The gas temperature at a given height is defined as

$$T(r, z) = \begin{cases} T_{\text{mid}} + (T_{\text{atm}} - T_{\text{mid}}) \cdot \left( \sin \frac{\pi z}{8H_p} \right)^4, & \text{if } z < 4H_p; \\ T_{\text{atm}}, & \text{if } z \geq 4H_p. \end{cases}$$

Dust temperature is assumed to be equal to the gas temperature.

4. Column density  $\Sigma$  at each radius is given by

$$\Sigma_0 = (2 - \gamma) \frac{M_{\text{gas}}}{2\pi r_c^2} \exp\left(\frac{r_{\text{in}}}{r_c}\right)^{2-\gamma},$$

$$\Sigma(r) = \Sigma_0 \left(\frac{r}{r_c}\right)^{-\gamma} \exp\left[-\left(\frac{r}{r_c}\right)^{2-\gamma}\right]$$

where  $\gamma$  and  $r_c$  are tapering factor and critical radius,  $M_{\text{gas}}$  is the total gas mass, and  $r_{\text{in}}$  is the inner disk radius.

5. The local gas volume density is calculated on a fine grid by integrating the vertical hydrostatic equilibrium equation with a normalization at each radius given at the previous item, and then interpolated to the model grid:

$$\hat{\rho}(r, z) = \exp\left(-\int_0^z \left[ \left( \frac{GM_{\text{star}}z'}{(r^2 + z'^2)^{3/2}} \right) \left( \frac{\mu}{RT} \right) + \frac{\partial \ln T}{\partial z} \right] dz'\right)$$

$$\rho_0(r) = \Sigma(r) \left( \int_0^{+\infty} \hat{\rho}(r, z) dz \right)^{-1}$$

$$\rho(r, z) = \rho_0(r) \hat{\rho}(r, z)$$

6. The local dust density is a fraction of a local gas density.

In this parametrization, the disk’s gas temperature and density distributions are defined by stellar mass  $M_{\text{star}}$ , disk mass  $M_{\text{disk}}$ , inner radius  $r_{\text{in}}$ , critical radius  $r_c$ , tapering factor  $\gamma$ , midplane temperature at 100 au  $T_{\text{mid, 100 au}}$ , atmosphere gas temperature at radial distance 100 au  $T_{\text{atm, 100 au}}$ , temperature slope  $q$ , and gas molar mass  $\mu$ , in total 9 parameters. The ionization is calculated on top of the density distribution, using the corresponding parametrizations by Bruderer et al. (2009) for X-ray and Padovani et al. (2018) for CRP. The physical structure is then passed to the chemical abundance estimator described earlier in Chapter 4, generating a 2D chemical distribution in the disk. The resulting physical-chemical model is then transformed into RadMC3D format. The LTE line radiative transfer is run simultaneously for all the lines in a single run based on LAMDA line database (Schöier et al. 2005).

The disk forward models generated with DiskCheF were used by our group to submit successful NOEMA proposal (S21AT, PI: Francheschi). In addition to its own physical model, the produced software package is able to read ANDES models and visualize them using RadMC3D. This interface is used by the collaboration (Molyarova, Akimkin, Kóspál) to compare the thermo-chemical time-dependent models with the observations of variable accreting protostars. Another application was during the preparation of the observations series for the project “Catch me if you can: time-variable ionization of DQ Tau”, co-PI: van Terwisga, Smirnov-Pinchukov. The project has predicted that during the regular accretion event in a circumbinary disk DQ Tau, the  $\text{HCO}^+$  emission would vary by a factor of 10 or more on a timescale of days. The observations were scheduled for ALMA (2021.1.01414.S), IRAM 30m telescope (148-21), ground-based optical monitoring (ESO 2.2m/FEROS spectroscopy, Konkoly observatory, MASTER robotic telescope network), and the X-ray and UV observatory SWIFT. The preliminary X-ray analysis was published in Getman et al. (2022).

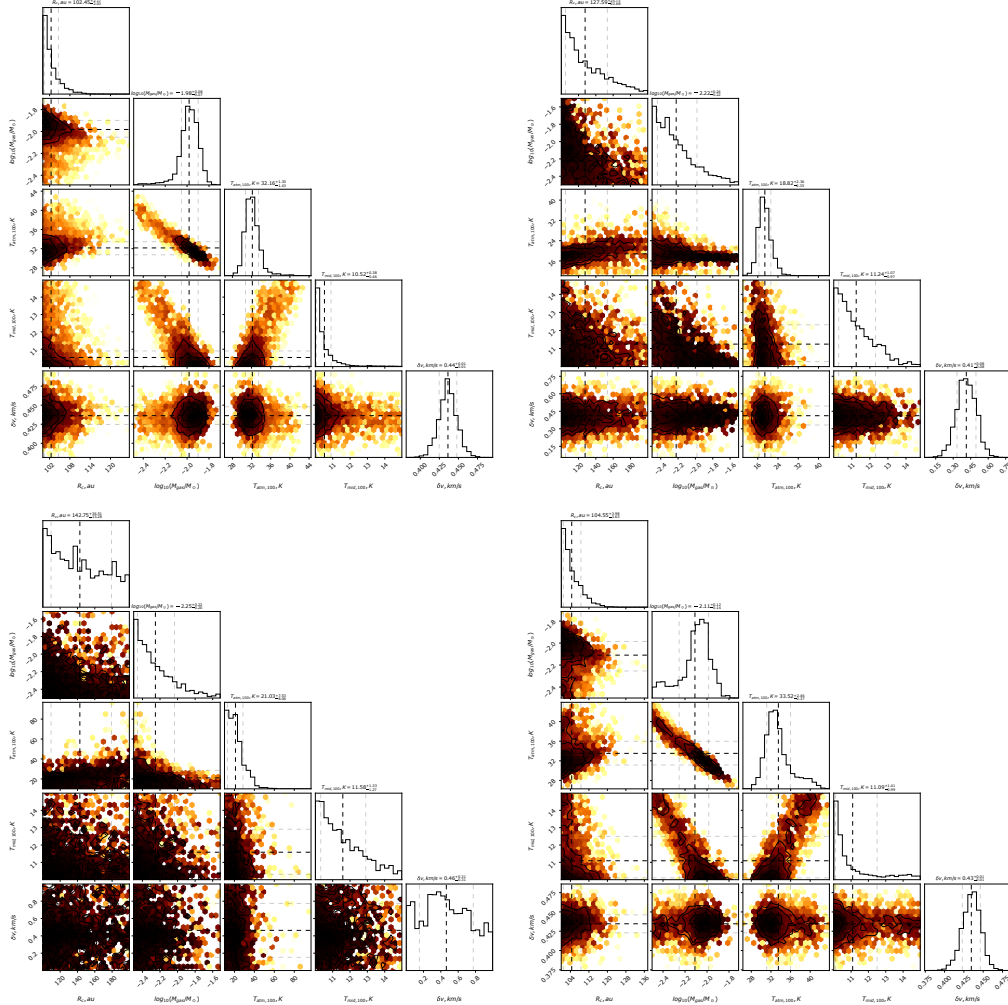


Figure 5.6: Corner plot miniatures of the posterior distribution of physical parameters derived by the DN Tau disk modeling compared with PRODIGE data. The full-sized figures are presented on pages 101-104. *Top-left*: CO J=2-1; *top-right*:  $^{13}\text{CO}$  J=2-1; *bottom-left*:  $\text{C}^{18}\text{O}$  J=2-1; *bottom-right*: combination of all three. From top to bottom and left to right of each panel: the outer radius, the total mass, the atmosphere temperature, the midplane temperature, the velocity offset.

## 5.4 Bayesian fitting

We derived posterior probability distributions with the nested sampling Monte Carlo algorithm MLFriends (Buchner 2019) using the UltraNest<sup>2</sup> package (Buchner 2021). This package provides a robust, efficient, MPI-cluster-ready way to fit and analyze posterior distributions of the model parameters. The model was built using the approach described in the previous section. The modeled line cubes were sampled in the  $u$ - $v$  space with the coverage taken from the data. We used `galario` package for the Fourier transfer of the cube (Tazzari et al. 2018) and for comparing different cubes visibilities, as image plane comparison suffers from the dirty beam deconvolution (clean) uncertainty. We have performed model-to-data fitting to the DN Tau data using single transitions of CO,  $^{13}\text{CO}$ , and  $\text{C}^{18}\text{O}$  J=2-1, and a combined fit adding the residual  $\chi^2$  of all three lines together. The fit did not include  $\text{HCO}^+$  isotopologs as we planned to constrain gas distribution using CO isotopologs first, and then derive the ionization parameters after fixing the structure

<sup>2</sup><https://johannesbuchner.github.io/UltraNest/>

parameters. The CI Tau was not chosen for this first application as the foreground cloud adds additional complexity to the fitting process. The pipeline was first tested on DM Tau data from *PRODIGE* sample where it converged well, but this data is work a progress of another colleague and it does not include the formylum isotopologs.

We demonstrate in the Fig. 5.6 the miniatures of the posterior distributions from the fit of DN Tau. These results are very preliminary and are proof of concept rather than the final fit of the data which will be performed by the group later. A few important effects were not yet taken into account. The fit does not reproduce the very inner disk as it is poorly sampled with the pixel grid, and the flux is not conserved. We are now experiment with sup-pixeling and finer grids. Also, the covariance matrix between the visibilities noise is not provided by the observatory, and the residuals could only be estimated based on diagonal of the covariance matrix, the individual visibility weights. The Bayesian methods like nested sampling or Monte Carlo Markov Chain (MCMC) are sensitive not only to the shape of  $\chi^2(p)$ , but also to the absolute values of the residual. The non-diagonal components of the covariance matrix related to the noise correlation are missing, which is efficiently increasing the residuals and improving the reported fit quality. To compensate for that, we divide the  $\chi^2$  by a factor of 100, which provides reasonable, but still preliminary error bars.

1. The fit derived solely from the optically-thick CO line is consistent with the fit derived from the combination of the lines. The ability of CO alone to predict the physical parameters comes from the fact that as the line is observed on the large number of individual velocity channels, the CO is probed at different depths at the line wings. Even though CO does not trace the midplane directly, it is shown that its total mass correlates with the disk mass better than mass of other species (Molyarova et al. 2017). Trapman et al. (2022) show that C<sup>18</sup>O in combination with N<sub>2</sub>H<sup>+</sup> is also a good proxy for the total gas mass, but both these molecules are significantly fainter.
2. Even in combination with isotopologs, CO is not good to derive the vertical temperature structure using this pipeline and data at this resolution. The one reason can be that the physical model of Williams & Best (2014) is not general enough to reproduce more complex disk structures. On the other hand, it was demonstrated that high-resolution CO isotopologs maps actually allow measuring of the vertical temperature structure (MAPS IV: Law et al. 2021). This disagreement is likely due to the limitations of the low spatial resolution available in our data.
3. C<sup>18</sup>O was not well detected in individual channel maps thus the fit only sets the upper limits on the temperature and mass, which is very predictable.
4. The fit did not converge to a good solution, even in the additional runs with broader parameter range. The reason can be a hidden but bright substructure is not directly resolved with our resolution. The ALMA study of the dust in this disk also could not explain the radial profile of the continuum emission using a simple dust distribution model (Long et al. 2019). More complex, not single-profile physical model can be used to explain this difference.

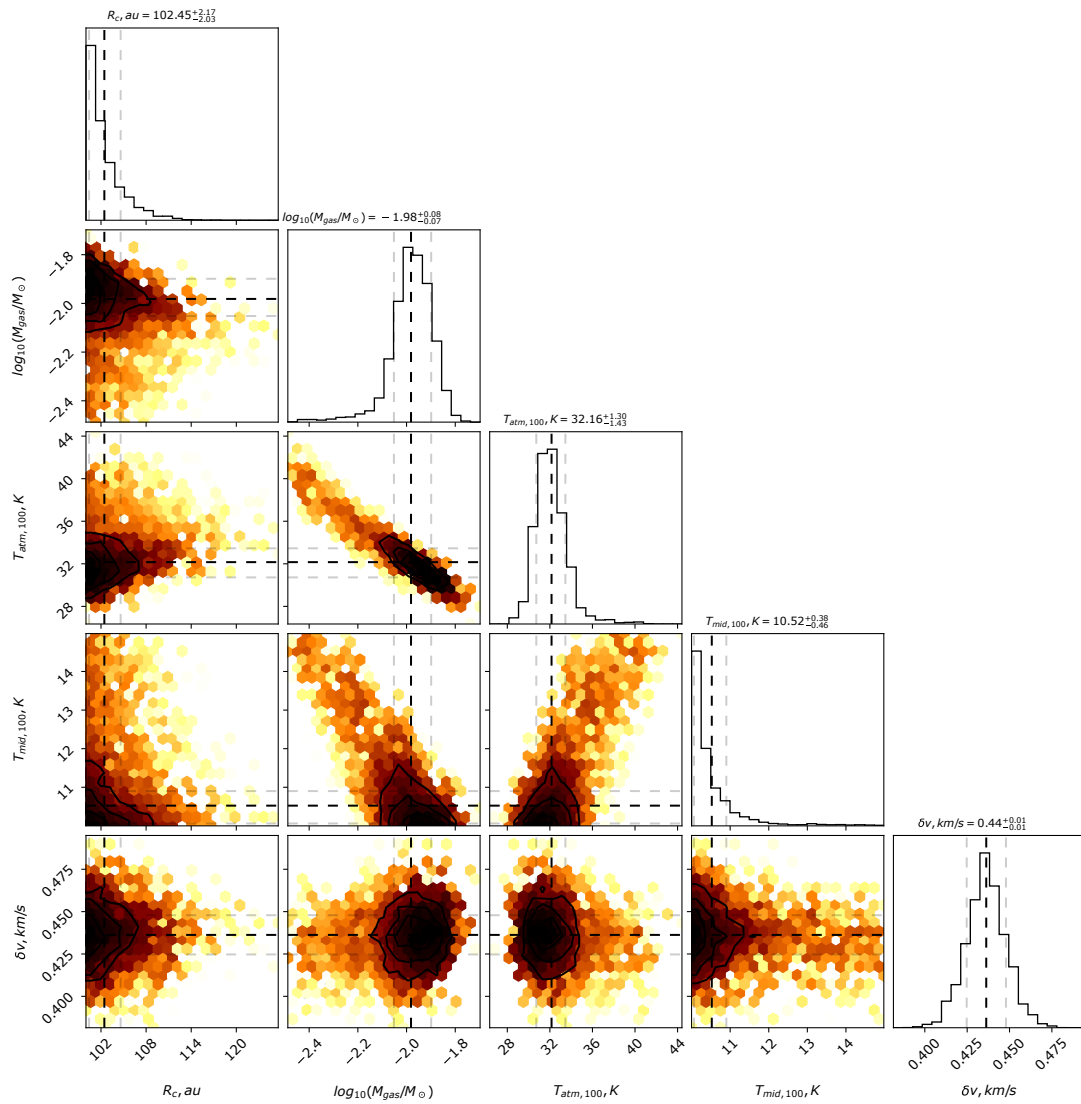
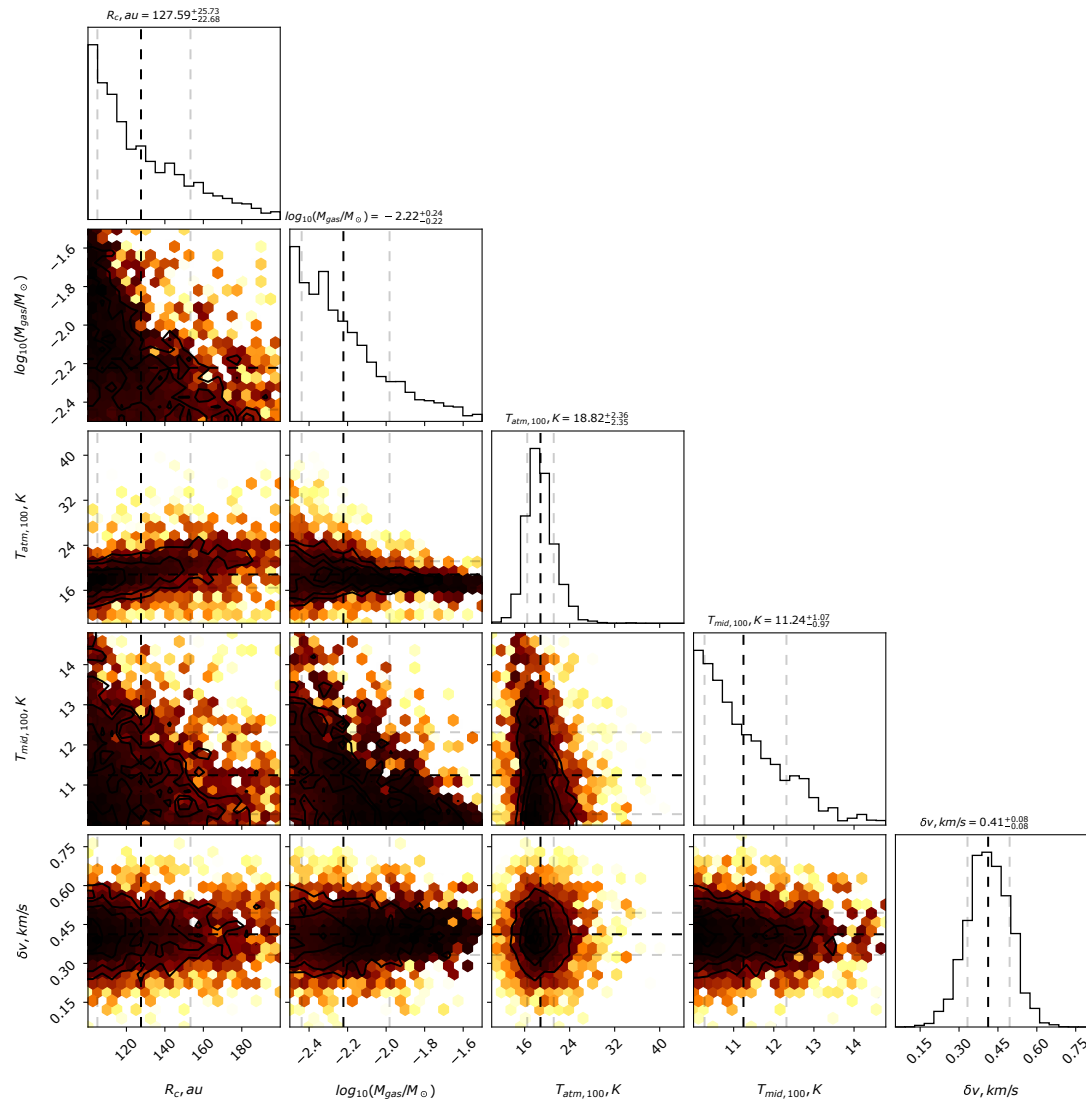
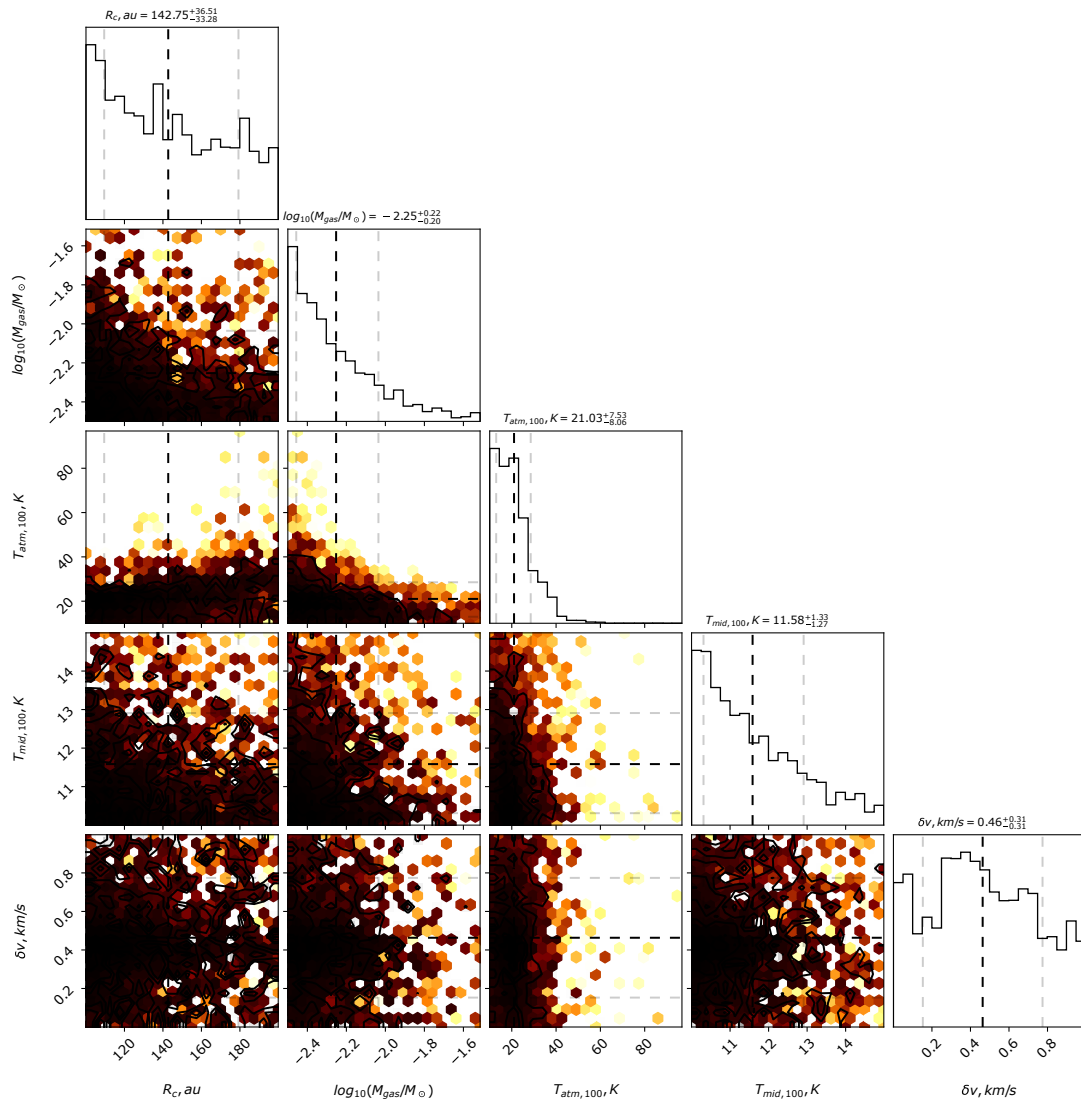


Figure 5.7: Corner plots of the posterior distribution of physical parameters derived by the DN Tau disk modeling compared with PRODIGE data, for CO J=2-1 line.

Figure 5.7: continued, for  $^{13}\text{CO}$  J=2-1.

Figure 5.7: continued, for C<sup>18</sup>O J=2-1.

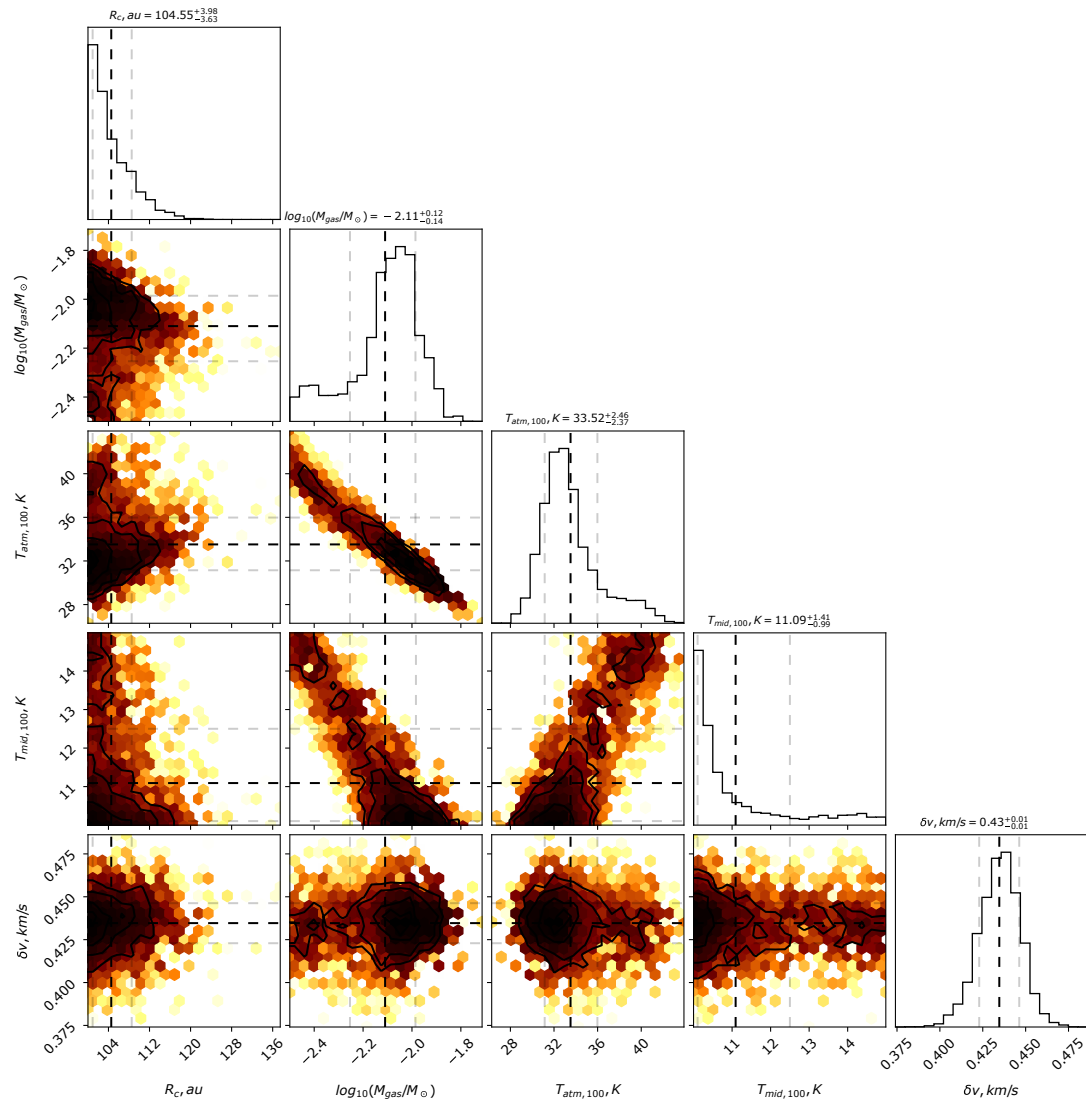


Figure 5.7: continued, for a combination of CO J=2-1,  $^{13}\text{CO}$  J=2-1, and  $\text{C}^{18}\text{O}$  J=2-1.

# Chapter 6

## Summary

The work performed for this thesis occupies a humble, but an important role in the field of protoplanetary disk chemistry. The broader community is usually thrilled by the large programs like DSHARP and MAPS (Andrews et al. 2018; Öberg et al. 2021), but this is only the tip of the iceberg. Most of the data taken by the telescopes and most of work hours spent do not operate with such fine and expensive data focusing on the most massive and bright disks, and rather focus on explaining less catchy, but more representative, low-resolution observation of disks representing most of the disk population.

In this thesis, I have discussed two applications of probing circumstellar disks with  $\text{HCO}^+$  isotopologs and the quick method of reproducing its abundances for Class II protoplanetary disks environments.

In Chapter 2, I modeled protoplanetary disks with and without gaps using thermochemical code ANDES, chemical kinetics code ALCHEMIC, and radiative transfer code LIME. The aim was to study how  $\text{C}^{18}\text{O}$ ,  $\text{HCO}^+$  and  $\text{DCO}^+$  react to various dust-to-gas ratios in the disk gap to answer the question of whether the gas is depleted in the gaps together with the dust. Comparison with observations from (Favre et al. 2019) has suggested that gas is also depleted which produces a counter-intuitive behavior of the  $\text{HCO}^+$  and  $\text{DCO}^+$  with optically-thick  $\text{HCO}^+$  tracing deeper colder regions and becoming fainter, but more of optically-thin  $\text{DCO}^+$  forming as ionization layer moves to a colder region, where deuterium fractionation plays a major role. This together leads to  $\text{DCO}^+/\text{HCO}^+$  ratio increase up to 0.1 - 1 compared to  $10^{-4}$  of the input D/H ratio. These results were published as Smirnov-Pinchukov et al. (2020).

In Chapter 3, I was performing the chemical (ALCHEMIC) and radiative transfer (RADEX) modeling of CO-rich debris disks for different elemental compositions to explain why other molecules (CN, HCN, CS,  $\text{HCO}^+$ ) were not detected. The observations sensitivity targeted the line-to-CO ratio of at least 0.1 compared to ratios observed for earlier evolutionary stage of Herbig Ae star. However, nothing was detected except for CO isotopologs. I have shown that for the small amount of small dust and thus optical depth of  $A_V \sim 1$ , observed for debris disks, UV radiation is too intense, and only mutually-shielded  $\text{H}_2$  and CO can remain. All other molecules forming or evaporating from ice grains would be photodissociated very quickly. Among other molecules,  $\text{HCO}^+$  was predicted to be less sensitive to photodissociation. As millimeter observations of molecules other than CO isotopologs are not expected within ALMA capabilities, I have suggested having a more detailed look at the vertical distribution of the gas in edge-on debris disks for a hint of gas chemical composition. It was already shown that the edge-on debris disk around 49 Ceti has 25% lower vertical scale height than expected, assuming  $\text{H}_2$  and He composition (Hughes et al. 2017). As the CO/H ratio grows from  $\sim 10^{-4}$  with secondary CO being evaporated from the ice grains and primordial hydrogen being removed from

the system, the gas mean molecular mass and thus the vertical scale height will change too. I associated the observed effect in 49 Cet with the CO/H ratio of about  $2 \times 10^{-2}$ . We have published these results as Smirnov-Pinchukov et al. (2022b).

In Chapter 4, I have addressed the issue of chemical simulations being too slow to be incorporated in the fitting of disk observations. Instead, I proposed a machine learning pipeline to incorporate grids of full disk chemical models generated with traditional codes (ANDES in this case) into a quick function to predict the chemistry of other disk models. We discuss its performance and the limitations of the approach. This work is accepted for publication in A&A and is now published as a preprint (Smirnov-Pinchukov et al. 2022a). This approach will be used in an upcoming series of papers to fit the molecular data obtained in the framework of the large observing program on NOEMA, PRODIGE/L19ME (PI: Th. Henning). We use this method to rapidly calculate chemical composition for the Bayesian retrieval of disk physical parameters using CO isotopologs (Francheschi et al., in prep.) and a combined fit of other molecules in the nearest future. The approach is discussed in the previously unpublished Chapter 5 with the outline for the future research.

In addition to the work described in this thesis, I participated in other projects, just briefly mentioned in the thesis. I worked on the data reduction and analysis pipeline for the NOEMA large program PRODIGE (L19ME). I was planning, coordinating, and executing the program with my colleague Sierk van Terwisga as a co-PI. In parallel, I have suggested a method for deriving the expansion velocities of spatially unresolved ionized gas bubbles around young star clusters (Smirnov-Pinchukov & Egorov 2021).

## Authored publications

1. Smirnov-Pinchukov, G. V., Semenov, D. A., Akimkin, V. V., and Henning, T., **Using HCO<sup>+</sup> isotopologues as tracers of gas depletion in protoplanetary disk gaps**, *Astronomy & Astrophysics*, vol. 644, 2020. doi:10.1051/0004-6361/202038572.
2. Smirnov-Pinchukov, G. V., Moór, A., Semenov, D. A., Ábrahám, P., Henning, T., Kóspál, Á., Hughes, A. M., di Folco, E., **Lack of other molecules in CO-rich debris discs: is it primordial or secondary gas?**, *Monthly Notices of the Royal Astronomical Society*, vol. 510, no. 1, pp. 1148-1162, 2022. doi:10.1093/mnras/stab3146.
3. Smirnov-Pinchukov, G. V., Molyarova, T., Semenov, D.A., Akimkin, V. V., van Terwisga, S., Francheschi, R., Henning, T., **Machine learning-accelerated chemistry modeling of protoplanetary disks**, *Astronomy & Astrophysics*, vol. 666, L8, 2022. doi:10.1051/0004-6361/202244691

---

4. Smirnov-Pinchukov, G. V. and Egorov, O. V., **Measurements of the Expansion Velocities of Ionized-Gas Superbubbles in Nearby Galaxies Based on Integral Field Spectroscopy Data**, *Astrophysical Bulletin*, vol. 76, no. 4, pp. 367-380, 2021. doi:10.1134/S1990341321040131.

---

5. Valdivia-Mena, M. T., Pineda, J. E., Segura-Cox, D. M., Caselli, P., Neri, R., López-Sepulcre, A., Cunningham, N., Bouscasse, L., Semenov, D., Henning, Th., Piétu, V., Chapillon, E., Dutrey, A., Fuente, A., Guilloteau, S., Hsieh, T. H., Jiménez-Serra, I., Marino, S., Maureira, M. J., Smirnov-Pinchukov, G. V., Tafalla, M., and Zhao, B., **PRODIGE – Envelope to disk with NOEMA I. A 3000 au streamer feeding a Class I protostar**, accepted for publication in *Astronomy & Astrophysics*, 2022.
6. Getman, K. V., Akimkin, V. V., Arulanantham, N., Kóspál, Á., Semenov, D. A., Smirnov-Pinchukov, G. V., and van Terwisga, S. E., **The Young Binary DQ Tau Produces Another X-Ray Flare Near Periastron**, *Research Notes of the American Astronomical Society*, vol. 6, no. 3, 2022. doi:10.3847/2515-5172/ac618a.
7. Topchieva, A., Akimkin, V., and Smirnov-Pinchukov, G., **Infrared photometric properties of inner and outer parts of HII regions**, *Research in Astronomy and Astrophysics*, vol. 19, no. 10, 2019. doi:10.1088/1674-4527/19/10/148.
8. Egorov, O. V., Lozinskaya, T. A., Moiseev, A. V., and Smirnov-Pinchukov, G. V., **Star formation complexes in the ‘galaxy-sized’ supergiant shell of the galaxy Holmberg I**, *Monthly Notices of the Royal Astronomical Society*, vol. 478, no. 3, pp. 3386-3409, 2018. doi:10.1093/mnras/sty1158.
9. Egorov, O. V., Lozinskaya, T. A., Moiseev, A. V., and Smirnov-Pinchukov, G. V., **The supergiant shell with triggered star formation in the dwarf irregular galaxy IC 2574: neutral and ionized gas kinematics**, *Monthly Notices of the Royal Astronomical Society*, vol. 444, no. 1, pp. 376-391, 2014. doi:10.1093/mnras/stu1369.



# Bibliography

- Aikawa, Y., Cataldi, G., Yamato, Y., et al. 2021, *ApJS*, 257, 13
- Aikawa, Y., van Zadelhoff, G. J., van Dishoeck, E. F., & Herbst, E. 2002, *A&A*, 386, 622
- Akimkin, V., Zhukovska, S., Wiebe, D., et al. 2013, *ApJ*, 766, 8
- Albertsson, T., Indriolo, N., Kreckel, H., et al. 2014a, *ApJ*, 787, 44
- Albertsson, T., Semenov, D., & Henning, T. 2014b, *ApJ*, 784, 39
- Albertsson, T., Semenov, D. A., Vasyunin, A. I., Henning, T., & Herbst, E. 2013, *ApJS*, 207, 27
- Andrews, S. M. 2020, *ARA&A*, 58, 483
- Andrews, S. M., Huang, J., Pérez, L. M., et al. 2018, *ApJ*, 869, L41
- Ansdeell, M., Gaidos, E., Hedges, C., et al. 2020, *MNRAS*, 492, 572
- Ansdeell, M., Williams, J. P., van der Marel, N., et al. 2016, *ApJ*, 828, 46
- Ardévol Martínez, F., Min, M., Kamp, I., & Palmer, P. I. 2022, *A&A*, 662, A108
- Avenhaus, H., Quanz, S. P., Garufi, A., et al. 2018, *ApJ*, 863, 44
- Bai, X.-N. & Goodman, J. 2009, *ApJ*, 701, 737
- Bailer-Jones, C. A. L., Rybizki, J., Foesneau, M., Demleitner, M., & Andrae, R. 2021, *AJ*, 161, 147
- Bell, C. P. M., Mamajek, E. E., & Naylor, T. 2015, *MNRAS*, 454, 593
- Bergin, E. A., Du, F., Cleeves, L. I., et al. 2016, *ApJ*, 831, 101
- Bergner, J. B., Öberg, K. I., Bergin, E. A., et al. 2019, *ApJ*, 876, 25
- Biham, O., Furman, I., Pirronello, V., & Vidali, G. 2001, *ApJ*, 553, 595
- Bockelée-Morvan, D. & Biver, N. 2017, *Philosophical Transactions of the Royal Society of London Series A*, 375, 20160252
- Bosman, A. D. 2018, PhD thesis, University of Leiden, Netherlands
- Bosman, A. D., Walsh, C., & van Dishoeck, E. F. 2018, *A&A*, 618, A182
- Brinch, C. & Hogerheijde, M. R. 2010, *A&A*, 523, A25
- Brown-Sevilla, S. B., Keppler, M., Barraza-Alfaro, M., et al. 2021, *A&A*, 654, A35
- Bruderer, S., Doty, S. D., & Benz, A. O. 2009, *ApJS*, 183, 179
- Bruderer, S., van der Marel, N., van Dishoeck, E. F., & van Kempen, T. A. 2014, *A&A*, 562, A26
- Buchner, J. 2019, *PASP*, 131, 108005
- Buchner, J. 2021, *The Journal of Open Source Software*, 6, 3001
- Carleo, G., Cirac, I., Cranmer, K., et al. 2019, *Reviews of Modern Physics*, 91, 045002
- Carney, M. T., Fedele, D., Hogerheijde, M. R., et al. 2018, *A&A*, 614, A106
- Cataldi, G., Brandeker, A., Wu, Y., et al. 2018, *ApJ*, 861, 72
- Cataldi, G., Wu, Y., Brandeker, A., et al. 2020, *ApJ*, 892, 99
- Cazzoletti, P., van Dishoeck, E. F., Visser, R., Facchini, S., & Bruderer, S. 2018, *A&A*, 609, A93
- Ceccarelli, C., Caselli, P., Bockelée-Morvan, D., et al. 2014, in *Protostars and Planets VI*, ed. H. Beuther, R. S. Klessen, C. P. Dullemond, & T. Henning, 859

- Cieza, L. A., Ruíz-Rodríguez, D., Hales, A., et al. 2019, *MNRAS*, 482, 698
- Cleeves, L. I., Adams, F. C., & Bergin, E. A. 2013, *ApJ*, 772, 5
- Cleeves, L. I., Bergin, E. A., & Adams, F. C. 2014, *ApJ*, 794, 123
- Cleeves, L. I., Bergin, E. A., & Harries, T. J. 2015a, *ApJ*, 807, 2
- Cleeves, L. I., Bergin, E. A., Öberg, K. I., et al. 2017, *ApJ*, 843, L3
- Cleeves, L. I., Bergin, E. A., Qi, C., Adams, F. C., & Öberg, K. I. 2015b, *ApJ*, 799, 204
- Cleeves, L. I., Öberg, K. I., Wilner, D. J., et al. 2016, *ApJ*, 832, 110
- de Zeeuw, P. T., Hoogerwerf, R., de Bruijne, J. H. J., Brown, A. G. A., & Blaauw, A. 1999, *AJ*, 117, 354
- Dent, W. R. F., Greaves, J. S., & Coulson, I. M. 2005, *MNRAS*, 359, 663
- Dent, W. R. F., Wyatt, M. C., Roberge, A., et al. 2014, *Science*, 343, 1490
- Di Folco, E., Péricaud, J., Dutrey, A., et al. 2020, *A&A*, 635, A94
- Dieleman, S., Willett, K. W., & Dambre, J. 2015, *MNRAS*, 450, 1441
- Dolginov, A. Z. & Stepinski, T. F. 1994, *ApJ*, 427, 377
- Draine, B. T. & Lee, H. M. 1984, *ApJ*, 285, 89
- Drozdovskaya, M. N., Walsh, C., van Dishoeck, E. F., et al. 2016, *MNRAS*, 462, 977
- Du, F. & Bergin, E. A. 2014, *ApJ*, 792, 2
- Dunjko, V. & Briegel, H. J. 2018, *Reports on Progress in Physics*, 81, 074001
- Dutrey, A., Guilloteau, S., Piétu, V., et al. 2017, *A&A*, 607, A130
- Dutrey, A., Semenov, D., Chapillon, E., et al. 2014a, in *Protostars and Planets VI*, ed. H. Beuther, R. S. Klessen, C. P. Dullemond, & T. Henning, 317
- Dutrey, A., Semenov, D., Chapillon, E., et al. 2014b, *Protostars and Planets VI*, 317
- Eistrup, C., Walsh, C., & van Dishoeck, E. F. 2016, *A&A*, 595, A83
- Evans, N., Calvet, N., Cieza, L., et al. 2009, *arXiv e-prints*, arXiv:0901.1691
- Favre, C., Bergin, E. A., Cleeves, L. I., et al. 2015, *ApJ*, 802, L23
- Favre, C., Fedele, D., Maud, L., et al. 2019, *ApJ*, 871, 107
- Fedele, D., Carney, M., Hogerheijde, M. R., et al. 2017, *A&A*, 600, A72
- Fedele, D. & Favre, C. 2020, *A&A*, 638, A110
- Fedele, D., Tazzari, M., Booth, R., et al. 2018, *A&A*, 610, A24
- Flower, D. R. & Lique, F. 2015, *MNRAS*, 446, 1750
- Flower, D. R., Pineau des Forêts, G., & Walmsley, C. M. 2004, *A&A*, 427, 887
- Flower, D. R., Pineau Des Forêts, G., & Walmsley, C. M. 2006, *A&A*, 449, 621
- Gammie, C. F. 1996, *ApJ*, 457, 355
- Garrod, R. T. 2013, *ApJ*, 765, 60
- Garrod, R. T. & Herbst, E. 2006, *A&A*, 457, 927
- Garrod, R. T., Wakelam, V., & Herbst, E. 2007, *A&A*, 467, 1103
- Garrod, R. T. & Widicus Weaver, S. L. 2013, *Chemical Reviews*, 113, 8939
- Garufi, A., Podio, L., Codella, C., et al. 2020, *A&A*, 636, A65
- Gerlich, D. 1990, *J. Chem. Phys.*, 92, 2377
- Gerlich, D., Herbst, E., & Roueff, E. 2002, *Planet. Space Sci.*, 50, 1275
- Getman, K. V., Akimkin, V. V., Arulanantham, N., et al. 2022, *Research Notes of the American Astronomical Society*, 6, 64

- Goldberger, J., Hinton, G. E., Roweis, S., & Salakhutdinov, R. R. 2005, in *Advances in Neural Information Processing Systems*, ed. L. Saul, Y. Weiss, & L. Bottou, Vol. 17 (MIT Press)
- Gorti, U. & Hollenbach, D. 2004, *ApJ*, 613, 424
- Grassi, T., Bovino, S., Schleicher, D. R. G., et al. 2014, *MNRAS*, 439, 2386
- Grassi, T., Nauman, F., Ramsey, J. P., et al. 2021, arXiv e-prints, arXiv:2104.09516
- Guilloteau, S., Di Folco, E., Dutrey, A., et al. 2013, *A&A*, 549, A92
- Guilloteau, S., Reboussin, L., Dutrey, A., et al. 2016, *A&A*, 592, A124
- Guzmán, V. V., Bergner, J. B., Law, C. J., et al. 2021, *ApJS*, 257, 6
- Guzmán, V. V., Huang, J., Andrews, S. M., et al. 2018, *ApJ*, 869, L48
- Harada, N., Herbst, E., & Wakelam, V. 2010, *Astrophys. J.*, 721, 1570
- Harada, N., Herbst, E., & Wakelam, V. 2012, *ApJ*, 756, 104
- Hasegawa, T. I., Herbst, E., & Leung, C. M. 1992, *ApJS*, 82, 167
- Heays, A. N., Bosman, A. D., & van Dishoeck, E. F. 2017, *A&A*, 602, A105
- Herbst, E. & Klemperer, W. 1973, *ApJ*, 185, 505
- Hobbs, L. M., Vidal-Madjar, A., Ferlet, R., Albert, C. E., & Gry, C. 1985, *ApJ*, 293, L29
- Holdship, J. & Viti, S. 2022, *A&A*, 658, A103
- Holdship, J., Viti, S., Haworth, T. J., & Ilee, J. D. 2021, *A&A*, 653, A76
- Holdship, J., Viti, S., Jiménez-Serra, I., Makrymallis, A., & Priestley, F. 2017, *AJ*, 154, 38
- Honvault, P., Jorfi, M., González-Lezana, T., Faure, A., & Pagani, L. 2011, *Physical Review Letters*, 107, 023201
- Hoogerwerf, R. 2000, *MNRAS*, 313, 43
- Huang, J., Andrews, S. M., Cleeves, L. I., et al. 2018a, *ApJ*, 852, 122
- Huang, J., Andrews, S. M., Dullemond, C. P., et al. 2018b, *ApJ*, 869, L42
- Huang, J., Andrews, S. M., Dullemond, C. P., et al. 2020, *ApJ*, 891, 48
- Huang, J. & Öberg, K. I. 2015, *ApJ*, 809, L26
- Huang, J., Öberg, K. I., Qi, C., et al. 2017, *AJ*, 835
- Hughes, A. M., Duchêne, G., & Matthews, B. C. 2018, *ARA&A*, 56, 541
- Hughes, A. M., Lieman-Sifry, J., Flaherty, K. M., et al. 2017, *ApJ*, 839, 86
- Hughes, A. M., Wilner, D. J., Kamp, I., & Hogerheijde, M. R. 2008, *ApJ*, 681, 626
- Hugo, E., Asvany, O., & Schlemmer, S. 2009, *J. Chem. Phys.*, 130, 164302
- Hunter, J. D. 2007, *Computing in Science & Engineering*, 9, 90
- Igea, J. & Glassgold, A. E. 1999, *ApJ*, 518, 848
- Ilee, J. D., Walsh, C., Booth, A. S., et al. 2021, *ApJS*, 257, 9
- Iqbal, W., Wakelam, V., & Gratier, P. 2018, *A&A*, 620, A109
- Isella, A., Guidi, G., Testi, L., et al. 2016, *Phys. Rev. Lett.*, 117, 251101
- Ivlev, A. V., Akimkin, V. V., & Caselli, P. 2016, *ApJ*, 833, 92
- Kama, M., Trapman, L., Fedele, D., et al. 2020, *A&A*, 634, A88
- Keil, M., Viti, S., & Holdship, J. 2022, *ApJ*, 927, 203
- Keppler, M., Teague, R., Bae, J., et al. 2019, *A&A*, 625, A118
- Klusmeyer, J., Hughes, A. M., Matra, L., et al. 2021, arXiv e-prints, arXiv:2107.07435
- Kóspál, Á., Moór, A., Juhász, A., et al. 2013, *ApJ*, 776, 77
- Kral, Q., Marino, S., Wyatt, M. C., Kama, M., & Matrà, L. 2019, *MNRAS*, 489, 3670

- Kral, Q., Matrà, L., Kennedy, G. M., Marino, S., & Wyatt, M. C. 2020, *MNRAS*, 497, 2811
- Kral, Q., Matrà, L., Wyatt, M. C., & Kennedy, G. M. 2017, *MNRAS*, 469, 521
- Law, C. J., Loomis, R. A., Teague, R., et al. 2021, *ApJS*, 257, 3
- Lee, H. H., Herbst, E., Pineau des Forets, G., Roueff, E., & Le Bourlot, J. 1996, *A&A*, 311, 690
- Lee, H.-H., Roueff, E., Pineau des Forets, G., et al. 1998, *A&A*, 334, 1047
- Lee, J.-E., Lee, S., Baek, G., et al. 2019, *Nature Astronomy*, 3, 314
- Lee, K. L. K., Patterson, J., Burkhardt, A. M., et al. 2021, *ApJ*, 917, L6
- Lieman-Sifry, J., Hughes, A. M., Carpenter, J. M., et al. 2016, *ApJ*, 828, 25
- Lin, D. N. C. & Papaloizou, J. C. B. 1993, in *Protostars and Planets III*, ed. E. H. Levy & J. I. Lunine, 749
- Long, F., Herczeg, G. J., Harsono, D., et al. 2019, *ApJ*, 882, 49
- Long, F., Pinilla, P., Herczeg, G. J., et al. 2018, *ApJ*, 869, 17
- Lovell, A. J., Schloerb, F. P., Bergin, E. A., et al. 1997, *Earth Moon and Planets*, 77, 253
- Marino, S., Flock, M., Henning, T., et al. 2020, *MNRAS*, 492, 4409
- Marino, S., Matrà, L., Stark, C., et al. 2016, *MNRAS*, 460, 2933
- Marino, S., Wyatt, M. C., Panić, O., et al. 2017, *MNRAS*, 465, 2595
- Martí-Vidal, I., Vlemmings, W. H. T., Muller, S., & Casey, S. 2014, *A&A*, 563, A136
- Matrà, L., MacGregor, M. A., Kalas, P., et al. 2017, *ApJ*, 842, 9
- Matrà, L., Öberg, K. I., Wilner, D. J., Olofsson, J., & Bayo, A. 2019, *AJ*, 157, 117
- Matrà, L., Wilner, D. J., Öberg, K. I., et al. 2018, *ApJ*, 853, 147
- McMullin, J. P., Waters, B., Schiebel, D., Young, W., & Golap, K. 2007, in *Astronomical Society of the Pacific Conference Series*, Vol. 376, *Astronomical Data Analysis Software and Systems XVI*, ed. R. A. Shaw, F. Hill, & D. J. Bell, 127
- Meeus, G., Montesinos, B., Mendigutía, I., et al. 2012, *A&A*, 544, A78
- Milam, S. N., Savage, C., Ziurys, L. M., & Wyckoff, S. 2004, *ApJ*, 615, 1054
- Miley, J. M., Panić, O., Wyatt, M., & Kennedy, G. M. 2018, *A&A*, 615, L10
- Millar, T. J., Walsh, C., Cordiner, M. A., Ní Chuimín, R., & Herbst, E. 2007, *ApJ*, 662, L87
- Miotello, A., Bruderer, S., & van Dishoeck, E. F. 2014, *A&A*, 572, A96
- Miotello, A., Facchini, S., van Dishoeck, E. F., & Bruderer, S. 2018, *A&A*, 619, A113
- Miotello, A., Facchini, S., van Dishoeck, E. F., et al. 2019, *A&A*, 631, A69
- Molyarova, T., Akimkin, V., Semenov, D., et al. 2018, *ApJ*, 866, 46
- Molyarova, T., Akimkin, V., Semenov, D., et al. 2017, *ApJ*, 849, 130
- Moór, A., Curé, M., Kóspál, Á., et al. 2017, *ApJ*, 849, 123
- Moór, A., Juhász, A., Kóspál, Á., et al. 2013, *ApJ*, 777, L25
- Moór, A., Kral, Q., Ábrahám, P., et al. 2019, *ApJ*, 884, 108
- Mumma, M. J. & Charnley, S. B. 2011, *ARA&A*, 49, 471
- Muro-Arena, G. A., Benisty, M., Ginski, C., et al. 2020, *A&A*, 635, A121
- Murphy, S. J., Joyce, M., Bedding, T. R., White, T. R., & Kama, M. 2021, *MNRAS*, 502, 1633
- Nakatani, R., Kobayashi, H., Kuiper, R., Nomura, H., & Aikawa, Y. 2021, *ApJ*, 915, 90
- Öberg, K. I. & Bergin, E. A. 2021, *Phys. Rep.*, 893, 1

- Öberg, K. I., Boogert, A. C. A., Pontoppidan, K. M., et al. 2011, *ApJ*, 740, 109
- Öberg, K. I., Guzmán, V. V., Walsh, C., et al. 2021, *ApJS*, 257, 1
- Öberg, K. I., Qi, C., Fogel, J. K. J., et al. 2010, *ApJ*, 720, 480
- Oberg, K. I., Qi, C., Wilner, D. J., & Andrews, S. M. 2011, *The Astrophysical Journal*, 743, 152
- O'Dell, C. R. & Wen, Z. 1994, *ApJ*, 436, 194
- Padovani, M., Ivlev, A. V., Galli, D., & Caselli, P. 2018, *A&A*, 614, A111
- Pagani, L., Vastel, C., Hugo, E., et al. 2009, *A&A*, 494, 623
- Parfenov, S. Y., Semenov, D. A., Sobolev, A. M., & Gray, M. D. 2016, *MNRAS*, 460, 2648
- Pavlyuchenkov, Y., Semenov, D., Henning, T., et al. 2007, *ApJ*, 669, 1262
- Pecaut, M. J. & Mamajek, E. E. 2016, *MNRAS*, 461, 794
- Pedregosa, F., Varoquaux, G., Gramfort, A., et al. 2011, *Journal of Machine Learning Research*, 12, 2825
- Pegues, J., Öberg, K. I., Bergner, J. B., et al. 2021, *ApJ*, 911, 150
- Pegues, J., Öberg, K. I., Bergner, J. B., et al. 2020, *ApJ*, 890, 142
- Péicaud, J., Di Folco, E., Dutrey, A., Guiloteau, S., & Piétu, V. 2017, *A&A*, 600, A62
- Qi, C., Öberg, K. I., & Wilner, D. J. 2013, *ApJ*, 765, 34
- Rab, C., Güdel, M., Padovani, M., et al. 2017, *A&A*, 603, 96
- Rab, C., Güdel, M., Woitke, P., et al. 2018, *A&A*, 609, A91
- Reback, J., McKinney, W., jbrockmendel, et al. 2021, *pandas-dev/pandas: Pandas 1.2.4*
- Ribas, Á., Espaillat, C. C., Macías, E., & Sarro, L. M. 2020, *A&A*, 642, A171
- Roberge, A., Feldman, P. D., Lagrange, A. M., et al. 2000, *ApJ*, 538, 904
- Roberge, A., Feldman, P. D., Weinberger, A. J., Deleuil, M., & Bouret, J.-C. 2006, *Nature*, 441, 724
- Roberge, A., Welsh, B. Y., Kamp, I., Weinberger, A. J., & Grady, C. A. 2014, *ApJ*, 796, L11
- Roberts, H., Herbst, E., & Millar, T. J. 2004, *A&A*, 424, 905
- Roberts, H. & Millar, T. J. 2000, *A&A*, 361, 388
- Röllig, M., Abel, N. P., Bell, T., et al. 2007, *A&A*, 467, 187
- Rollins, R. P. & Rawlings, J. M. C. 2012, *MNRAS*, 427, 2328
- Roueff, E., Lis, D. C., van der Tak, F. F. S., Gerin, M., & Goldsmith, P. F. 2005, *A&A*, 438, 585
- Ruaud, M., Wakelam, V., & Hersant, F. 2016, *MNRAS*, 459, 3756
- Salinas, V. N., Hogerheijde, M. R., Murillo, N. M., et al. 2018, *A&A*, 616, A45
- Schöier, F. L., van der Tak, F. F. S., van Dishoeck, E. F., & Black, J. H. 2005, *A&A*, 432, 369
- Semenov, D., Hersant, F., Wakelam, V., et al. 2010, *A&A*, 522, A42
- Semenov, D. & Wiebe, D. 2011, *ApJ*, 196, 25
- Semenov, D., Wiebe, D., & Henning, T. 2004, *A&A*, 417, 93
- Sipilä, O., Caselli, P., & Harju, J. 2013, *A&A*, 554, A92
- Smirnov-Pinchukov, G. V. & Egorov, O. V. 2021, *Astrophysical Bulletin*, 76, 367
- Smirnov-Pinchukov, G. V., Molyarova, T., Semenov, D. A., et al. 2022a, 666, L8
- Smirnov-Pinchukov, G. V., Moór, A., Semenov, D. A., et al. 2022b, *MNRAS*, 510, 1148

- Smirnov-Pinchukov, G. V., Semenov, D. A., Akimkin, V. V., & Henning, T. 2020, *A&A*, 644, A4
- Smith, I. W. M. 2011, *ARA&A*, 49, 29
- Strom, K. M., Strom, S. E., Edwards, S., Cabrit, S., & Skrutskie, M. F. 1989, *AJ*, 97, 1451
- Tazzari, M., Beaujean, F., & Testi, L. 2018, *MNRAS*, 476, 4527
- Teague, R., Bae, J., Aikawa, Y., et al. 2021, *ApJS*, 257, 18
- Teague, R., Bae, J., Birnstiel, T., & Bergin, E. A. 2018, *ApJ*, 868, 113
- Teague, R. & Loomis, R. 2020, arXiv e-prints, arXiv:2007.11906
- Teague, R., Semenov, D., Gorti, U., et al. 2017, *ApJ*, 835, 228
- Teague, R., Semenov, D., Guilloteau, S., et al. 2015, *A&A*, 574, A137
- Trapman, L., Miotello, A., Kama, M., van Dishoeck, E. F., & Bruderer, S. 2017, *A&A*, 605, A69
- Trapman, L., Zhang, K., van't Hoff, M. L. R., Hogerheijde, M. R., & Bergin, E. A. 2022, *ApJ*, 926, L2
- van Boekel, R., Henning, T., Menu, J., et al. 2017, *ApJ*, 837, 132
- van der Plas, G., Ménard, F., Gonzalez, J. F., et al. 2019, *A&A*, 624, A33
- van der Tak, F. F. S., Black, J. H., Schöier, F. L., Jansen, D. J., & van Dishoeck, E. F. 2010, *Radex: Fast Non-LTE Analysis of Interstellar Line Spectra*
- van Terwisga, S. E., van Dishoeck, E. F., Cazotte, P., et al. 2019, *A&A*, 623, A150
- Vasyunin, A. I. & Herbst, E. 2013, *ApJ*, 769, 34
- Vasyunin, A. I., Semenov, D., Henning, T., et al. 2008, *ApJ*, 672, 629
- Vasyunin, A. I., Semenov, D. A., Wiebe, D. S., & Henning, T. 2009, *ApJ*, 691, 1459
- Veal, J. M., Snyder, L. E., Wright, M. C. H., et al. 1997, *IAU Circ.*, 6575, 1
- Vidal-Madjar, A., Lagrange-Henri, A. M., Feldman, P. D., et al. 1994, *A&A*, 290, 245
- Villadsen, T., Ligterink, N. F. W., & Andersen, M. 2022, arXiv e-prints, arXiv:2207.03906
- Visser, R., van Dishoeck, E. F., & Black, J. H. 2009, *Astron. Astrophys.*, 503, 323
- Wakelam, V., Herbst, E., Loison, J.-C., et al. 2012, *Astrophys. J., Suppl. Ser.*, 199, 21
- Wakelam, V., Loison, J. C., Herbst, E., et al. 2015, *ApJS*, 217, 20
- Walmsley, C. M., Flower, D. R., & Pineau des Forêts, G. 2004, *A&A*, 418, 1035
- Walsh, C., Nomura, H., & van Dishoeck, E. 2015, *A&A*, 582, A88
- Weintraub, D. A., Sandell, G., & Duncan, W. D. 1989, *ApJ*, 340, L69
- White, J. A. & Boley, A. C. 2018, *ApJ*, 859, 103
- Wichittanakom, C., Oudmaijer, R. D., Fairlamb, J. R., et al. 2020, *MNRAS*, 493, 234
- Wiebe, D., Semenov, D., & Henning, T. 2003, *A&A*, 399, 197
- Willacy, K., Klahr, H. H., Millar, T. J., & Henning, T. 1998, *A&A*, 338, 995
- Williams, J. P. & Best, W. M. J. 2014, *ApJ*, 788, 59
- Wilson, T. L. & Rood, R. 1994, *ARA&A*, 32, 191
- Woitke, P., Kamp, I., & Thi, W. F. 2009, *A&A*, 501, 383
- Wyatt, M. C. 2008, *ARA&A*, 46, 339
- Yorke, H. W. & Bodenheimer, P. 2008, in *Astronomical Society of the Pacific Conference Series, Vol. 387, Massive Star Formation: Observations Confront Theory*, ed. H. Beuther, H. Linz, & T. Henning, 189
- Yu, M., Willacy, K., Dodson-Robinson, S. E., Turner, N. J., & Evans, Neal J., I. 2016, *ApJ*, 822, 53
- Zuckerman, B. & Song, I. 2012, *ApJ*, 758, 77

# Acknowledgements

My PhD project happened in the harsh time. With the very bright first 1.5 years, after making many friends and scientific connections, the pandemic has locked us behind the closed doors and face masks. Even now, 2.5 years since restrictions were first introduced, the wound in our community did not fully heal. One trouble follows another, and in 2022 my home country is torn apart into madness and hate. The last preparations for this thesis were made in an atmosphere of approaching global war, in which my people are on the wrong side. The tides within and between the families broke, and infinite reports about the destruction and death have replaced the COVID charts. I am happy that I could help the people of Ukraine, who found their shelter in Heidelberg: Anastasiia Martemianova with her son Tim, Olga Zakhzhay with her daughter Sonia, Nadiia Pulatova with her daughter Mila, and Andrey Zigloh, and many other new friends who share time at our place. Peace to you, your beloved, and your country, and to the whole planet.

I want to thank my friends who stayed in contact during the hardest times. Iliia Kuksenok, Vasili Golubtsov, Sergey Sapozhnikov, Dmitri Olach, thank you, *pocony*, for our almost-nightly chats, discussions and activities. Alexandra Grudskaya, Alexey Nikonov, Oleg Egorov and Evgeniya Egorova, many others. Thank you all for being yourself.

I thank my advisors: Thomas Henning for the opportunities, Dima Semenov for the communications, and Kees Dullemond for the advises in the right times. Great thanks to my collaborators, who were always respectful, enthusiastic, and very helpful, especially Attila Moór, Vitaly Akimkin, Tamara Molyarova, Peter Ábrahám, and Agnes Kóspál. To our latest mini-group: to Riccardo Francheschi for being honest, to Sierk van Terwisga for being optimistic, to Kamber Schwarz for being supportive. To the colleagues attending the PPDTea before the pandemic, especially Christian Lenz, Camille Bergez-Casalou, Lucia Klarmann, Vincent Carpenter, Gideon Yoffe, thank you for believing in me. To Matthias Samland for organizing MeetPy and to Felix Bosco and Eduard Bopp for giving interesting talks there. To all my office mates over these years, and to those coming to the student coffee. To Aida Ahmadi and Asmita Bhandare, THE student representatives. I want to additionally thank MPIA ombudspersons Coryn Bayler-Jones and Christian Fendt as well as PAC members Tom Herbst and Fabian Walter to helping in the darkest moments.

To all other people of MPIA, with whom we chatted over the coffee or lunch, for always being intelligent and inspiring.

To the organizers of the best summer school ever – Torun summer school on astrophysics, spectroscopy and quantum chemistry – especially Agata Karska and Justyna Cembrzyńska, these were wonderful two weeks.

To my Master's advisor Tatiana Alexandrovna Lozinskaya, and to our SAI student group coordinator, Konstantin Alexandrovich Postnov. Thank you for your guidance in my early stages, and for helping me to become a person I have become.

To my wife Irina, for being the best. To my daughter Marina, for being the strongest and the smartest. To Tonya. Thank you for making my life brighter.



# **Declaration of Originality**

## **Declaration of Originality**

I hereby declare that this thesis is my own work and that I have used no other than the stated sources and aids.

## **Originalitätserklärung**

Ich versichere, dass ich diese Arbeit selbstständig verfasst habe und keine anderen als die angegebenen Quellen und Hilfsmittel benutzt habe.

Heidelberg, October 30, 2022

(Grigorii V. Smirnov-Pinchukov)

